Karlsruher Institut für Technologie

Schriftenreihe
Kontinuumsmechanik im Maschinenbau

27

Patrick Arthur Hessman

On multi-scale modeling of fatigue in short glass fiber reinforced thermoplastics

KIT Scientific Publishing

Patrick Arthur Hessman

On multi-scale modeling of fatigue in short glass fiber reinforced thermoplastics

Schriftenreihe
Kontinuumsmechanik im Maschinenbau
Band 27

Karlsruher Institut für Technologie (KIT)
Institut für Technische Mechanik
Bereich Kontinuumsmechanik

Hrsg. Prof. Dr.-Ing. habil. Thomas Böhlke

Eine Übersicht aller bisher in dieser Schriftenreihe erschienenen Bände finden Sie am Ende des Buchs.

On multi-scale modeling of fatigue in short glass fiber reinforced thermoplastics

by
Patrick Arthur Hessman

KIT Scientific Publishing

Karlsruher Institut für Technologie
Institut für Technische Mechanik
Bereich Kontinuumsmechanik

On multi-scale modeling of fatigue in short glass fiber reinforced thermoplastics

Zur Erlangung des akademischen Grades eines Doktors der Ingenieurwissenschaften von der KIT-Fakultät für Maschinenbau des Karlsruher Instituts für Technologie (KIT) genehmigte Dissertation

von Patrick Arthur Hessman, M.Sc.

Tag der mündlichen Prüfung: 15. Mai 2024
Hauptreferent: Prof. Dr.-Ing. Thomas Böhlke
Korreferent: Prof. Dr.-Ing. Ralf Müller

Impressum

Scientific Publishing

Karlsruher Institut für Technologie (KIT)
KIT Scientific Publishing
Straße am Forum 2
D-76131 Karlsruhe

KIT Scientific Publishing is a registered trademark of Karlsruhe Institute of Technology.
Reprint using the book cover is not allowed.

www.ksp.kit.edu

Print on Demand 2025 – Gedruckt auf FSC-zertifiziertem Papier

ISSN 2192-693X
ISBN 978-3-7315-1398-8
DOI 10.5445/KSP/1000176738

Zusammenfassung

Kurzglasfaserverstärkte Thermoplaste sind eine wichtige Materialklasse für eine Reihe industrieller Anwendungen. Sie vereinen attraktive mechanische Eigenschaften, wie eine hohe spezifische Steifigkeit, eine hohe spezifische Festigkeit, Korrosionsbeständigkeit und kosteneffizienten Fertigungsmethoden wie dem Spritzguss. Während des Fertigungsprozesses stellt sich aufgrund der Strömungsverhältnisse in der Kavität des Werkzeuges eine komplexe Mikrostruktur der verstärkenden Fasern in der Matrix mit verschiedenen Orientierungszuständen und Faserlängen ein.

Aufgrund dieser komplexen Mikrostruktur müssen Simulationsmodelle für kurzglasfaserverstärkte Thermoplaste auf Mehrskalenmethoden zurückgreifen, welche den Einfluss der Mikrostruktur auf das makroskopische Verhalten des Bauteils und umgekehrt abbilden. Innerhalb dieses Kontextes beschäftigt sich die vorliegende Arbeit mit der mikromechanischen Modellierung von kurzglasfaserverstärkten Thermoplasten mit dem Ziel sowohl das elastische Verhalten des Komposits als auch das Schädigungsverhalten und die Festigkeit unter Ermüdungslast zu beschreiben. Dabei steht ein kommerziell verfügbares kurzglasfaserverstärktes Polyamid 6.6 mit Fasermassenanteilen zwischen $15\,\%$ and $50\,\%$ im Fokus.

Um sowohl genaue als auch zuverlässige Mikrostrukturdaten zu bekommen wird zunächst ein neuartiger Segmentierungsalgorithmus für Einzelfasern vorgestellt, welcher in der Lage ist die Faserorientierungs- und Faserlängenverteilungen anhand hochauflösender Mikro-Computertomographie Aufnahmen von Komposit-Prüfkörpern zu ermitteln. Im

Anschluss werden drei solche Aufnahmen verwendet, um relevante statistische Metriken der Mikrostruktur abzuleiten und zu diskutieren. Eine Besonderheit des Vorgehens ist es, dass aufgrund der Einzelfaser-Segmentierung auch Korrelationen zwischen der Längen- und Orientierungsverteilung untersucht werden können.

Im zweiten Schritt werden ein Satz häufig angewendeter analytischer Mean-Field Homogenisierungsansätze eingeführt und untersucht, welche in der Lage sind Mikrostrukturinformationen für die Modellierung auf Bauteilebene zu nutzen. Dies sind die Selbstkonsistenzmethode, der Mori-Tanaka Ansatz, das Modell von Ponte Castañeda-Willis, das Interaction Direct Derivative Modell sowie das Two-Step Modell. Die Modelle werden in einer einheitlichen Struktur präsentiert, welche einen detaillierten Vergleich und eine tiefgreifende Diskussion ermöglicht; unter anderem Untersuchungen zur Wahrung der diagonalen Symmetrie des Steifigkeitstensors, welche für manche Modelle und Mikrostrukturzustände nicht garantiert werden kann. Im Anschluss werden verschiedene Methoden zur Berücksichtigung der Mikrostruktur diskutiert, einschließlich einer kürzlich vorgestellten Vorgehensweise zur effizienteren Integration der Orientierungsverteilung. Die Modelle werden auch in Bezug auf die berechneten effektiven elastischen Eigenschaften der Komposite und die berechneten Spannungen und Dehnungen in den Fasern verglichen. Dabei werden auch Vollfeld-Ergebnisse aus numerischen Homogenisierungen mittels Fast Fourier Transformation (FFT) und experimentell bestimmte Komposit-Steifigkeitswerte aus Zugversuchen hinzugezogen.

In Bezug auf die Modellierung des Ermüdungsverhaltes wird ein mikromechanisches Hochzyklen-Ermüdungsmodell entwickelt. Es basiert auf dem Two-Step Homogenisierungsschema und führt Schädigungsvariablen für die Faser- und Matrix-Phase ein. Während die Faserschädigung mittels einer modifizierten Tsai-Wu Belastungsfunktion in Kombination mit einer Weibull-Verteilung beschrieben wird, wird für die Matrix-

schädigung ein modifiziertes zyklenbasiertes Schädigungsmodells nach Peerlings et al. (2000) verwendet. Diese material-spezifische Modifikation bezieht sich auf einen neuen Interaktionsterm in der Schädigungsfunktion, welcher die Rate der Matrixschädigung in Abhängigkeit von der mittleren Faserschädigung im Komposit modelliert. Im Anschluss wird die Vorhersagegüte in Bezug auf die Ermüdungsgrenze der verschiedenen kurzglasfaserverstärkten Polyamid 6.6 Komposite und für verschiedene Lastrichtungen untersucht.

Summary

Short glass fiber reinforced thermoplastic composites (SFRTs) are a vital class of materials for many industrial applications. They combine attractive mechanical properties such as high specific stiffness and high specific strength with corrosion resistance and low-cost mass-production by injection molding. During this production process the flow within the cavity leads to a final part with a complex microstructure of the reinforcing fibers in the matrix with varying orientation states and fiber lengths.

It is due to this complex microstructure that simulation models for assessing parts made from SFRTs need multi-scale techniques to model the influence of the microstructure on the macroscopic behavior and vice-versa. Within this context the present thesis covers the micromechanical modeling of SFRTs with the goal of describing both the elastic behavior of the composite material and the progressive damage behavior of the material during fatigue loading. Within this thesis a commonly applied commercial class of short glass fiber reinforced polyamide 6.6 (PA66-GF) composites is considered which are available with different fiber mass fractions between $15\,\%$ and $50\,\%$.

To obtain accurate and reliable microstructural data, a novel single fiber segmentation algorithm is introduced which allows the fiber orientation and length distributions to be obtained from high-resolution x-ray micro-computed tomography scans of SFRT composite specimens. The algorithm is discussed and relevant microstructural statistics are derived and discussed based on three scans. Due to the nature of the developed

algorithm, the correlation between fiber length and orientation can also be highlighted.

Secondly, a set of common analytical mean-field homogenization schemes are introduced and studied, which allow the microstructural data to be employed in models on the scale of real parts: the Self-Consistent, Mori-Tanaka, Ponte Castañeda-Willis, Interaction Direct Derivative and Two-Step models. They are presented in a unified structure to allow a thorough comparison and a meaningful discussion, including limitations such as the loss of major symmetry for some models and in some microstructural cases. Different methods of resolving the SFRT microstructure are discussed, including an efficient adaptive integration scheme for the orientation distribution. The different models are then compared with respect to the predicted effective elastic properties of the composite and the predicted stresses and strains within the fibers and the matrix material, including comparisons to full-field numerical homogenization results using Fast Fourier Transformation (FFT) methods and experimental stiffness values from tensile tests.

With respect to fatigue modeling a micromechanical high cycle fatigue model is proposed. It uses the Two-Step homogenization scheme and introduces damage variables for fibers and the matrix material. While the damage of the fiber phase is modeled using a modified Tsai-Wu loading function in conjunction with a Weibull-type probabilistic failure function, the fatigue damage in the matrix phase is modeled using a modification of the cycle-based model proposed by Peerlings et al. (2000). The modification introduces an interaction term coupling the level of fiber damage and the damage rate of the matrix material, which is motivated by the material-specific damage processes at the micro scale. The models ability to predict the fatigue limit of SFRTs is studied using S-N curves for different fiber orientations and fiber mass fractions.

Acknowledgments

My greatest thanks go to my supervisor, Thomas Böhlke, for supporting my doctoral research and giving me the opportunity to work and learn at the institute. His deep knowledge, our fruitful discussions and his continuous support have helped me navigate through my doctoral years and contributed immensely to ensuring I am where I am now.

I wish to thank Ralf Müller for co-supervising my dissertation and his support.

Thanks also go to Kurt Hornberger and Fabian Welschinger for supervising my research at the Corporate Sector Research and Advance Engineering of Robert Bosch GmbH. Their unconditional support, willingness to engage in extensive discussions, and their technical expertise have been indispensable for the success of my work. I wish to also thank Martin Giersbeck and Jan-Martin Kaiser for giving me the opportunity to perform my research in their department and work-group and providing the technical and financial means for my research.

The last years wouldn't have been the same without my fellow colleagues and PhD students, both at the Institute of Engineering Mechanics and at Bosch. Their support and friendship has been invaluable and the shared experiences will always be treasured. I wish to especially thank Philipp Weißgraeber for the willingness to share his experience and to be there when encouragement was needed the most.

Finally, I owe my deepest thanks to my family: My parents Karin and Frederic for giving me the foundation onto which I was able to build and the support to freely find my own path, my brother Christopher

for his compassion and love, and my sons Finn and Enno for their understanding and patience.

Above all, I am deeply indebted to my wife Sarah: for her unconditional love and support, for providing me with the freedom and time to pursue my research and thesis, and her understanding and patience, without which none of this would have been possible.

Karlsruhe, May 2024 Patrick Arthur Hessman

Contents

Chapter 1

Introduction

1.1 Motivation

Short glass fiber thermoplastics (SFRTs) are a material class of great industrial importance and academic interest. They are used in the design and production of various products, including housings, electrical components, connectors and sensors. Large-scale and cost-optimal applications are facilitated by injection molding, which also allows for the integration of other functional parts, such as the over-molding of electrical connections or bushings. These properties, combined with the material classes high specific stiffness and strength, have made SFRTs an attractive substitute for most costly materials and processes such as die-cast aluminum alloys.

During the injection molding process, molten thermoplastic material containing suspended short glass fibers is pressed into the cavity, where the material then solidifies. The shear flows during filling of the cavity strongly influence the orientation and length of the suspended fibers, which leads to a characteristic microstructure, where fibers exhibit different orientation states in different regions of the geometry and over the thickness of the part. These microstructural properties directly and strongly influence the mechanical properties of the material and, hence, need to be accounted for when developing and dimensioning products. Simulation methods and models are an essential technique to

this end, allowing the behavior of the final product to be predicted and required design changes to be identified at an early stage of the design process.

This work aims at addressing the topic of micromechanical modeling of fatigue in SFRTs by covering three main topics required for such an endeavor.

Microstructural analysis The microstructure of the SFRT part (e.g., fiber orientation, fiber length, volume fractions) needs to be identified by either predictive mold-filling simulations or measurements of real or sample parts. For model development, measurement of specimen parts – e.g., by x-ray micro-computed tomography analyses (µCT) – offer the advantage of more detailed data, not available through simulative approaches. To this end, this work describes a new single fiber segmentation algorithm for SFRT-type materials, which yields the location, orientation, length and diameter of single fibers within a composite specimen.

Micromechanical modeling In order to model the mechanical behavior of SFRTs on the phase level and in order to predict the effective material behavior as a function of microstructural properties, micromechanical modeling or multiscale frameworks need to be used. They allow the scales between microstructure and part geometry to be bridged and yield both the effective behavior of the composite and the loads on the microscopic phases.

Within this work, analytical mean field homogenization schemes are employed. While they have been the subject of extensive research over the years, there still remains the need for a thorough theoretical evaluation and benchmark study. A unified formulation of a set of commonly used schemes is introduced, which can facilitate further comparisons of the models' properties and connections. Secondly, there remains the need for study on the influence of different levels of microstructural fidelity on model predictions, covering the common description using fiber

orientation tensors (e.g., from mold filling simulations) to the inclusion of raw µCT data.

As the simulation of full parts requires efficient modeling frameworks, this work also includes a comparison of different methods of including microstructural information, including a more recently published efficient adaptive integration algorithm.

Fatigue modeling In order to successfully apply SFRTs in the production of real parts, both robust and cost-efficient production processes as well as efficient and accurate simulation models for any field-relevant loading scenarios are required. The prediction of the load limits for parts under high cycle fatigue loading remains an especially challenging task, as it depends on a multitude of factors. This work therefore introduces a progressive cyclic damage model which aims at tackling the topic by modeling the damage processes at the microscale. The matrix model is based on the paper of Peerlings et al. (2000). An extension to the original equations is necessitated by the fact that the reinforcing fibers and the resulting heterogeneous stress and damage state need to be accounted for. Therefore, a coupling term relating the rate of matrix damage to the fiber damage state was developed, as microscopic damage zones can act as stress concentrations, further increasing micro- and mesoscopic damage processes. With respect to this local fiber-related damage, an anisotropic quasi-static damage model was developed.

1.2 Objectives and originality of this thesis

Objectives. The overall objective of this thesis is to develop a micromechanical framework for modeling fatigue in short glass fiber reinforced thermoplastic composites (SFRTs). More specifically, the aim is to account for the microstructure of the given material class, incorporate this data into a multi-scale modeling framework and thereby allowing the

microstructure-dependent fatigue behavior of SFRT parts to be modeled. This integrative simulation chain is covered in three steps:

1. First, a method for extracting statistical microstructure information from x-ray micro-computed tomography (µCT) scans is developed. This so-called single fiber segmentation algorithm can be used to analyze the microstructure of composite specimens. The resulting data – such as fiber orientation and length distributions – is needed to accurately model the mechanical behavior of the composite on specimen level, especially for model development and validation. In industrial product development environments, where µCT scans might not be available, this data is also often obtained from mold-filling simulations.
2. Using the obtained microstructural information one can then employ multi-scale modeling frameworks, such as mean field homogenization schemes. Hence, the second main topic of this research deals with this class of models and their application to the material class at hand. Different common mean field models are introduced and compared using experimental data. A unified algebraic formulation for the models is developed that allows light to be shed on under-reported connections between them and their limitations.
3. Finally, the strength of the composite material under high cycle fatigue loading is modeled using a progressive damage model for the matrix and reinforcing fibers. The model is implemented both for single-element computations as well as for 3D simulations using the finite element solver *Abaqus*. Using the microstructural data and employing the Two-Step homogenization framework, the S-N curves of different composite grades and for two fiber orientation states are modeled.

Originality of this thesis. The research presented in this thesis contains the following novel insights, models and algorithms:

- **Segmentation algorithm:** A novel single fiber segmentation (SFS) algorithm is proposed that uses a series of standard image modification techniques to separate the fiber and matrix domains robustly. In a second step, any over-segmented regions (i.e., fiber erroneously split in the first step) are reconnected using a set of geometric rules. As a result, each fiber's orientation, length, diameter and location are retrieved.
- **Correlation of fiber orientation and length distributions:** The microstructural information from the SFS process allows the correlation of fiber length and orientation to be studied. It is shown that very short fibers tend towards a more random fiber orientation state, whereas long fibers within the same layer of a composite specimen show a nearly unidirectional alignment.
- **Unified formulation of mean field models:** A unified algebraic structure for the Mori-Tanaka (Mori and Tanaka, 1973; Benveniste, 1987), Interaction Direct Derivative (Zheng and Du, 2001), Ponte Castañeda-Willis (Ponte Castañeda and Willis, 1995) and Two-Step (Pierard et al., 2004) schemes is suggested, in which the Polarization tensor is highlighted as the main distinguishing factor. This clarifies connections and differences between the models (especially for the Interaction Direct Derivative scheme), which have remained ambiguous and opaque in the literature.
- **Comparison of fiber orientation integration methods:** Both a regular integration scheme and the adaptive integration scheme of Goldberg et al. (2017) are employed to integrate over the fiber orientation distribution function and the results are compared with respect to the computational effort.
- **Influence of microstructural description:** Using the detailed microstructural data from the SFS algorithm the predictions of the mean field models for different levels of microstructural fidelity are compared: from single layer and average values to a multilayer setup

with each single fiber being accounted for. These predictions are compared to experimental data, highlighting which factors play a dominant role.

- **Anisotropic fiber damage model:** A probabilistic fiber damage model is proposed, that uses the Tsai-Wu failure function (Tsai and Wu, 1971) to account for the pressure-dependent and anisotropic failure envelope of the fiber and its interface. This approach reduces the computational burden when compared to approaches that evaluate the interfacial stress for different surface normals of the fiber interface.
- **Matrix fatigue damage model:** A matrix fatigue damage model is proposed based on the quasi-brittle damage model of Peerlings et al. (2000), which is employed to model the cyclic progressive damage of the matrix material within the multiscale framework. A modification to the original formulation is presented that accounts for the influence of the fiber volume fraction and of the damage state of the fiber domain on the matrix damage process. Through this procedure it is possible to identify a single model parameter set which is applicable to different fiber volume fractions, including pure (i.e., unreinforced) matrix material.

1.3 State of the art

Microstructural characterization of SFRTs[1]

Research has shown that the microstructure of SFRCs greatly influences the final mechanical properties of the composite (Fu and Lauke, 1996; 1998; Fu et al., 2000; Belmonte et al., 2017a). Hence, in order to accurately

[1] This section is based on the publication "Microstructural analysis of short glass fiber reinforced thermoplastics based on x-ray micro-computed tomography" (Hessman et al., 2019), with some minor typographical and formatting changes to improve the readability and coherence within this thesis.

model such materials, a sound knowledge of the microstructural morphology is of paramount importance. While simulation models and tools for predicting the fiber orientation and length distributions based on the part geometry and process parameters do exist, limitations persist with regard to the obtained accuracy. Often, these limitations render them inadequate for research purposes and the development of new material models in the context of structural simulation. Therefore, image-based analyses of composite materials have been of consistent importance, with methods being developed and improved over many decades.

Earlier ones relied on stereological measurements on micrographs of cut and polished specimens (Fakirov and Fakirova, 1985; Fischer et al., 1990; Bay and Tucker III, 1992; Davidson et al., 1997; Blanc et al., 2006). In addition to the fact that such methods are destructive, they have the disadvantage of requiring fibers to be accurately tracked through multiple cuts in order to measure a fiber's length and resolve the three-dimensional orientation (Davidson et al., 1997). Improvements were suggested such as the orientation analysis by confocal laser scanning microscopy (Clarke et al., 1995; Eberhardt et al., 2001). Nonetheless, the mentioned methods suffer from complicated processing and are generally not easily automated.

With the improvement and broader availability of high-resolution x-ray micro-computed tomography (µCT), the analysis of fully three-dimensional fiber morphologies has gained importance (de Paiva et al., 1996; Shen et al., 2004) and is now commonly used. At spatial resolutions below $1\,\mu\mathrm{m}$, such methods yield results with unprecedented accuracy and spatial fidelity (Salaberger et al., 2011). Nevertheless, difficulties in correctly separating fibers in the 3D images as well as the high computational effort still pose noteworthy limitations.

A first class of µCT analysis workflows relies on local voxel-wise filters and operations. Robb et al. (2007) and Wirjadi (2009) used the anisotropic Gaussian filter with varying orientations to assess the local orientation

and applied their method at spatial resolutions of $3.5\,\mu m$ and $0.7\,\mu m$, respectively. Axelsson (2008) used a similar approach, but substituted a phase-invariant quadrature filter to estimate the local orientation of synthetically generated and real material images. Lastly, Krause et al. (2010) applied the structure tensor to extract local orientations. A comprehensive overview and evaluation of these methods is given in Pinter et al. (2018). All methods have the advantage of not requiring fibers to be separated from one another, making them reliable and less prone to under- or over-segmentation. On the other hand, they do not readily yield information about a single fiber, such as its length or position.

So-called medial axis or skeletonization methods are an alternative. Yang and Lindquist (2000) describe such a method and analyzed the microstructure of a polymer fiber mat. Eberhardt and Clarke (2002) extracted orientation information on a regular grid and combine them to obtain a curvilinear centerline description of the fibers. A noteworthy disadvantage of the above mentioned methods is the loss of any fiber radius information due to the thinning process and the often difficult resolution of junctions.

More recently, Salaberger et al. (2011; 2015) suggested two methodologies allowing for a single fiber segmentation based on global thresholding and local orientations. A stochastic model-based algorithm was used by Glöckner et al. (2016) to determine both the orientation and length of the fibers in various polypropylene and polybutylene terephthalate short glass fiber composites. Their iterative procedure consists of pattern matching using cylinder integrals and consolidation steps.

Most commercial µCT software packages also include algorithms for automatic or semi-automatic analysis, often relying on a voxel-wise orientation approach and remaining limited with regard to detailed single fiber information.

Multiscale Models for SFRTs[2]

Different types of multi-scale frameworks exist and are employed for various material classes and applications. On the one hand, mean field (or analytical) homogenization schemes aim at modeling the heterogeneity of the material using fundamental mathematical relations and geometric assumptions, yielding averaged, analytical and often explicit models (cf. Hill (1963), Mori and Tanaka (1973), Willis (1981), Benveniste (1987) and Pierard et al. (2004), among others). On the other hand, numerical homogenization approaches account for a specific and geometrically resolved microstructure and solve for the microscopic fields directly using different numerical schemes. There has been an enormous increase in their use, especially due to the development of highly efficient FFT-based solvers (Moulinec and Suquet, 1998; Eyre and Milton, 1999; Spahn et al., 2014; Schneider et al., 2016), model order reduction techniques (Michel and Suquet, 2003; Fritzen and Böhlke, 2011; Wulfinghoff et al., 2018). More recently, data-driven modeling concepts using Deep Material Networks have shown to be very promising for both linear and non-linear composite behavior (Liu et al., 2019; Liu and Wu, 2019; Gajek et al., 2020) Nevertheless, analytical mean field homogenization schemes continue to play a central role in modeling heterogeneous materials, especially SFRCs. The availability of different commercial implementations has also lead to an increased use of these models in industry.

Different authors have published comparisons of mean field schemes, also in the context of short fiber reinforced composites. Tucker III and Liang (1999) gave extended overview of modeling approaches for unidirectional short fiber composites. More recently, Müller et al. (2015)

[2] This section is based on the publication "On mean field homogenization schemes for short fiber reinforced composites: Unified formulation, application and benchmark" (Hessman et al., 2021), with some minor typographical and formatting changes to improve the readability and coherence within this thesis.

compared mean field models to numerical (FFT) results for different short glass fiber reinforced polypropylene composites and Müller et al. (2016) used measured microstructural data to compute effective elastic properties and compared them to experimental results. Klusemann and Svendsen (2010) studied many schemes for application with particle reinforced materials. In a related work Naili et al. (2020) compared different homogenization schemes using full-field finite element analyses of unit cell and representative volume element models. Fewer results have been published on the prediction of phase stresses and strains within a composite material by mean field schemes (e.g. Jain et al., 2013).

Damage & fracture processes in SFRTs[3]

Due to the inherently complex microstructure of SFRCs and the influence it has on all types of mechanical properties, a thorough understanding of the microstructural morphology is indispensable, and has increasingly been the focus of academic and industrial research. This includes the effects of fiber length and orientation on the material strength (Fu and Lauke, 1996; Fu et al., 1999), studies how the microstructure affects fatigue strength (Bernasconi et al., 2007; De Monte et al., 2010a;c;b; Belmonte et al., 2014; Wilmes and Hornberger, 2015; Belmonte et al., 2017a), methods for determining the local fiber orientation (Bernasconi et al., 2008; Hessman et al., 2019) and publications on analyzing local damage phenomena in the microstructure (Arif et al., 2014; Rolland et al., 2016; 2018).

With respect to micromechanical failure processes, studies such as Sato et al. (1991) and Rolland et al. (2016) have shown that the damage processes within SFRCs are greatly influenced and even nucleate at or in the vicinity of the reinforcing fibers. Using in-situ synchrotron

[3] This section is based on the publication "A micromechanical cyclic damage model for high cycle fatigue failure of short fiber reinforced composites" (Hessman et al., 2023), with some minor typographical and formatting changes to improve the readability and coherence within this thesis.

x-ray microtomography to study the fatigue damage in an SFRT composite, Rolland et al. (2018) showed that the damage processes consist of cavitation in the matrix, damage and debonding of the fiber ends, fiber fracture, debonding of the tangential fiber-matrix interface, matrix crazing, microcracks and finally mesocracks. Belmonte et al. (2017b) studied damage initiation under fatigue loading in axially loaded PA66-GF35 specimens using electron microscopy of fracture surfaces. They found that the matrix fractured in a micro-ductile manner during stable fatigue crack propagation and brittle fracture occurred during unstable crack propagation. Furthermore, matrix cavities were found ahead of the propagating crack tip. The initiation of damage was also linked to the presence of nano-voids around nano-particles. In Belmonte et al. (2017a) the same authors studied the influence of the glass fiber volume fraction for different PA66-based composites. Again using specimens loaded along the main fiber direction, they observed an increased fatigue strength for higher volume fractions. Furthermore, the fraction of fatigue life associated with fatigue crack propagation was shown to also increase with the fiber volume fraction. Fatigue damage was also shown to initiate as matrix cavitation around particles and to be strongly influenced by the fiber-induced local stress state.

Fiber-related damage modeling for SFRTs[4]

For fiber and fiber-interface failure, Fitoussi et al. (1996; 1998) suggested a model which combines the Mori-Tanaka homogenization method and a statistical micromechanical damage model for Sheet Molding Compound (SMC)-type materials. Therein, interfacial debonding of fibers was described by Coulomb's law and damaged fibers were replaced by an undamaged anisotropic effective material of reduced stiffness.

[4] This section is based on the publication "A micromechanical cyclic damage model for high cycle fatigue failure of short fiber reinforced composites" (Hessman et al., 2023), with some minor typographical and formatting changes to improve the readability and coherence within this thesis.

Similarly, Jain et al. (2015a) model the anisotropic stiffness of SFRCs with debonded fibers using "equivalent bonded inclusions" and the Mori-Tanaka scheme. More recently, Schemmann et al. (2018) applied the Mori-Tanaka scheme to model both matrix damage and fiber debonding in SMC materials. The latter was done by using an effective interface stress and considering a Weibull-distributed interfacial strength.

Fatigue damage modeling for SFRTs[5]

Different approaches have been suggested for modeling high cycle fatigue in short fiber composites. Krairi and Doghri (2013) and Krairi et al. (2016) introduce a mean field homogenization based approach where damage within so called weak spots is computed and used as an indicator for high cycle fatigue failure. Jain et al. (2015b) suggested a hybrid multiscale method for scaling S-N curves for SFRCs. Pietrogrande et al. (2021) modeled the fatigue life of a SFRT using a two-step approach, computing the cumulative distribution function of the matrix stresses with the FE-based two-step method of Pietrogrande et al. (2018) and using it to calculate an effective matrix stress for scaling S-N curves. Köbler et al. (2021) suggest a cyclic fatigue damage law for an SFRT composite based on Fast Fourier Transformation (FFT) full-field simulations and a model-order reduction method. Recently, Magino et al. (2022a;b) suggested a mean-stress sensitive multiscale model for high cycle fatigue of SFRTs using a cycle-jump approach with a model order reduction scheme.

[5] This section is based on the publication "A micromechanical cyclic damage model for high cycle fatigue failure of short fiber reinforced composites" (Hessman et al., 2023), with some minor typographical and formatting changes to improve the readability and coherence within this thesis.

1.4 Scope of the presented models

This work covers the structural mechanical behavior of short glass fiber reinforced thermoplastic composites on a *macro* scale, where the heterogeneity of the material is accounted for indirectly by employing multi-scale modeling schemes that account for the material structure on the *micro* scale, but yield a homogeneous effective material. This effective material model can then be used to simulate the mechanical behavior of larger parts, as required especially in industrial settings.

To this end, the models are formulated within the context of continuum mechanics. The fundamental balance equations are the balance of mass, balance of linear momentum, balance of angular momentum and the balance of energy. Furthermore, there exist inequalities that give bounds for admissible irreversible (e.g., inelastic) processes, such as the Clausius-Duhem inequality derived from the second law of thermodynamics. Detailed explanations and derivations of these fundamental equations can be found in literature such as Holzapfel (2000) or Bertram (2012), among many others.

Depending on the specific material, especially the specific matrix material employed, and the environmental conditions such as temperature and humidity, the resulting material behavior of SFRTs can range between quasi-brittle and ductile. This work focuses on the effective elastic properties and the high cycle fatigue behavior of dried (i.e., low moisture content) SFRT composites. Under these circumstances and within this scope one can consider the material to behave in a quasi-brittle manner. Therefore, we restrict ourselves to the realm of small deformations.

1.5 Outline of the thesis

In addition to the introductory chapter, this work contains five additional chapters, of which three chapters are based on published journal arti-

cles covering the three main subtopics: microstructure characterization (Hessman et al., 2019), micromechanical modeling of the elastic behavior (Hessman et al., 2021), and finally the micromechanical modeling of fatigue (Hessman et al., 2023).

Chapter 2 gives an overview of the fundamentals of short fiber reinforced thermoplastics, including injection molding, the resulting microstructure and methods to quantitatively describe the microstructure, such as fiber orientation tensors and orientation distribution functions.

Chapter 3 (Hessman et al., 2019) covers a methodology to analyze the microstructure of SFRTs using x-ray micro-computed tomography. It contains a novel single fiber segmentation algorithm which enables detailed microstructural analyses. Relevant implementation details are provided and a model validation using artificial and experimental data is discussed.

In Chapter 4 (Hessman et al., 2021) different analytical homogenization methods are compared and discussed. Using the previously obtained microstructural data, the predictions for the elastic properties and of phase stresses and strains are compared. To this end, results from experimental tests and full-field homogenization methods are considered.

Building on the findings of the two previous chapters, Chapter 5 (Hessman et al., 2023) introduces a micromechanical cyclic damage model for high cycle fatigue. The model equations are discussed, including a novel adaptation to the damage formulation that accounts for a material-specific aspect of the fatigue behavior. The algorithm is explained and the parameter identification procedure is outlined. The predicted fatigue behavior is compared using experimental data.

Chapter 6 gives a brief summary of the topics of this work and key findings, as well as possible future paths for subsequent research in these fields.

To improve the readability of the thesis, the original introductory sections and selected method sections of the three publications have been

combined into the joint fundamentals and introduction chapters of this work. These individual sections and their respective source publications are highlighted using footnotes. New introduction sections were added to Chapters 3, 4 and 5 to link them within the overall thesis.

Some figures and tables from the original publications were rearranged or reformatted to fit the thesis form and footnotes were added to add context or highlight minor modifications.

1.6 Notation

Within this thesis a direct tensor notation is preferred. Scalar variables are written as lowercase Latin or Greek letters (e.g., a or σ). Vectors are written as lowercase bold Latin letters (e.g., $\boldsymbol{a}$), whereas second-order tensors are denoted with uppercase bold Latin or lowercase bold Greek letters (e.g., $\boldsymbol{A}$ or $\boldsymbol{\sigma}$). Fourth-order tensors are finally represented by uppercase blackboard bold Latin letters (e.g., $\mathbb{A}$). The scalar product is written by a single dot (e.g., $\boldsymbol{a} \cdot \boldsymbol{b}$), the dyadic product is given as $\boldsymbol{a} \otimes \boldsymbol{b}$ and the notation $\boldsymbol{a}^{\otimes n}$ is introduced as shorthand for the $(n-1)$-times dyadic product of tensor $\boldsymbol{a}$: $\boldsymbol{a} \otimes \boldsymbol{a} \otimes ... \otimes \boldsymbol{a}$. Linear mappings of a second-order tensor by a fourth-order tensor are written as $\boldsymbol{A} = \mathbb{B}[\boldsymbol{C}]$, whereas the double contraction of two fourth-order tensors is denoted by $\mathbb{A} = \mathbb{B}\mathbb{C}$. Finally, the fourth-order symmetric identity tensor $\mathbb{I}^{\mathrm{S}} = 1/2(\delta_{ik}\delta_{jl} + \delta_{il}\delta_{jk})\, \boldsymbol{e}_i \otimes \boldsymbol{e}_j \otimes \boldsymbol{e}_k \otimes \boldsymbol{e}_l$ is introduced.

Chapter 2

Fundamentals of short fiber reinforced thermoplastics

2.1 Injection molding of SFRTs[1]

Injection molding is arguably the most common industrial production process for short fiber reinforced thermoplastics. Its main characteristics are the filling of a mold cavity with molten thermoplastic material containing the suspended fibers. The process is shown schematically in Fig. 2.1 and comprises the following steps (Domininghaus et al., 2012):

1. Melting of the thermoplastic granules via heating elements in the nozzle and by frictional heat introduced by the rotating screw in the plastification unit.
2. Injection of the molten thermoplastic into the closed mold cavity (step a).
3. Packing and holding stage (step b), where the final filling occurs and any shrinkage is compensated.
4. Cooling of the part, opening of the mold and ejection of the final part (step c).

[1] This section contains a paragraph from the publication "Microstructural analysis of short glass fiber reinforced thermoplastics based on x-ray micro-computed tomography" (Hessman et al., 2019), with some minor typographical and formatting changes to improve the readability and coherence within this thesis.

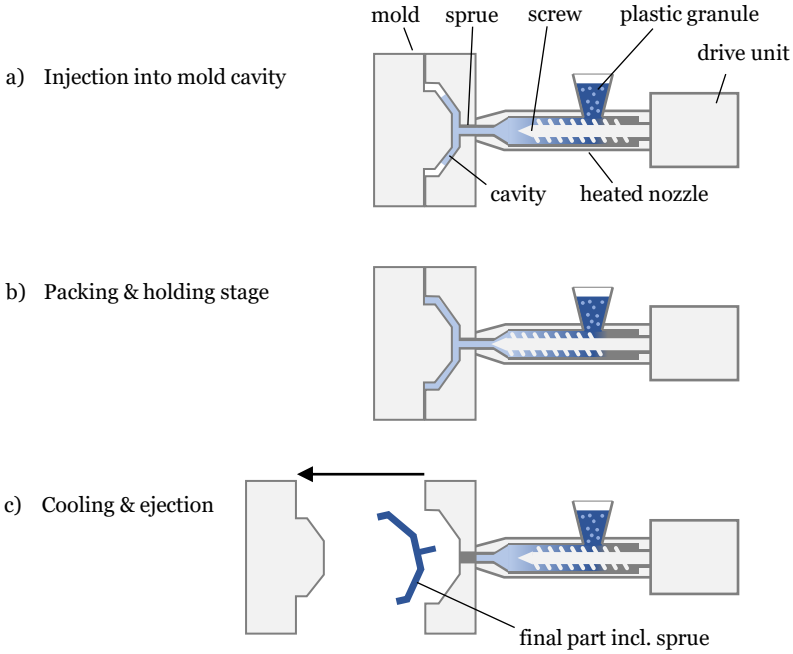

Figure 2.1: Schematic representation of the injection molding process.

During the injection molding process, the glass fibers rotate and align according to the shear flow in the cavity, resulting in a heterogeneous and complex fiber orientation state in the final part (Folgar and Tucker III, 1984; Fakirov and Fakirova, 1985). In addition, longer fibers are broken down due to the high shear stresses and fiber-fiber contact in the plastification unit and in the cavity, leading to non-uniform fiber lengths (von Turkovich and Erwin, 1983). A segregation of fibers due to the state of flow can lead to spatially varying fiber volume fractions (Rolland et al., 2016).

2.2 Quantitative description of SFRT microstructures[2]

As this work is concerned with *short* glass fiber reinforced thermoplastics, it is helpful to restrict ourselves to straight fibers that can be conveniently represented by cylinders of length l, diameter d and orientation $\boldsymbol{p} \in \mathcal{S} \coloneqq \{\boldsymbol{p} \in \mathbb{R}^3 \,|\, \|\boldsymbol{p}\| = 1\}$ (cf. Fig. 2.2). The orientation can also be specified using the azimuth ϕ and polar angle θ. For material modeling purposes, the aspect ratio $a = l/d$ will become a central measure.

In order to describe the material's local fiber orientation state, we can introduce the fiber orientation distribution function (FODF) ψ_p which relates an orientation $\boldsymbol{p}$ to its occurrence probability. The fundamental

[2] This section, including the figure, is based on the publications "Microstructural analysis of short glass fiber reinforced thermoplastics based on x-ray micro-computed tomography" (Hessman et al., 2019) and "On mean field homogenization schemes for short fiber reinforced composites: Unified formulation, application and benchmark" (Hessman et al., 2021), with some minor typographical and formatting changes to improve the readability and coherence within this thesis.

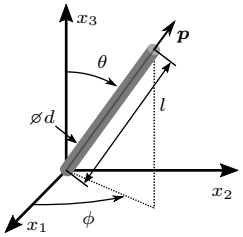

Figure 2.2: Orientation of a fiber in spherical coordinates.

properties of ψ_p can be summarized as follows

$$\begin{aligned} &\oint_{\mathcal{S}} \psi_p(\boldsymbol{p})\,\mathrm{d}\boldsymbol{p} = 1, \\ &\psi_p(\boldsymbol{p}) \geq 0 \quad \text{and} \quad \psi_p(\boldsymbol{p}) = \psi_p(-\boldsymbol{p}). \end{aligned} \tag{2.1}$$

Fiber orientation tensors are a convenient description the fiber orientation distribution that represent the distribution's leading statistical moments (Kanatani, 1984; Advani and Tucker III, 1987). Their application has become very common in the field of composite homogenization (e.g. Buck et al., 2015; Müller and Böhlke, 2016; Köbler et al., 2018). The n-th order fiber orientation tensor $\mathcal{N}^{\langle n \rangle}$ can be related to the FODF by

$$\mathcal{N}^{\langle n \rangle} = \oint_{\mathcal{S}} \boldsymbol{p}^{\otimes n}\, \psi_p(\boldsymbol{p})\,\mathrm{d}\boldsymbol{p}, \tag{2.2}$$

where $\otimes n$ symbolizes the $(n-1)$-times dyadic product.

In order to also take into account the distribution of fiber length and diameter, the joint probability function $\psi(\boldsymbol{p}, l, d)$ can be defined (cf. Bay and Tucker III, 1992)

$$\int_d \int_l \oint_{\mathcal{S}} \psi(\boldsymbol{p}, l, d)\,\mathrm{d}\boldsymbol{p}\,\mathrm{d}l\,\mathrm{d}d = 1. \tag{2.3}$$

From the joint probability function we can compute the volume-weighted orientation tensors by

$$\mathcal{N}^{\langle n\rangle} = \frac{\int_d \int_l \oint_{\mathcal{S}} V(l,d)\ \boldsymbol{p}^{\otimes n}\ \psi(\boldsymbol{p},l,d)\ \mathrm{d}\boldsymbol{p}\,\mathrm{d}l\,\mathrm{d}d}{\int_d \int_l \oint_{\mathcal{S}} V(l,d)\ \psi(\boldsymbol{p},l,d)\ \mathrm{d}\boldsymbol{p}\,\mathrm{d}l\,\mathrm{d}d,} \tag{2.4}$$

where $V(l,d) = \pi/4\, d^2\, l$ represents the volume of a cylindrical fiber of length l and diameter d (cf. Bay and Tucker III, 1992).

An example for the correlation of fiber length and orientation can be found in Hessman et al. (2019)[3]. Unfortunately, due to a lack of microstructural insight, $\psi(\boldsymbol{p},l,d)$ is often not available and the length distribution ψ_l is analyzed and accounted for separately. In such cases, one can resort to using a fixed fiber diameter and computing $\psi(\boldsymbol{p},l) = \psi_p(\boldsymbol{p})\,\psi_l(l)$ under the assumption of stochastic independence.

With a set of discrete fibers or fiber orientations $\boldsymbol{p}_\alpha$ with associated volumes $V_\alpha = \pi/4\, d_\alpha^2\, l_\alpha$, the n-th order fiber orientation tensor can then be computed using

$$\mathcal{N}^{\langle n\rangle} = \frac{1}{V_\mathrm{F}} \sum_{\alpha=1}^{N} V_\alpha \boldsymbol{p}_\alpha^{\otimes n}, \qquad V_\mathrm{F} = \sum_{\alpha=1}^{N} V_\alpha. \tag{2.5}$$

[3] cf. Chapter 3 of this thesis

Chapter 3

Microstructural analysis of short glass fiber reinforced thermoplastics based on x-ray micro-computed tomography[1]

3.1 Introduction

This chapter deals with the analysis of the microstructure of short glass fiber reinforced thermoplastics (SFRTs). A novel µCT segmentation algorithm is presented, with which the microstructural characteristics of single fibers within a composite specimen can be obtained. This data is then used to derive statistical metrics, which in turn can be used to model the composite in multi-scale methods. Artificially generated µCT scan images are employed to validate the approach and the segmentation results of different real µCT scans are compared to fiber orientation tensors from commercial software and a fiber length distribution from an incinerated specimen. Finally, the method is also tested for a high volume fraction PA66-GF50 composite.

[1] This chapter, including all tables and figures, is based on the publication "Microstructural analysis of short glass fiber reinforced thermoplastics based on x-ray micro-computed tomography" (Hessman et al., 2019), with some minor typographical and formatting changes to improve the readability and coherence within this thesis.

Chapter structure

The chapter is structured in three parts. First, in Section 3.2, the material considered, all used experimental data and artificially generated µCT scans are provided. In Section 3.3, the developed segmentation algorithm is introduced and explained. This includes the different steps, algorithmic details and the implementation. The following Section 3.4 covers the results. First, the algorithm is validated using artificial µCT data and the sensitivity with respect to the spatial resolution is studied. Afterwards, the results of the full specimen scans are presented and discussed. Finally, the conclusions of the chapter are summarized in Section 3.5.

3.2 Materials and methods

3.2.1 Composite material and specimens

In this work a commercial-grade short glass fiber reinforced polyamide 6.6 with a fiber mass fraction of $35\,\%$ (PA66-GF35) is studied. Given a polyamide 6.6 matrix density of $1.13\,\mathrm{g\,cm^{-3}}$ and a glass fiber density of $2.55\,\mathrm{g\,cm^{-3}}$, the resulting composite fiber volume fraction is approximately $19.3\,\%$. The material was injection molded into a plate cavity with dimensions $120 \times 80 \times 2\,\mathrm{mm^3}$, as shown in Fig. 3.1.

The specimens used for the µCT scans were cut out of these plates at a location $40\,\mathrm{mm}$ from the gate, equivalent to the middle section of potential tensile specimens.

In addition to the µCT scans, the fiber length distribution for one cuboid specimen was determined experimentally. The polymeric matrix was removed by incineration and the remaining fibers were measured using an optical microscope and an automated workflow.

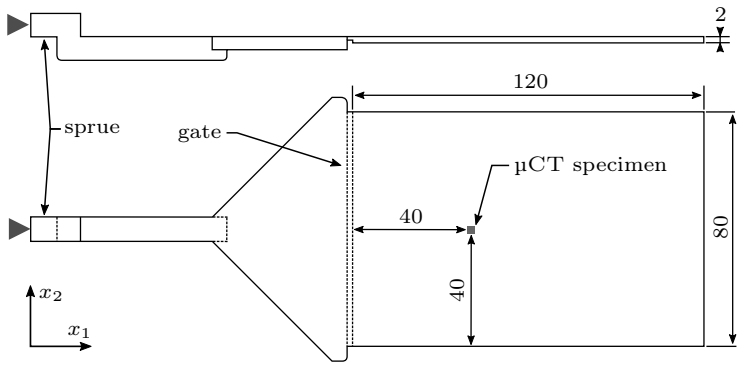

Figure 3.1: Drawing of the plate geometry and specimen location (units in mm).

3.2.2 X-ray micro-computed tomography

To obtain accurate 3D images of the microstructure, a high resolution x-ray micro-computed tomography system *Zeiss Xradia 520 Versa* with a $160\,\mathrm{kV}$ x-ray tube was used (see Fig. 3.2). With a 2000×2000 pixel detector, images with a size of up to 2000^3 voxels and a spatial resolution as low as $0.4\,\mu\mathrm{m}$ can be achieved. Naturally, the overall sample size and the obtained resolution are adversarial goals. Therefore, an intermediate resolution of $1\,\mu\mathrm{m}$ was chosen for the full height scans, which leads to images of up to $(2000\,\mu\mathrm{m})^3$. As will be shown further below, such scans yield the required spatial details while ensuring representative sets of more than 20,000 fibers and covering the entire thickness of the used plate.

3.2.3 Scans of the composite material

Three full height µCT specimens of PA66-GF35 were prepared and scanned for this work, which shall be referred to as *Scan 1*, *Scan 2* and *Scan 3*. The first two were cut from two different plates at exactly the

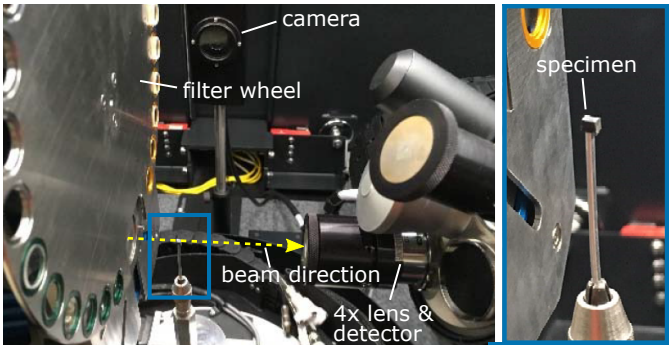

Figure 3.2: Pictures of the cuboid specimen in the µCT scanner.

position marked in Fig. 3.1 whereas *Scan 3* was cut out directly next to *Scan 2* with a minimal offset in x_1-direction. A rendering of *Scan 3* is shown in Fig. 3.3.

Each scan took approximately $10\,\mathrm{h}$ to complete during which roughly 3000 projections at $10\,\mathrm{s}$ each were performed. The scan was first processed in the software VGStudio Max (VG, Volume Graphics GmbH, Germany), from which three-dimensional cuboid 16 bit gray scale images were exported. In addition, second-order FOTs were exported using the included analysis functionality and later used as reference values.

In order to study the influence of the spatial resolution, a sub-volume named *region of interest* (*ROI 1.0*) of *Scan 1* was extracted and also scanned at a higher resolution of $0.4\,\mu\mathrm{m}$ (*ROI 0.4*). Finally, a $0.4\,\mu\mathrm{m}$ resolution scan was performed for a specimen of PA66-GF50 with a higher volume fraction of $30.7\,\%$ (*ROI High*) to explore the limitations of the presented algorithm with regard to a higher fiber content. A comprehensive summary of all scan details can be found in Table 3.1.

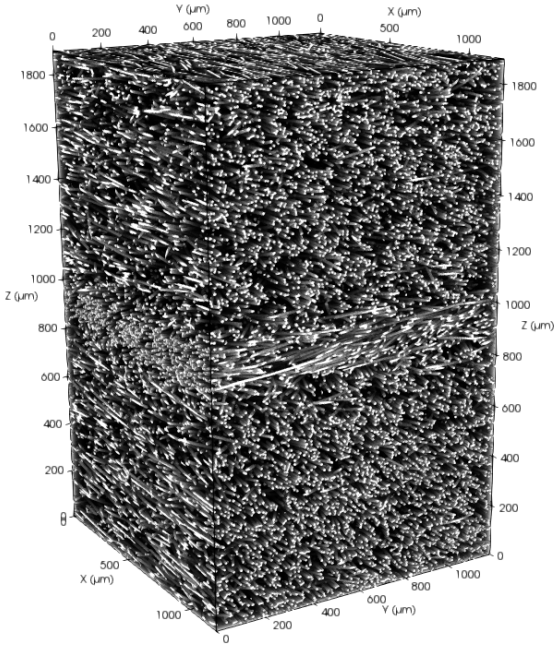

Figure 3.3: Rendering of the PA66-GF35 µCT scan *Scan 3*.

Table 3.1: Summary of all µCT scans used in this work: Full height scans (*Scan*), regions of interest (*ROI*), high volume fraction ROI (*ROI High*) and artificial ground truth data (*GT*).

Scan	Resol.	Material (vol. fraction)	Scan domain in μm^3
Scan 1	1.0 µm	PA66-GF35 (19.3 %)	$1255 \times 1343 \times 1883$
Scan 2	1.0 µm	PA66-GF35 (19.3 %)	$752 \times 1558 \times 1857$
Scan 3	1.0 µm	PA66-GF35 (19.3 %)	$1202 \times 1200 \times 1891$
ROI 1.0	1.0 µm	PA66-GF35 (19.3 %)	$491 \times 494 \times 717$
ROI 0.4	0.4 µm	PA66-GF35 (19.3 %)	$505 \times 511 \times 743$
ROI High	0.4 µm	PA66-GF50 (30.7 %)	$528 \times 515 \times 596$
GT 1.0	1.0 µm	Artificial (19 %)	$400 \times 400 \times 400$
GT 0.4	0.4 µm	Artificial (19 %)	$400 \times 400 \times 400$

3.2.4 Artificial µCT data

In order to validate the proposed algorithm, artificial ground truth (GT) µCT data for an imaginary PA66-GF35 composite was used. First, a reference fiber orientation tensor $\boldsymbol{N}_{\text{ref}} \mathrel{\widehat{=}} \text{diag}(0.66, 0.3, 0.04)$ was chosen. The fiber length and radius were set to constant values of $200\,\mu\text{m}$ and $5\,\mu\text{m}$, respectively, yielding an aspect ratio of 20. Constant values were explicitly chosen to facilitate detection of any mis-segmentation and deviation in length and radius. In order to keep the data as realistic as possible, touching fibers were allowed. To demonstrate that the proposed algorithm correctly accounts for the voxel size, two spatial resolutions of $0.4\,\mu\text{m}$ and $1\,\mu\text{m}$ (*GT 0.4* and *GT 1.0*) were used. The domain size was set to $(400\,\mu\text{m})^3$, resulting in voxel grids of dimensions 1000^3 and 400^3, respectively. The artificial fiber morphology and 3D images were generated up to a nominal volume fraction of $19\,\%$ using the Sequential Addition and Migration (SAM) algorithm (Schneider, 2017) that accurately matched the reference FOT. The resulting 3D image is visualized in Fig. 3.4 and a summary of the setups can be found in Table 3.1.

3.3 Segmentation algorithm

The µCT analysis workflow we are proposing is related to those of Salaberger et al. (2011; 2015) and Glöckner et al. (2016) as far as it relies on a single fiber segmentation and analysis paradigm. The algorithm operates directly on the three-dimensional volume images from µCT scans in order to capture the complex three-dimensional microstructure. This allows for detailed insight into the fiber orientation and arrangements, but comes at the cost of high resolution requirements and often high computational cost (Pinter et al., 2018).

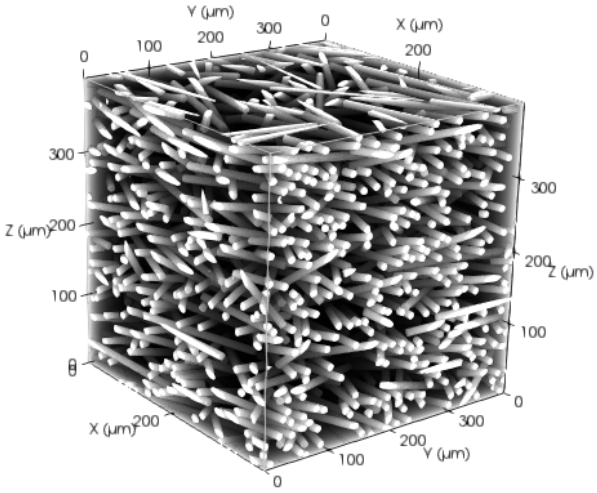

Figure 3.4: Rendering of the artificially generated ground truth microstructure.

The proposed method can be split into three parts, which are explained below. Images at different stages of preparation and processing are shown for two slices in Fig. 3.5.

3.3.1 Image preparation

Before the fibers can be segmented, it is necessary to first preprocess the input gray value image I. Especially for high resolutions images (voxel size below $1\,\mu\mathrm{m}$), it can be advantageous to use smoothing filters such as Gaussian or median filters to reduce the overall noise. Then, in order to both increase the segmentation quality and reduce the overall processing time, smaller fragments and particles need to be removed. In the present work, a morphological opening is used, which consists of an erosion and dilation operation, yielding the filtered image $I_f = I \circ K = (I \ominus K) \oplus K$. The erosion removes structures smaller than the structuring element K and the dilation expands the remaining image

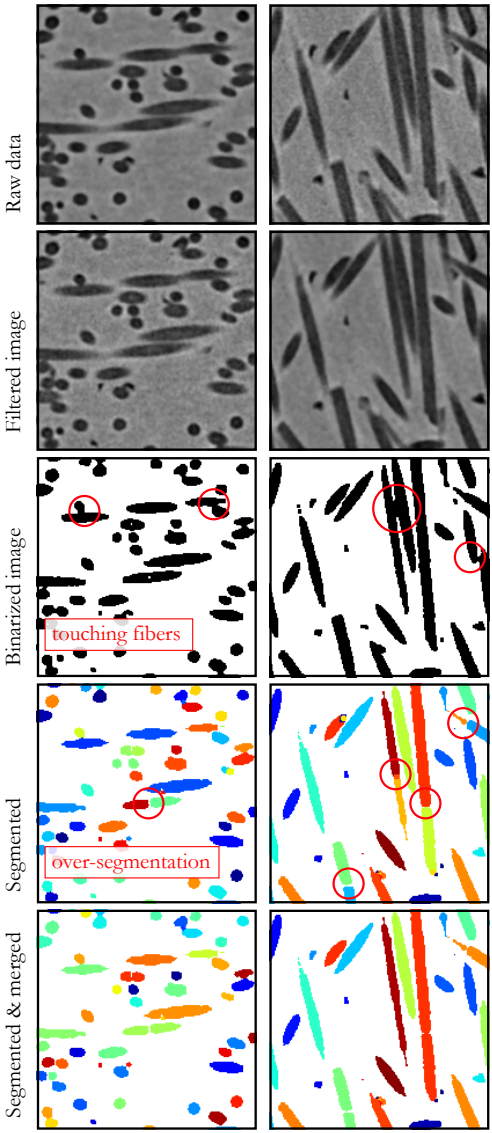

Figure 3.5: Detail slices of $190 \times 190\,\mu m^2$ from a scan at different stages of processing, normal to the x_1-axis (left) and normal to the x_3-axis (right).

again. More details on the filters and operations can be found in Burger and Burge (2009b).

In the next step, a binary representation I_b of the µCT scan is obtained by applying a threshold t, voxels with a gray value above t being considered to be part of a fiber $\Omega_F = \{\boldsymbol{x} \in \mathbb{R}^3 \mid I_b(\boldsymbol{x}) > t\}$. Estimates for t can be obtained by algorithms such as the well-known Otsu's method (Otsu, 1979), but manual adjustment has proven valuable. Good results are typically obtained by setting t such that the resulting image volume fraction corresponds to the fiber volume fraction of the material.

In some cases, the gray values within a fiber can fluctuate. After filtering and binarization, these fluctuations can lead to cavities within the fibers that lead to over-segmentation. In such cases, this is alleviated by means of the flood-fill method (Burger and Burge, 2009a).

3.3.2 Fiber detection

The binarized image I_b typically still contains large regions of connected fibers which need to be separated to allow for a single fiber analysis (cf. Fig. 3.5). For this, an iterative segmentation scheme is proposed. It is outlined in Fig. 3.6 and can be summarized as follows: To separate the fibers all fiber domains are iteratively shrunk, labeled, expanded again, and finally evaluated. Correctly detected single fiber regions are extracted before performing another iteration on the remaining fiber domains. The different steps are detailed below.

Given the image I_b, an erosion $J = I_b \ominus K(k)$ with an increasing size of the structuring element is performed, starting at $k = 0$ (no erosion) up to k_{max}. For each resulting image J, all N contiguous fiber regions are labeled, yielding the label image $\tilde{L}$. The constant-value regions in $\tilde{L}$ now constitute fiber candidates $\Omega_l = \{\boldsymbol{x} \in \mathbb{R}^3 \mid \tilde{L}(\boldsymbol{x}) = l\}$. Due to the erosion, these regions are increasingly shrunk and thereby separate from neighboring clusters enabling the single fiber segmentation. To restore

nearly the original fiber volume, a dilation of the labeled image is then performed $L = \tilde{L} \oplus K(k)$, after which fibers may touch again but remain separated due to their labels. For clarity, the fiber candidate index l is dropped in the following description.

Next, the contiguous domains are evaluated to assess whether they constitute proper single fibers. Each candidate is evaluated utilizing the inertia tensor $\boldsymbol{L}_\Omega$

$$\boldsymbol{L}_\Omega = \sum_{i=1}^{n} [(\tilde{\boldsymbol{x}}_i \cdot \tilde{\boldsymbol{x}}_i)\boldsymbol{I} - \tilde{\boldsymbol{x}}_i \otimes \tilde{\boldsymbol{x}}_i] \quad \text{with} \quad \tilde{\boldsymbol{x}}_i = \boldsymbol{x}_i - \bar{\boldsymbol{x}} \tag{3.1}$$

and its spectral representation

$$\boldsymbol{L}_\Omega = \sum_{I=1}^{3} \lambda_I \boldsymbol{v}_I \otimes \boldsymbol{v}_I. \tag{3.2}$$

where $\boldsymbol{I} = \delta_{ij} \boldsymbol{e}_i \otimes \boldsymbol{e}_j$ denotes the second-order identity tensor, $\boldsymbol{x}_i \in \Omega$ represent the location of voxel i and $\bar{\boldsymbol{x}}$ is the fiber center of gravity (COG). The underlying assumption is that the fiber's main axis $\boldsymbol{p}$ is accurately predicted by the region's principal axis $\boldsymbol{v}_1$, belonging to the smallest eigenvalue λ_1.

Once the fiber main axis is retrieved, the fiber length can be measured by the distance of the two points that are furthest away from the COG when projected onto the fiber axis, which shall be referred to as $\boldsymbol{a}$ and $\boldsymbol{b}$. This is sketched in Fig. 3.7

$$l = \max_i (\boldsymbol{x}_i \cdot \boldsymbol{p}) - \min_i (\boldsymbol{x}_i \cdot \boldsymbol{p}). \tag{3.3}$$

This method, similar to that of Salaberger et al. (2011), neglects the fibers' possible curvature by projecting all voxel coordinates onto the principal axis, leading to an error that increases with the ratio of fiber length to radius of curvature. Since the algorithm is dedicated to short fibers and

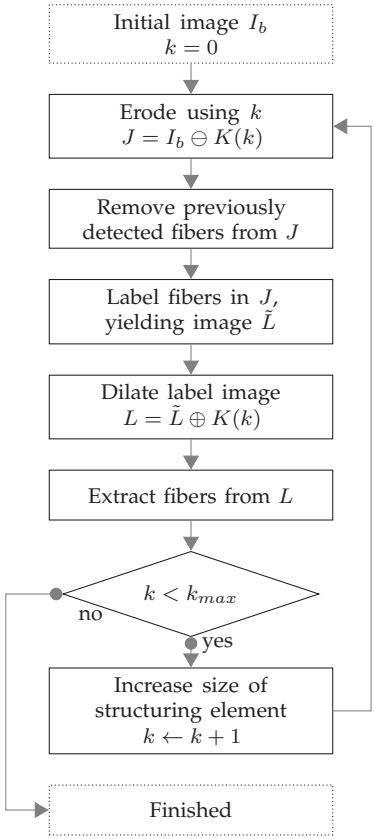

Figure 3.6: Flow chart of the segmentation algorithm.

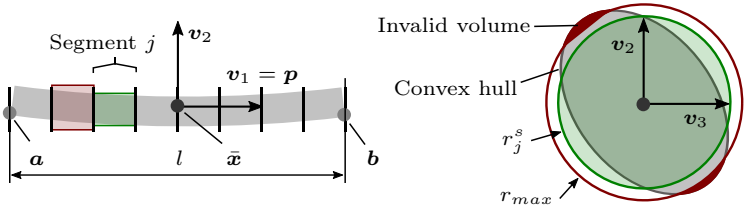

Figure 3.7: Schematic of the fiber length, radius and error estimation of a fiber candidate with exaggerated curvature.

since their curvature is sufficiently small (Bay and Tucker III, 1992), this effect can be neglected.

Detecting the fiber radius r is not as straightforward. It is done by defining multiple fiber segments along the main axis. For each segment (index j), all voxels' centroid coordinates are projected onto the fiber's transverse plane ($\boldsymbol{v}_2$-$\boldsymbol{v}_3$). The segment radius r_j^s is then defined as the radius of a circle with the same area as the convex hull of all segment points when projected onto the $\boldsymbol{v}_2$-$\boldsymbol{v}_3$ plane (see Fig. 3.7)

$$r = \frac{1}{m}\sum_{j=1}^{m} r_j^s \qquad \text{with} \qquad r_j^s = \sqrt{\frac{1}{\pi} A_j^{hull}}. \tag{3.4}$$

This segment-wise approach also allows for a detection error estimate $e \in [0;1]$. It is defined segment-wise as the fraction of volume (or voxels) that lies outside of an imaginary cylinder with radius r_{max} (typically $8\,\mu\mathrm{m}$), orientation $\boldsymbol{p}$ and located in the segment's center of gravity (cf. Fig. 3.7). If the overall error e remains below a predefined tolerated error, then the fiber candidate is accepted. Successfully detected fibers are saved as tuples $f = (\bar{\boldsymbol{x}}, \boldsymbol{a}, \boldsymbol{b}, \boldsymbol{p}, l, r)$ and their voxel region Ω is removed from the original Image I_b, thereby not entering the analysis again.

The above given steps are repeated until all fiber candidates have been processed. In case all candidates are found to represent valid fibers, the

detection algorithm stops. Otherwise, if $k + 1 < k_{max}$ holds, the structuring element is enlarged ($k \leftarrow k + 1$) and the workflow is repeated.

3.3.3 Fiber merging

In cases where large fiber clusters with many touching points are encountered, large erosion kernels need to be used. This can lead to an over-segmentation, where fibers are broken down into multiple fragments, leading to an erroneous prediction of the length distribution. To account for this effect, a fiber merging algorithm is proposed.

After successful completion of the fiber detection, the merging algorithm searches for fragment pairs (f_i, f_j) that fulfill all of the following coaxiality and proximity conditions

$$\begin{aligned} \arccos(|\boldsymbol{p}_i \cdot \boldsymbol{p}_j|) &< \alpha_{max}, \\ \arccos(|\Delta\bar{\boldsymbol{x}}_{ij} \cdot \boldsymbol{p}_i|) &< \alpha_{max}, \\ \arccos(|\Delta\bar{\boldsymbol{x}}_{ij} \cdot \boldsymbol{p}_j|) &< \alpha_{max}, \\ \min(|\boldsymbol{a}_i - \boldsymbol{a}_j|, |\boldsymbol{a}_i - \boldsymbol{b}_j|, |\boldsymbol{b}_i - \boldsymbol{b}_j|) &< d_{max}, \\ \text{with } \Delta\bar{\boldsymbol{x}}_{ij} = \frac{\bar{\boldsymbol{x}}_j - \bar{\boldsymbol{x}}_i}{|\bar{\boldsymbol{x}}_j - \bar{\boldsymbol{x}}_i|}&. \end{aligned}$$

Here, the maximum deviation angle α_{max} and the maximum distance d_{max} are parameters with typical values being $\alpha_{max} = 10°$ and $d_{max} = 10\,\mu\mathrm{m}$ for the material at hand. If a pair is detected, the fiber characteristics are merged and the process is repeated until no more fragment pairs are found. In the end, all fibers below a minimum length of $30\,\mu\mathrm{m}$ were discarded to sanitize the final fiber dataset and to remove non-fiber particles (cf. Salaberger et al. (2015)).

3.3.4 Implementation

The algorithm was implemented in the *Python* programming language to facilitate extensibility and fully automated application. Extensive use was made of the *scikit-image* (van der Walt et al., 2014) and *scipy* (Jones et al., 2001) packages for image processing. It is important to note that due to the high resolution of the µCT scans significant amounts of memory are needed to store all intermediate results and scans, especially, since typical image sizes easily exceed 10 GB.

In order to reduce computation time and to leverage the multi-core architectures found in nearly all modern workstations, the *dask* library and the *dask.array* class (Rocklin, 2015; Dask Development Team, 2016) were used to parallelize all filter operations for image preparation and segmentation. As a consequence, the algorithm can be easily deployed to a computation cluster where necessary.

The interested reader is further referred to the paper of Gouillart et al. (2016) for an introduction to the processing of tomography data with the Python programming language.

3.3.5 Related methods

As noted above, other single fiber segmentation algorithms have been published in recent years. Salaberger et al. (2011; 2015) described two analysis concepts that both yield medial axis representations of the fibers. The first relies on a global binarization using Otsu's method, subsequent binary thinning, and resolution of touching fibers and junctions to obtain a centerline description. In their second approach the Hessian matrix of the original gray value image is used to compute local orientations, and the gray value distribution in planes orthogonal to the fibers' axes are analyzed to detect fiber centers in clusters. These can then be used to improve the analysis steps of the first method. Their algorithm was applied to short glass fiber reinforced polypropylene composites with

fiber mass fractions of $1\,\%$, $5\,\%$, $10\,\%$ and $30\,\%$ and yielded promising results. Limitations of their method were shown to be related to the global segmentation, due to which two neighboring fibers might be merged during thinning. The extension by means of the Hessian improves the overall segmentation quality, but relies on determining local orientations based on second-order derivatives of the gray value image. In contrast, the algorithm proposed in this work does not yield a medial axis representation, but operates directly on the fiber voxel domains. This has the advantage of naturally extending to measures such as the fiber radius, facilitates the proposed detection error estimate and immediately offers the labeled segmented three-dimensional image. The dependency on the global threshold is also reduced by means of the iterative and thereby adaptive methodology.

In the paper of Glöckner et al. (2016) different short glass fiber reinforced polypropylene and polybutylene terephthalate composites with volume fractions between $1\,\%$ and $20\,\%$ were considered. The proposed stochastic model-based algorithm uses randomly selected and evaluated points within fibers and computation of cylinder integrals along the fiber orientation. Validation using artificially generated volume images showed promising results but also inaccuracies in the detected fiber lengths of approximately $10\,\%$. In addition, while the stochastic nature of the proposed method makes it robust against image noise, it increases the computational burden and renders the algorithm non-deterministic. Their method and the one proposed in this paper share their iterative nature and the fact that detected fibers are removed from the image to expedite the following steps. On the other hand, differences exists with regard to slightly curved fibers, which can be considered in our method and may pose pitfalls in connection with cylinder integrals.

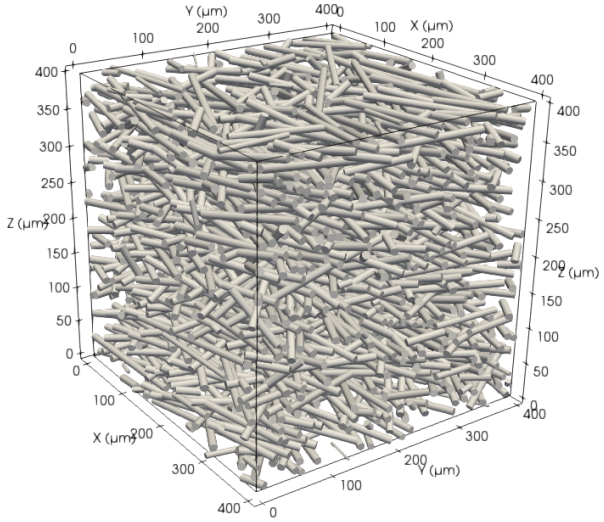

Figure 3.8: Rendering of the microstructure for the artificially generated ground truth data (*GT 1.0*), reconstructed based on the segmentation results. The displayed cylinders were generated using the detected fibers' geometric descriptions.

3.4 Results

3.4.1 Validation using artificial µCT data

Before applying the newly introduced segmentation algorithm to real µCT scans of PA66-GF35, a validation using the artificial scans *GT 1.0* and *GT 0.4* was performed. Due to the idealized nature of the data the image preparation steps were skipped, but the iterative erosion approach with maximum kernel radii k_{max} of 4 (*GT 1.0*) and 6 (*GT 0.4*) proved to be necessary to separate touching fibers.

The segmentation results are summarized in Table 3.2. Of the 1363 fibers in the ground truth data, 1292 fibers were found in the low resolution data while the high resolution data yielded 1289. The small discrepancy

between the segmentation results and the reference is most likely due the fact that some small fiber fragments could not be interpreted as fibers in a meaningful way. By comparing the overall volume of detected fibers with that of the binary image, a detection rate $d = V_{det}/V_{I_b}$ can be computed, which was approximately $96\,\%$ and $99\,\%$ for the two datasets. Different effects can lead to lower detection rates, including fiber fragments with an aspect ratio below 3 that are not considered as fibers and connected fiber that cannot be resolved by the proposed method. Using the detected fibers' geometrical descriptions the fiber morphology can be reconstructed, as visualized in Fig. 3.8.

The obtained second-order fiber orientation tensors are given in Table 3.2 and the maximum relative component-wise error with respect to the reference fiber orientation tensor is $1.9\,\%$ for *GT 1.0* and $1.45\,\%$ for *GT 0.4* (both N_{33}). This is considered to be an acceptable deviation, especially when considering the inherent inaccuracies involved in generating the voxel data. Furthermore, the proposed algorithm delivered more accurate results than VGStudio Max, which underestimated the N_{11} components and overestimated the transverse components of the FOT, yielding a relative error of $60\,\%$ for the N_{33} component.

The fiber lengths and radii were also determined with good accuracy using the proposed method. In order to facilitate a comparison with the reference fiber length data, only fibers that do not touch the domain boundaries and hence are not cut were considered. For the low resolution *GT 1.0* data the fiber length of uncut fibers is $199.8\,\mu\mathrm{m} \pm 3.5\,\mu\mathrm{m}$ and the radius was found to be $4.9\,\mu\mathrm{m} \pm 0.1\,\mu\mathrm{m}$ and therefore very close to the exact values of $200\,\mu\mathrm{m}$ and $5\,\mu\mathrm{m}$ with errors and standard deviation below the inherent voxel length scale of $1\,\mu\mathrm{m}$. The high resolution data yielded very accurate results for the fiber length and radius of $200.0\,\mu\mathrm{m} \pm 0.0\,\mu\mathrm{m}$ and $5.0\,\mu\mathrm{m} \pm 0.0\,\mu\mathrm{m}$, respectively.

3.4.2 Influence of spatial resolution

The influence of a real µCT scan's spatial resolution was studied on PA66-GF35 datasets *ROI 1.0* and *ROI 0.4* introduced above. Both were processed by applying the entire proposed workflow. The raw three-dimensional images were first enhanced using morphological opening with a ball-shaped kernel with a radius equivalent to $2\,\mu\mathrm{m}$ to remove small particles and artifacts. The threshold t for binarization was chosen such that the image volume fraction was close to the reference value of 0.193 and a maximum erosion kernel for the iterative segmentation algorithm was set to $k_{max} = 4$ for *ROI 1.0* and 8 for *ROI 0.4*.

Due to the lower signal-to-noise ratio of the high resolution scan, spurious matrix cavities within fibers were found in the binarized image which were removed using the flood fill method.

The resulting microstructural characteristics are summarized in Table 3.2. A total number of 2108 fibers were detected in the *ROI 1.0* data and similarly 2119 in the higher resolution *ROI 0.4* with detection rates above $90\,\%$. The volume-weighted mean fiber lengths for both scans were also similar at $241.9\,\mu\mathrm{m}$ and $255.7\,\mu\mathrm{m}$: a relative deviation of approximately $5\,\%$. The fiber orientation distribution was compared to data obtained using VGStudio Max, as given in Table 3.2 with a maximum relative deviation in the N_{33} FOT components of $-71.2\,\%$ (*ROI 1.0*) and $-76.8\,\%$ (*ROI 0.4*). Interestingly, the deviation between the low and high resolution scans is lower for the proposed method and more significant for VG when comparing the N_{22} and N_{33} components (cf. Table 3.2).

3.4.3 Full scans of PA66-GF35

The three full height scans were processed using the same workflow and parameters as for the scan *ROI 1.0* above ($k_{max} = 4$) with the binarization threshold t being manually adapted to yield the correct overall fiber

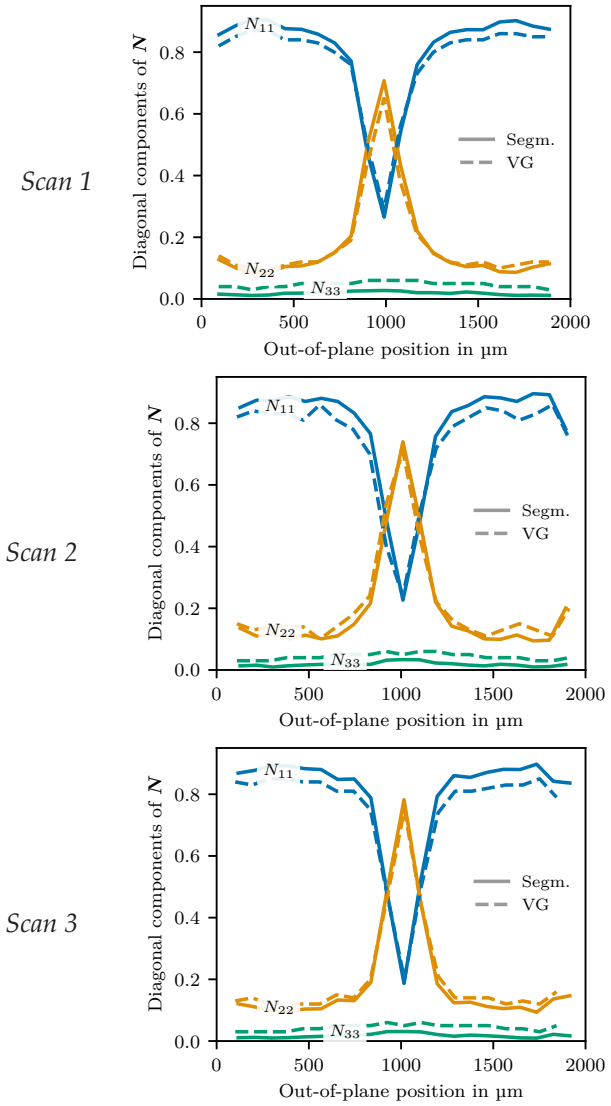

Figure 3.9: Layer-wise second-order fiber orientation tensor $\boldsymbol{N}$ of specimens *Scan 1*, *Scan 2* and *Scan 3*. Results from the proposed method (Segm.) are compared to the respective reference values from VGStudio Max (VG).

volume fraction. As summarized in Table 3.2, detection rates between $85\,\%$ and $88\,\%$ were achieved and between 25,000 to 33,000 fibers were found in the scans.

To visualize the fiber orientation distribution, the second-order fiber orientation tensor was evaluated in 21 layers along the out-of-plane axis (x_3), as shown in Fig. 3.9. The typical layered shell-core morphology is easily visible with fibers in the skin and shell regions being predominantly oriented in the main flow direction x_1 and fibers in the core layer oriented perpendicular to the flow along x_2. Comparing the segmentation results to the curves obtained from VGStudio Max, it can be seen that the latter leads to a systematically lower predicted fiber orientation. The N_{11} components from VG are predicted to be lower whereas the N_{33} components are higher. These deviations are in alignment with the error obtained for scan *GT 1.0* using VG but the final source of deviation remains uncertain.

Due to the single fiber segmentation approach used in this work, the fiber length distribution can also be analyzed immediately. The volume-weighted fiber length distribution for all three scans is shown in Fig. 3.10. A weighted analysis is helpful to alleviate the influence of small fibers, fragments and particles, which would otherwise significantly distort the results. It is noteworthy that the values for the weighted mean fiber length vary only within a small range of $30\,\mu\mathrm{m}$. This become even more apparent in Fig. 3.10 where the weighted length distribution scatter band of all three full scans is shown. It can be seen that the scans lie close to each other and correlate well with the length distribution obtained experimentally.

A similar evaluation was performed for the volume weighted fiber radius distribution shown in Fig. 3.11, which can be approximated well by a Gaussian distribution with mean radius $\bar{r} = 5.1\,\mu\mathrm{m}$ and standard deviation $\sigma_r = 0.53\,\mu\mathrm{m}$. Such values are in good agreement with ex-

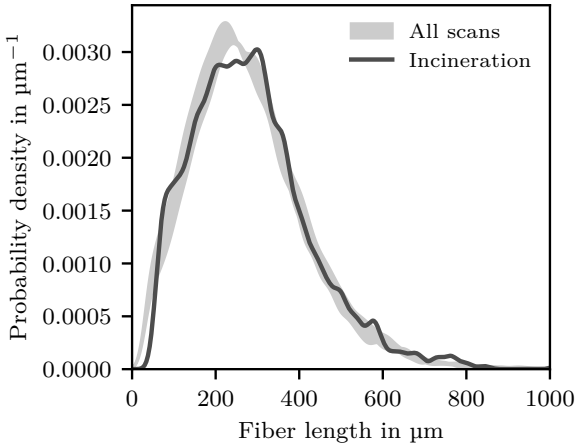

Figure 3.10: Volume-weighted fiber length distribution of all three full PA66-GF35 specimens and comparison with the length distribution from an incinerated specimen.

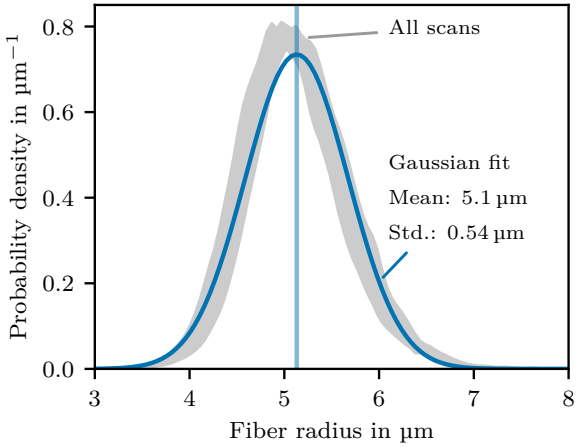

Figure 3.11: Volume-weighted fiber radius distribution of all three full PA66-GF35 specimens and Gaussian fit.

pected fiber radii, which are typically reported to lie between 5 µm to 6 µm (Bernasconi et al., 2008).

In contrast to filter-based algorithms that neglect the fibers' connectivity, the proposed algorithm can also be used to evaluate the correlation of different properties such as orientation and length. This is demonstrated in Fig. 3.12, where the layer-wise FOTs for three length intervals are shown for scan *Scan 1*. It becomes apparent that long fibers tend towards a nearly unidirectional setup, whereas short ones are oriented more randomly. To highlight this effect further, the eigenvalues of the per-layer FOTs can be averaged for each length interval, as shown in Fig. 3.13. With increasing fiber length the orientation state changes from a more random state towards a highly anisotropic and nearly unidirectional form.

Another important morphological parameter that can be evaluated from the µCT scans is the spatially varying fiber volume fraction (Belmonte et al., 2017a). Similar to the fiber orientation distribution, it was evaluated in a layered manner based on the binarized image I_b as shown in Fig. 3.14. For all three scans the volume fraction in the shell layers lies close to the overall nominal average of $19.3\,\%$, whereas a noticeable drop in volume fraction appears in the shell-core transition layer. Within the core region, the fiber fractions exhibits a significant jump of around $40\,\%$ with regard to the mean value (cf.(Rolland et al., 2016)). This is an important insight, as the fiber volume fraction is one of the predominant influence factors in the prediction of the mechanical behavior in such materials.

Concluding, it can be observed that all three scans show similar microstructural characteristics. The fiber orientation, length and radius distributions as well as the fluctuation of fiber volume fraction vary little, even though scan *Scan 1* was taken from a different plate than *Scan 2* and *Scan 3*. This can be explained by good manufacturing reproducibility.

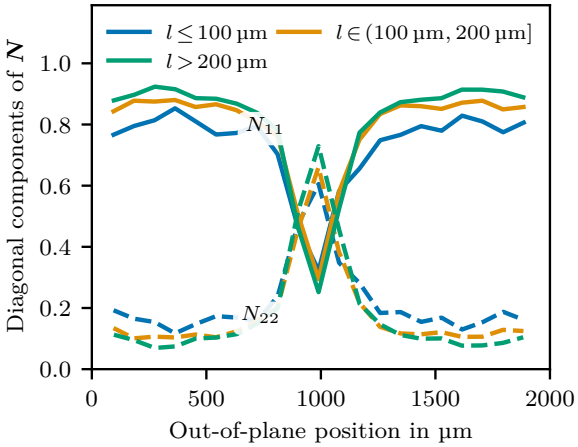

Figure 3.12: The layered fiber orientation state of *Scan 1* evaluated for three length intervals. For clarity only the N_{11} and N_{22} components are shown.

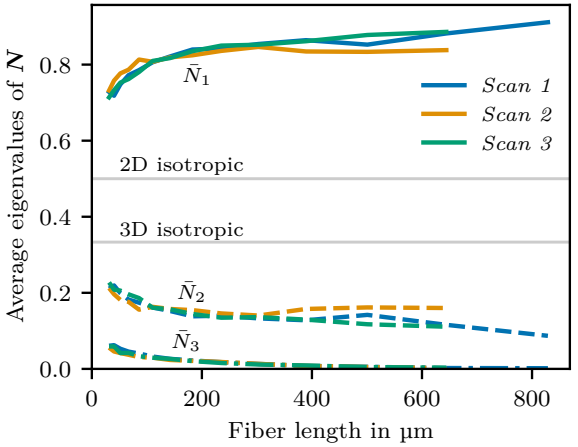

Figure 3.13: Average eigenvalues of the layer-wise FOTs showing the increase of orientation anisotropy for increasing fiber length.

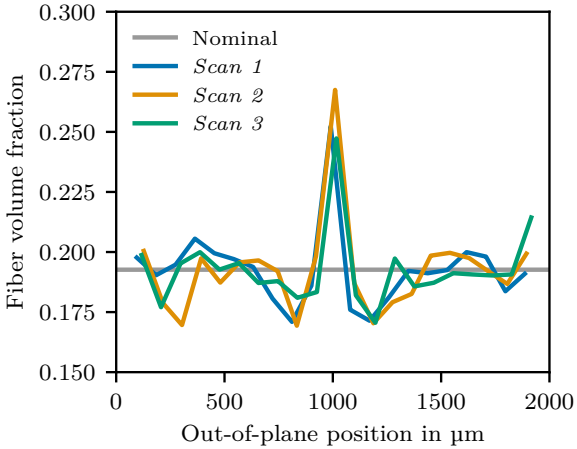

Figure 3.14: Layer-wise fiber volume fraction of all three full PA66-GF35 specimens.

3.4.4 Application to high volume fraction PA66-GF50

In order to assess the algorithm's capabilities regarding high volume fraction SFRT materials, it was applied to the high-resolution PA66-GF50 sub-volume dataset *ROI High*. Apart from the nominal volume fraction of $30.7\,\%$ and threshold value t, all algorithm parameters were kept the same as for the *ROI 0.4* scan above. As before, the obtained microstructure parameters are given in Table 3.2. Compared to the lower volume fraction scans, a lower detection rate of $59\,\%$ was achieved. This can be explained by the fact that the algorithm was developed using the PA66-GF35 composite and no further modifications were performed specifically for the higher volume fraction PA66-GF50.

Nevertheless, the determined FOT is in acceptable agreement with results from VGStudio Max, showing relative deviations of $11.1\,\%$ in the main orientation direction (N_{22}). The larger deviation of $-48.8\,\%$ in the N_{33} component remains in line with previous cases where VG predicted higher orientations in the transverse directions (cf. Section 3.4.1).

Compared to the results for lower volume fractions, the measured fiber length is significantly lower, which was to be expected due to the high number of fiber-fiber interactions and higher stresses during injection molding.

Table 3.2: Summary of results for the ground truth (*GT*), region of interest (*ROI*) and full scans (*Scan*). This includes the components of the second-order fiber orientation tensor $\boldsymbol{N}$, the number of detected fibers and the volume-weighted mean and standard deviation of the length and radius distributions. Results for the fiber orientation tensors obtained using VGStudio Max (VG) are given as reference.

	N_{11}	N_{22}	N_{33}	N_{23}	N_{13}	N_{12}	Detection rate	Fiber count	Fiber length in µm	Fiber radius in µm
GT Ref	0.6600	0.3000	0.0400	0.0000	0.0000	0.0000		1363	200.0 ± 0.0	5.00 ± 0.00
GT 1.0 (VG)	0.6340	0.3020	0.0640	0.0000	0.0000	0.0000				
GT 1.0	0.6708	0.2886	0.0406	0.0014	-0.0049	-0.0081	96.33 %	1292	199.8 ± 3.5	4.92 ± 0.05
GT 0.4	0.6700	0.2898	0.0402	0.0012	-0.0047	-0.0105	99.40 %	1289	200.0 ± 0.0	5.00 ± 0.01
ROI 1.0	0.6571	0.3198	0.0231	0.0019	0.0209	0.0486	90.05 %	2108	241.9 ± 114.4	5.41 ± 0.52
ROI 1.0 (VG)	0.6400	0.2800	0.0800	0.0000	0.0200	0.0200				
ROI 0.4	0.6534	0.3234	0.0232	0.0020	0.0199	0.0497	95.65 %	2119	255.7 ± 119.6	5.87 ± 0.52
ROI 0.4 (VG)	0.6400	0.2600	0.1000	0.0000	0.0200	0.0200				
ROI High	0.0487	0.9001	0.0512	0.0566	0.0019	0.0389	58.63 %	4564	168.5 ± 96.0	5.46 ± 0.66
ROI High (VG)	0.0900	0.8100	0.1000	0.0600	0.0000	0.0400				
Scan 1	0.7927	0.1889	0.0185	0.0014	0.0245	0.0333	88.07 %	32604	289.9 ± 140.8	5.25 ± 0.53
Scan 1 (VG)	0.7757	0.1790	0.0467	0.0024	0.0248	0.0257				
Scan 2	0.7743	0.2069	0.0189	0.0001	-0.0015	0.0081	86.71 %	25269	263.5 ± 131.5	5.01 ± 0.53
Scan 2 (VG)	0.7476	0.2086	0.0433	-0.0010	-0.0086	0.0038				
Scan 3	0.7853	0.1969	0.0177	0.0017	-0.0020	-0.0755	85.51 %	30925	273.7 ± 138.4	5.09 ± 0.53
Scan 3 (VG)	0.7535	0.2030	0.0440	0.0010	-0.0025	-0.0650				

3.5 Summary

The microstructure of a short glass fiber reinforced thermoplastic was analyzed using x-ray micro-computed tomography. A novel single fiber segmentation algorithm was proposed that relies on an iterative segmentation and merging procedure. It was implemented in Python, making use of parallelization techniques for improved performance. Validation tests were performed using artificial ground truth µCT data and the method was shown to yield accurate results. The influence of the scan resolutions was assessed by comparing two sub-volume scans at two resolutions and results were shown to be reproducible. The method was then applied to high resolution µCT scans of three glass fiber reinforced polyamide 6.6 (PA66-GF35) samples.

The fiber orientation tensors, fiber length and radius distributions as well as the fluctuating fiber volume fraction were analyzed and good agreement of the fiber orientation tensors was demonstrated when compared to the commercial software VGStudio Max, even exceeding its accuracy for the artificial data. A comparison of the fiber length distributions with results from incineration also demonstrated the quality of the obtained data. Due to the single fiber segmentation it was possible to quantify the correlation of fiber length and orientation and it was shown that the three scans, although obtained from different locations and from two different plates, yielded similar morphological parameters due to the reproducible manufacturing process. Finally, the algorithm's capabilities regarding high volume fraction composites were studied on a high resolution scan of a polyamide 6.6 with a fiber mass fraction of $50\,\%$.

Highly automated analyses using the proposed method can therefore be used to obtain detailed microstructural data of short glass fiber reinforced thermoplastic composites for material model development, quality control purposes or the validation of process simulation workflows.

Chapter 4

On mean field homogenization schemes for short fiber reinforced composites: Unified formulation, application and benchmark[1]

4.1 Introduction

The microstructure of short fiber reinforced composites (SFRCs) – such as short glass fiber reinforced thermoplastics (SFRTs) – strongly influences the mechanical properties of the material and hence those of any final part. Therefore, multi-scale or homogenization methods are important tools, as they allow microstructural properties (such as fiber orientation distributions) to be accounted for and also provide predictions of the effective mechanical behavior of the material at the macro scale.

This chapter covers the topic of multi-scale modeling of SFRCs with a focus in mean field homogenization techniques. A set of common schemes is introduced and discussed, including the Self-Consistent (Hill, 1965; Budiansky, 1965), Mori-Tanaka (Mori and Tanaka, 1973;

[1] This chapter, including all tables and figures, is based on the publication "On mean field homogenization schemes for short fiber reinforced composites: Unified formulation, application and benchmark" (Hessman et al., 2021), with some minor typographical and formatting changes to improve the readability and coherence within this thesis.

Benveniste, 1987), Ponte Castañeda-Willis (Ponte Castañeda and Willis, 1995), Interaction Direct Derivative (Zheng and Du, 2001) and Two-Step (Pierard et al., 2004) schemes. A unified algebraic formulation is derived, which allows for a more clear and comprehensive comparison of the models. This is especially important, as the differences in previous notations have contributed to a lack of clarity with respect to the models' connections and differences. In order to incorporate microstructural data into these models, different methods are discussed and compared, including the adaptive scheme by Goldberg et al. (2017). Both the predicted elastic properties as well as the predictions of average stresses on the micro scale are evaluated and compared to results from full-field simulations using a Fast Fourier Transform (FFT) based solver.

Within this chapter, the statistical microstructure description obtained from the single fiber segmentation algorithm from Chapter 3 (cf. Hessman et al., 2019) is used as input.

Chapter structure

The chapter is split into four parts. In Section 4.2 the relevant information on the employed material and experiments is given. This includes tensile tests and a summary of the microstructural data obtained in Chapter 3. Section 4.3 gives an overview over the fundamental equations of mean field homogenization, introduces the different schemes and discusses other theoretical aspects. Thereafter, Section 4.4 contains benchmarks of the models and comparisons to reference solutions. A summary of the chapter's results is given in Section 4.5

4.2 Material and microstructure

4.2.1 Short glass fiber reinforced polyamide 6.6

In this work a commercially available short glass fiber reinforced polyamide 6.6 (PA66-GF35) with a fiber mass fraction of $35\,\%$ is used as an example composite material. Given a fiber density of $2.55\,\mathrm{g\,cm^{-3}}$ and a matrix density of $1.13\,\mathrm{g\,cm^{-3}}$, the fiber mass fraction of $35\,\%$ results in a fiber volume fraction of approximately $19.3\,\%$. Details on the isotropic elastic properties of the two phases are given in Table 4.1.

Rectangular plates of the material were produced by injection molding, out of which specimens for x-ray micro-computed tomography (µCT) and mechanical testing were milled (see Fig. 4.1). To analyze the complex microstructure, a µCT single fiber segmentation algorithm was used. For details on the µCT analysis workflow and corresponding results, the reader is referred to the paper Hessman et al. (2019)[2]. An overview of the obtained microstructural information is given in Section 4.2.2.

The anisotropic stiffness of the material was measured by tensile tests performed at the Institute of Engineering Mechanics (Karlsruhe Institute of Technology (KIT), Germany). Tensile specimens (Becker, 2009) were cut out of the plates in angles of $0°$, $15°$, $30°$, $60°$ and $90°$ with respect to the main flow direction (x_1). To remove the influence of moisture absorption, the specimens were dried in a vacuum oven at $80\,°\mathrm{C}$ and below $5\,\mathrm{mbar}$ absolute pressure for $72\,\mathrm{h}$. They were then tested using a *Zwick* tensile testing setup with a *GOM Aramis 3D 4M* optical strain measurement device. Between five and nine specimens were tested per orientation to obtain statistically meaningful data. The resulting Young's moduli are shown in Fig. 4.2 together with the scatter and standard

[2] cf. Chapter 3 of this thesis

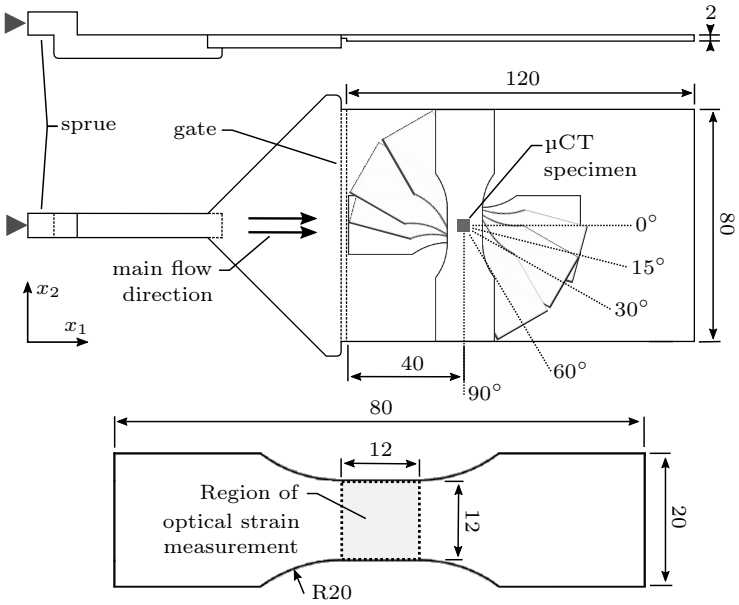

Figure 4.1: Outline of the plate geometry, the location of µCT and tensile specimens in the plate, and a drawing of the tensile specimen with the region of optical strain measurement (all dimensions in mm, based upon Hessman et al. (2019)

deviations. As expected, the material is considerably stiffer along the main flow direction (0°) and more compliant in the off-axis directions.

4.2.2 Microstructural analysis

The material's complex microstructure was resolved by three µCT scans of cuboid specimens that were cut out of the plates at a distance of 40 mm from the gate (see Fig. 4.1). An exemplary rendering of one of the underlying µCT scans is given in Fig. 4.3, highlighting the shell-core orientation distribution.

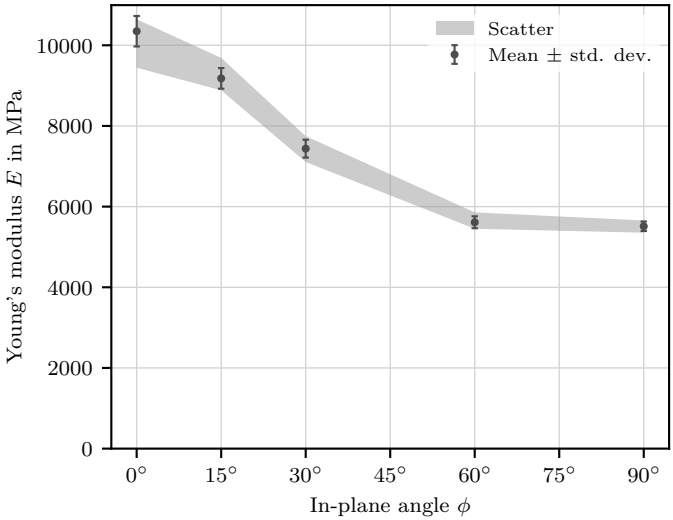

Figure 4.2: Orientation-dependent Young's modulus of the composite specimens, tested at different angles, including the scatter band and standard deviations.

From the µCT scans the fiber morphology was extracted using the single fiber segmentation algorithm published in Hessman et al. (2019)[3]. The data obtained using the algorithm contains tuples of orientation, length, diameter (or radius) and position $f = (\boldsymbol{p}, l, d, \bar{\boldsymbol{x}})$ for each fiber, which accurately describe the material's microstructure. Subsequently, statistical descriptions such as the volume-weighted fiber orientation and length distributions as well as mean quantities were computed. In order to obtain statistically meaningful data, all microstructural descriptors were taken as averages over all three µCT scans, with results given in Table 4.1. The resulting layer-wise second-order fiber orientation tensor is shown in Fig. 4.4, exhibiting the canonical layered shell-core fiber orientation distribution (Bernasconi et al., 2008) and low variance

[3] cf. Chapter 3 of this thesis

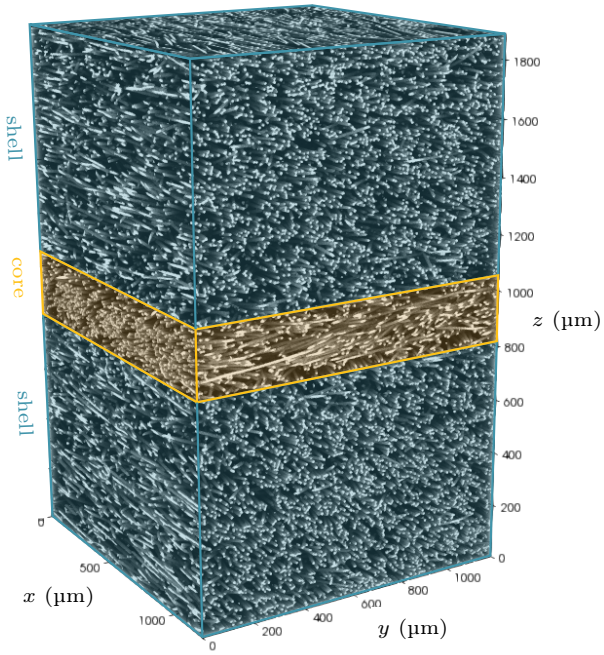

Figure 4.3: Rendering of one of the three µCT scans from Hessman et al. (2019)(cf. Chapter 3 of this thesis) used in this work.

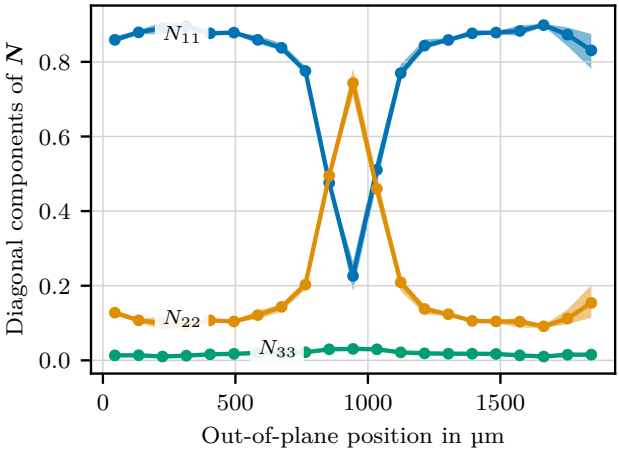

Figure 4.4: Layer-wise second-order fiber orientation distribution derived from the second-order fiber orientation tensor. Both the scatter band and mean values are shown based on the three segmented µCT scans.

between the three underlying µCT scans. The volume-weighted fiber length distribution can be found in Fig. 4.5, also exhibiting a narrow scatter band.

Additional information regarding the obtained microstructural details can be found in Hessman et al. (2019)[4].

[4] cf. Chapter 3 of this thesis

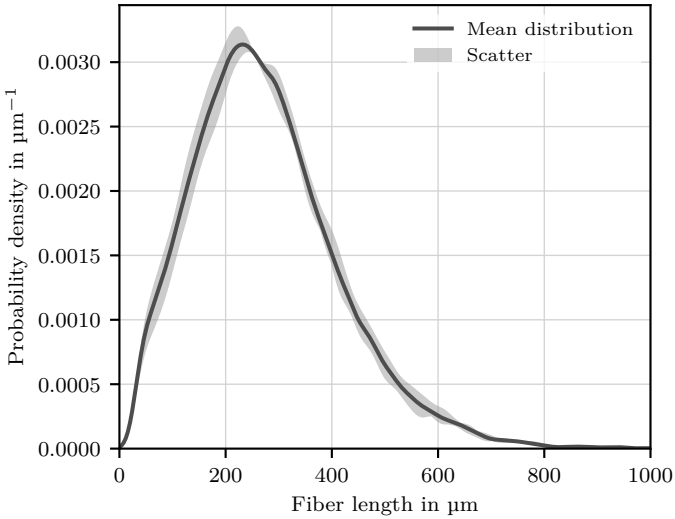

Figure 4.5: The volume-weighted fiber length distribution from the µCT segmentation analysis. The scatter band of the three specimens is shown alongside the mean curve.

Table 4.1: Material and microstructural properties for the PA66-GF35 composite obtained from three µCT scans. A more detailed microstructural description is given in Hessman et al. (2019)(cf. Chapter 3 of this thesis).

Matrix Young's modulus	$E_\mathrm{M} = 3\,\mathrm{GPa}$
Matrix Poisson's ratio	$\nu_\mathrm{M} = 0.4$
Fiber Young's modulus	$E_\mathrm{F} = 72\,\mathrm{GPa}$
Fiber Poisson's ratio	$\nu_\mathrm{F} = 0.22$
Fiber volume fraction	$c_\mathrm{F} = 19.3\,\%$
Mean fiber orientation tensor	$\bar{\boldsymbol{N}} \mathrel{\widehat{=}} \begin{bmatrix} 0.7855 & -0.0096 & 0.0089 \\ -0.0096 & 0.1962 & 0.0012 \\ 0.0089 & 0.0012 & 0.0183 \end{bmatrix}$
Mean fiber diameter	$\bar{d} = 10.2\,\mu\mathrm{m}$
Mean fiber length	$\bar{l} = 275.7\,\mu\mathrm{m}$
Mean fiber aspect ratio	$\bar{a} = 27$

4.3 Mean field homogenization for short fiber reinforced composites

4.3.1 Fundamental relations of mean field homogenization

This section gives a brief and non-comprehensive overview of the fundamental relations in mean field homogenization theory within the domain of linear elasticity. For further detail and derivations, the reader is referred to literature (Mura, 1987; Nemat-Nasser and Hori, 2010, among others). As this work is predominantly concerned with SFRCs, we will use the terms *fiber*, *inclusion* and *inhomogeneity* equivalently. Nevertheless, most equations remain generally applicable to all types of matrix-inclusion-type composites, whether fibrous or not.

Let us first consider a general N-phase composite with piecewise constant phase stiffness and compliance tensors $\mathbb{C}_\alpha$ and $\mathbb{S}_\alpha$ ($\alpha = 0, \dots, N$), respectively. Following Hill (1963), we can relate the phase average strain ($\boldsymbol{\varepsilon}_\alpha$) and stress ($\boldsymbol{\sigma}_\alpha$) tensors to their macroscopic counterparts using the averaging operator $\langle\cdot\rangle$:

$$\bar{\boldsymbol{\varepsilon}} = \langle \boldsymbol{\varepsilon}_\alpha \rangle_\alpha \,, \qquad \bar{\boldsymbol{\sigma}} = \langle \boldsymbol{\sigma}_\alpha \rangle_\alpha \,. \tag{4.1}$$

The averaging can be defined as a sum over all discrete phases of the entire composite domain, weighted with their volume fractions c_α

$$\langle \cdot \rangle_\alpha = \sum_{\alpha=0}^{N} c_\alpha \, (\cdot)_\alpha \quad \text{where} \quad \sum_{\alpha=0}^{N} c_\alpha = 1. \tag{4.2}$$

The average phase strain and stress tensors can be computed using the fourth-order stress and strain localization tensors by a linear mapping

of the macroscopic quantities

$$\boldsymbol{\varepsilon}_\alpha = \mathbb{A}_\alpha \left[\bar{\boldsymbol{\varepsilon}}\right], \qquad \boldsymbol{\sigma}_\alpha = \mathbb{B}_\alpha \left[\bar{\boldsymbol{\sigma}}\right]. \tag{4.3}$$

By inserting the localization tensors from Eq. (4.3) into Eq. (4.1), one obtains the identities

$$\mathbb{I}^{\mathrm{S}} = \langle \mathbb{A}_\alpha \rangle_\alpha, \qquad \mathbb{I}^{\mathrm{S}} = \langle \mathbb{B}_\alpha \rangle_\alpha. \tag{4.4}$$

Equations for the effective stiffness and compliance tensors $\bar{\mathbb{C}}$ and $\bar{\mathbb{S}}$ can be obtained by inserting Hooke's law into Eq. (4.1) for each phase and then including the localization tensors from Eq. (4.3)

$$\bar{\mathbb{C}} = \langle \mathbb{C}_\alpha \mathbb{A}_\alpha \rangle_\alpha, \qquad \bar{\mathbb{S}} = \langle \mathbb{S}_\alpha \mathbb{B}_\alpha \rangle_\alpha. \tag{4.5}$$

For the rest of this work, we will focus on fiber-matrix-type composites with a matrix phase (index M) of volume fraction c_{M} and fibers (domain index F and individual indices $\alpha = 1, \ldots, N$) with individual volume fractions c_α. The overall fiber volume fraction then reads $c_{\mathrm{F}} = \sum_{\alpha=1}^{n} c_\alpha = 1 - c_{\mathrm{M}}$. In such cases it is attractive to rewrite Eq. (4.5) using Eq. (4.4) to only depend on the fiber localization tensors:

$$\bar{\mathbb{C}} = \mathbb{C}_{\mathrm{M}} + c_{\mathrm{F}} \left\langle \Delta\mathbb{C}_\alpha \mathbb{A}_\alpha \right\rangle_{\mathrm{F},\alpha}, \qquad \bar{\mathbb{S}} = \mathbb{S}_{\mathrm{M}} + c_{\mathrm{F}} \left\langle \Delta\mathbb{S}_\alpha \mathbb{B}_\alpha \right\rangle_{\mathrm{F},\alpha}. \tag{4.6}$$

Here, $\Delta\mathbb{C}_\alpha = \mathbb{C}_\alpha - \mathbb{C}_{\mathrm{M}}$ and $\Delta\mathbb{S}_\alpha = \mathbb{S}_\alpha - \mathbb{S}_{\mathrm{M}}$ are used as shorthands and the averaging over the domain of all fibers is defined as

$$\langle \cdot \rangle_{\mathrm{F},\alpha} = \sum_{\alpha=1}^{N} \frac{c_\alpha}{c_{\mathrm{F}}} (\cdot)_\alpha. \tag{4.7}$$

Eq. (4.6) shows that the effective elastic properties of the composite are fully defined by the phase properties and either the strain or stress localization tensors of the fiber phases.

4.3.2 The dilute approximation

The dilute approximation – or *single inclusion problem* – is of high theoretical importance as it gives the strain and stress in an ellipsoidal inclusion, embedded in an infinite matrix material and subjected to a far-field strain $\bar{\varepsilon}$ or stress $\bar{\boldsymbol{\sigma}}$ (Eshelby, 1957). It was shown by Eshelby that, for ellipsoidal inclusions, the strain and hence stress within homogeneous ellipsoidal inclusions is indeed constant. The strain and stress localization tensors in the dilute approximation are (Hill, 1965)

$$\mathbb{A}_\alpha^{\mathrm{dil}} = \left(\mathbb{I}^{\mathrm{S}} + \mathbb{P}_\alpha \Delta\mathbb{C}_\alpha\right)^{-1}, \quad \mathbb{B}_\alpha^{\mathrm{dil}} = \left(\mathbb{I}^{\mathrm{S}} + \mathbb{Q}_\alpha \Delta\mathbb{S}_\alpha\right)^{-1}. \tag{4.8}$$

Here we employ the two major-symmetric fourth-order tensors $\mathbb{P}$ and $\mathbb{Q}$ as introduced by Hill (1965).

Both tensors can be related by the identity (Hill, 1965)

$$\mathbb{P}\mathbb{C}_0 + \mathbb{S}_0\mathbb{Q} = \mathbb{I}^{\mathrm{S}}. \tag{4.9}$$

$\mathbb{P}_\alpha$, also referred to as Hill's polarization tensor, is frequently used in literature and employed in different models, whereas its dual $\mathbb{Q}_\alpha$ is seldom employed (cf. Walpole, 1981). Using Hill's definition of $\mathbb{P}$ and the identity above, we can compute both tensors as a function of Eshelby's tensor $\mathbb{E}_\alpha$ and the matrix material:

$$\mathbb{P}_\alpha = \mathbb{E}_\alpha \mathbb{S}_{\mathrm{M}}, \qquad \mathbb{Q}_\alpha = \mathbb{C}_{\mathrm{M}}(\mathbb{I}^{\mathrm{S}} - \mathbb{E}_\alpha) \tag{4.10}$$

Explicit equations for $\mathbb{E}_\alpha$ are given in literature (e.g. Tandon and Weng, 1984; 1986) for a spheroidal inclusion in an isotopic matrix medium. If the matrix is non-isotropic, numerical solutions are required (Willis, 1981; Gavazzi and Lagoudas, 1990; Müller et al., 2015).

4.3.3 Homogenization schemes

To account for real microstructures with *non*-dilute inclusion volume fractions, different methods have been suggested over many years. Below, a selected set of models are introduced: The Self-Consistent, Two-Step, Mori-Tanaka, Interaction-Direct Derivative, and Ponte Castañeda-Willis homogenization schemes. Special focus is put on recasting the latter three models into a *unified* structure.

Self-Consistent scheme

The Self-Consistent Scheme (SC) (Hill, 1965; Budiansky, 1965) is constructed directly from the dilute approximation by computing the dilute strain concentration tensor (Eq. (4.8)) as a function of the effective composite stiffness, instead of the matrix material. This means that the composite behaves as if every fiber were embedded in the infinite medium with stiffness $\bar{\mathbb{C}}$ (cf. Fig. 4.6), subjected to the far-field strain $\bar{\boldsymbol{\varepsilon}}$

$$\mathbb{A}_\alpha^{\mathrm{SC}} = \mathbb{A}_\alpha^{\mathrm{dil}}(\bar{\mathbb{C}}) = \left(\mathbb{I}^{\mathrm{S}} + \mathbb{P}_\alpha(\bar{\mathbb{C}})(\mathbb{C}_\alpha - \bar{\mathbb{C}})\right)^{-1}. \tag{4.11}$$

By approximating the effective stiffness $\bar{\mathbb{C}}$ in the above equation using the SC method itself, we get an implicit equation which can be solved iteratively:

$$\bar{\mathbb{C}}^{\mathrm{SC}} = \mathbb{C}_{\mathrm{M}} + c_{\mathrm{F}} \left\langle \Delta\mathbb{C}_\alpha \mathbb{A}_\alpha^{\mathrm{dil}}(\bar{\mathbb{C}}^{\mathrm{SC}}) \right\rangle_{\mathrm{F},\alpha}. \tag{4.12}$$

Mori-Tanaka scheme

The Mori-Tanaka scheme (Mori and Tanaka, 1973; Benveniste, 1987) has found widespread application due to its simple formulation and intuitive derivation. Following Benveniste (1987), each fiber in the composite behaves as if it were embedded in the infinite matrix material subjected to the mean matrix strain $\boldsymbol{\varepsilon}_{\mathrm{M}}$ (or stress $\boldsymbol{\sigma}_{\mathrm{M}}$) as far-field boundary condition: $\boldsymbol{\varepsilon}_\alpha = \mathbb{A}_\alpha^{\mathrm{dil}}[\boldsymbol{\varepsilon}_{\mathrm{M}}]$. The strain localization tensor then takes the following

well-known form (Benveniste, 1987; Benveniste et al., 1991):

$$\mathbb{A}_\alpha^{\mathrm{MT}} = \mathbb{A}_\alpha^{\mathrm{dil}} \left(c_{\mathrm{M}} \mathbb{I}^{\mathrm{S}} + c_{\mathrm{F}} \left\langle \mathbb{A}_\beta^{\mathrm{dil}} \right\rangle_{\mathrm{F},\beta} \right)^{-1}. \tag{4.13}$$

By inserting Eq. (4.13) in Eq. (4.6) and exploiting the fact that the term in parentheses in Eq. (4.13) is constant for all fibers α, we get the effective stiffness tensor for the MT scheme

$$\bar{\mathbb{C}}^{\mathrm{MT}} = \mathbb{C}_{\mathrm{M}} + c_{\mathrm{F}} \left\langle \Delta\mathbb{C}_\alpha \mathbb{A}_\alpha^{\mathrm{dil}} \right\rangle_{\mathrm{F},\alpha} \left(c_{\mathrm{M}} \mathbb{I}^{\mathrm{S}} + c_{\mathrm{F}} \left\langle \mathbb{A}_\beta^{\mathrm{dil}} \right\rangle_{\mathrm{F},\beta} \right)^{-1}. \tag{4.14}$$

Let us now rewrite the fiber strain localization tensor from Eq. (4.13) using Eq. (4.8) as follows:

$$\begin{aligned}
\mathbb{A}_\alpha^{\mathrm{MT}} &= \mathbb{A}_\alpha^{\mathrm{dil}} \left((1 - c_{\mathrm{F}}) \mathbb{I}^{\mathrm{S}} + c_{\mathrm{F}} \left\langle \mathbb{A}_\beta^{\mathrm{dil}} \right\rangle_{\mathrm{F},\beta} \right)^{-1} && (4.15)\\
&= \mathbb{A}_\alpha^{\mathrm{dil}} \left(\mathbb{I}^{\mathrm{S}} - c_{\mathrm{F}} \left\langle \mathbb{I}^{\mathrm{S}} - \mathbb{A}_\beta^{\mathrm{dil}} \right\rangle_{\mathrm{F},\beta} \right)^{-1} && (4.16)\\
&= \mathbb{A}_\alpha^{\mathrm{dil}} \left(\mathbb{I}^{\mathrm{S}} - c_{\mathrm{F}} \left\langle \left(\left(\mathbb{A}_\beta^{\mathrm{dil}} \right)^{-1} - \mathbb{I}^{\mathrm{S}} \right) \mathbb{A}_\beta^{\mathrm{dil}} \right\rangle_{\mathrm{F},\beta} \right)^{-1} && (4.17)\\
&= \mathbb{A}_\alpha^{\mathrm{dil}} \left(\mathbb{I}^{\mathrm{S}} - c_{\mathrm{F}} \left\langle \mathbb{P}_\beta \Delta\mathbb{C}_\beta \mathbb{A}_\beta^{\mathrm{dil}} \right\rangle_{\mathrm{F},\beta} \right)^{-1}. && (4.18)
\end{aligned}$$

The formulation in Eq. (4.18) and the corresponding stiffness tensor

$$\bar{\mathbb{C}}^{\mathrm{MT}} = \mathbb{C}_{\mathrm{M}} + c_{\mathrm{F}} \left\langle \Delta\mathbb{C}_\alpha \mathbb{A}_\alpha^{\mathrm{dil}} \right\rangle_{\mathrm{F},\alpha} \left(\mathbb{I}^{\mathrm{S}} - c_{\mathrm{F}} \left\langle \mathbb{P}_\beta \Delta\mathbb{C}_\beta \mathbb{A}_\beta^{\mathrm{dil}} \right\rangle_{\mathrm{F},\beta} \right)^{-1} \tag{4.19}$$

will be referred to as the *unified* formulation for the Mori-Tanaka model. Their importance will be highlighted in the sections below.

Remarkably, due to the strong duality in all formulations, equations for the stress localization ($\mathbb{B}^{\mathrm{MT}}$) and compliance tensors ($\bar{\mathbb{S}}^{\mathrm{MT}}$) can be immediately derived by substituting $\mathbb{S}$ for $\mathbb{C}$, $\mathbb{B}$ for $\mathbb{A}$ and $\mathbb{P}$ for $\mathbb{Q}$, either

in the original or modified versions

$$\mathbb{B}_\alpha^{\mathrm{MT}} = \mathbb{B}_\alpha^{\mathrm{dil}} \left(\mathbb{I}^{\mathrm{S}} - c_{\mathrm{F}} \left\langle \mathbb{Q}_\beta \Delta\mathbb{S}_\beta \mathbb{B}_\beta^{\mathrm{dil}} \right\rangle_{\mathrm{F},\beta} \right)^{-1}, \tag{4.20}$$

$$\bar{\mathbb{S}}^{\mathrm{MT}} = \mathbb{S}_{\mathrm{M}} + c_{\mathrm{F}} \left\langle \Delta\mathbb{S}_\alpha \mathbb{B}_\alpha^{\mathrm{dil}} \right\rangle_{\mathrm{F},\alpha} \left(\mathbb{I}^{\mathrm{S}} - c_{\mathrm{F}} \left\langle \mathbb{Q}_\beta \Delta\mathbb{S}_\beta \mathbb{B}_\beta^{\mathrm{dil}} \right\rangle_{\mathrm{F},\beta} \right)^{-1}. \tag{4.21}$$

Interaction Direct Derivative

The Interaction Direct Derivative (IDD) model of Zheng and Du (Zheng and Du, 2001; Du and Zheng, 2002) is an explicit scheme derived from the three-phase Generalized Self-Consistent Scheme of Christensen and Lo (1979) and has been the subject of many publication, including applications to SFRC materials (Müller et al., 2015; 2016; Buck et al., 2015).

The effective stiffness and compliance tensors for the IDD scheme can be given as follows (Zheng and Du, 2001)

$$\hat{\bar{\mathbb{C}}}^{\mathrm{IDD}} = \mathbb{C}_{\mathrm{M}} + \left(\mathbb{I}^{\mathrm{S}} - c_{\mathrm{F}} \left\langle \Delta\mathbb{C}_\beta \mathbb{A}_\beta^{\mathrm{dil}} \mathbb{P}_\beta^{\mathrm{D}} \right\rangle_{\mathrm{F},\beta} \right)^{-1} \left(c_{\mathrm{F}} \left\langle \Delta\mathbb{C}_\alpha \mathbb{A}_\alpha^{\mathrm{dil}} \right\rangle_{\mathrm{F},\alpha} \right), \tag{4.22}$$

$$\hat{\bar{\mathbb{S}}}^{\mathrm{IDD}} = \mathbb{S}_{\mathrm{M}} + \left(\mathbb{I}^{\mathrm{S}} - c_{\mathrm{F}} \left\langle \Delta\mathbb{S}_\beta \mathbb{B}_\beta^{\mathrm{dil}} \mathbb{Q}_\beta^{\mathrm{D}} \right\rangle_{\mathrm{F},\beta} \right)^{-1} \left(c_{\mathrm{F}} \left\langle \Delta\mathbb{S}_\alpha \mathbb{B}_\alpha^{\mathrm{dil}} \right\rangle_{\mathrm{F},\alpha} \right). \tag{4.23}$$

As these equations cannot be easily compared with those of the MT or SC schemes, we will recast the IDD model by making use of the fact that the stiffness and compliance tensors must be symmetric for the predictions to be physically meaningful. Hence, we can take the major-transpose of the above equations and – due to the symmetry of $\mathbb{C}$, $\mathbb{S}$, $\Delta\mathbb{C}_\beta \mathbb{A}_\beta^{\mathrm{dil}}$ and $\Delta\mathbb{S}_\beta \mathbb{B}_\beta^{\mathrm{dil}}$ – we get

$$\begin{aligned} \bar{\mathbb{C}}^{\mathrm{IDD}} &= \left(\hat{\bar{\mathbb{C}}}^{\mathrm{IDD}} \right)^{\mathrm{T}} \\ &= \mathbb{C}_{\mathrm{M}} + c_{\mathrm{F}} \left\langle \Delta\mathbb{C}_\alpha \mathbb{A}_\alpha^{\mathrm{dil}} \right\rangle_{\mathrm{F},\alpha} \left(\mathbb{I}^{\mathrm{S}} - c_{\mathrm{F}} \left\langle \mathbb{P}_\beta^{\mathrm{D}} \Delta\mathbb{C}_\beta \mathbb{A}_\beta^{\mathrm{dil}} \right\rangle_{\mathrm{F},\beta} \right)^{-1}, \end{aligned} \tag{4.24}$$

$$\begin{aligned}\bar{\mathbb{S}}^{\mathrm{IDD}} &= \left(\hat{\bar{\mathbb{S}}}^{\mathrm{IDD}}\right)^{\mathrm{T}} \\ &= \mathbb{S}_{\mathrm{M}} + c_{\mathrm{F}} \left\langle \Delta\mathbb{S}_{\alpha}\mathbb{B}_{\alpha}^{\mathrm{dil}} \right\rangle_{\mathrm{F},\alpha} \left(\mathbb{I}^{\mathrm{S}} - c_{\mathrm{F}} \left\langle \mathbb{Q}_{\beta}^{\mathrm{D}}\Delta\mathbb{S}_{\beta}\mathbb{B}_{\beta}^{\mathrm{dil}} \right\rangle_{\mathrm{F},\beta}\right)^{-1}.\end{aligned} \tag{4.25}$$

In the above equations, $\mathbb{P}_{\beta}^{\mathrm{D}}$ is the major-symmetric distribution polarization tensor (Hill, 1965; Willis, 1981; Ponte Castañeda and Willis, 1995) and $\mathbb{Q}_{\alpha}^{\mathrm{D}} = \mathbb{C}_{\mathrm{M}}(\mathbb{I}^{\mathrm{S}} - \mathbb{E}_{\alpha}^{\mathrm{D}})$ is a major-symmetric tensor, referred to as the (matrix cell) "eigenstiffness" tensor (Zheng and Du, 2001). Given the definition of $\mathbb{Q}_{\alpha}^{\mathrm{D}}$ and comparing Equations (4.24) and (4.25), it becomes apparent that $\mathbb{Q}_{\alpha}^{\mathrm{D}}$ is the distribution equivalent to the $\mathbb{Q}$ tensor suggested by Hill (1965) and introduced above in Equations (4.8) and (4.9). Also, the eigenstiffness tensor $\mathbb{Q}_{\beta}^{\mathrm{D}}$ and the polarization tensor $\mathbb{P}_{\beta}^{\mathrm{D}}$ have the same role within their respective equations, both accounting for the distribution of phase β. In alignment with the three-phase model, the spatial distribution of fibers – also referred to as the pair distribution or two-point statistics – can be associated with an ellipsoidal matrix cell surrounding each fiber (cf. Fig. 4.6). In this work we limit ourselves to the case of a spheroidal spatial distribution, fully defined by its orientation $\boldsymbol{p}_{\beta}^{\mathrm{D}}$ and aspect ratio a_{β}^{D}. Note that, for the IDD model, the distribution cell may be defined independently of the fibers shape and orientation.

A major advantage of these IDD formulations (Equations (4.24) and (4.25)) is that they allow us to extract the strain and stress localization tensors directly by comparing them with the general forms in Eq. (4.6). We get

$$\mathbb{A}_{\alpha}^{\mathrm{IDD}} = \mathbb{A}_{\alpha}^{\mathrm{dil}} \left(\mathbb{I}^{\mathrm{S}} - c_{\mathrm{F}} \left\langle \mathbb{P}_{\beta}^{\mathrm{D}}\Delta\mathbb{C}_{\beta}\mathbb{A}_{\beta}^{\mathrm{dil}} \right\rangle_{\mathrm{F},\beta}\right)^{-1}, \tag{4.26}$$

$$\mathbb{B}_{\alpha}^{\mathrm{IDD}} = \mathbb{B}_{\alpha}^{\mathrm{dil}} \left(\mathbb{I}^{\mathrm{S}} - c_{\mathrm{F}} \left\langle \mathbb{Q}_{\beta}^{\mathrm{D}}\Delta\mathbb{S}_{\beta}\mathbb{B}_{\beta}^{\mathrm{dil}} \right\rangle_{\mathrm{F},\beta}\right)^{-1}. \tag{4.27}$$

Indeed, the above stress localization (Eq. (4.27)) corresponds to the formulation that are only implicitly given by Zheng and Du (2001, eq. 23) by the "effective stress". Furthermore, the strain localization tensor derived above coincides with that given in Charpin and Ehrlacher (2014). Remarkably, they share the same general structure of those given for the Mori-Tanaka scheme above. Other IDD localization tensors published in literature were found to yield incompatible results, as they contain deviations in the ordering of the contraction $\mathbb{P}_\beta^{\mathrm{D}} \Delta\mathbb{C}_\beta \mathbb{A}_\beta^{\mathrm{dil}}$ in Eq. (4.26) (Bary, 2011; Tognevi et al., 2010) and $\mathbb{Q}_\beta^{\mathrm{D}} \Delta\mathbb{S}_\beta \mathbb{B}_\beta^{\mathrm{dil}}$ in Eq. (4.27) (Stora et al., 2006).

It is important to note again that – formally – the formulations above (Equations (4.24) to (4.27)) yield exactly the major transpose of the effective stiffness and compliance given in Zheng and Du (2001) and that such compact equations for $\mathbb{A}_\alpha^{\mathrm{IDD}}$ and $\mathbb{B}_\alpha^{\mathrm{IDD}}$ cannot be obtained otherwise. This is not an issue in cases where the IDD model is applicable and exhibits major symmetry (cf. Section 4.3.5 below).

Ponte Castañeda-Willis

The micromechanical scheme of Ponte Castañeda and Willis (1995) (PCW) is of great importance as it both constitutes a Hashin-Shtrikman-type bounding scheme based on the variational structure of Willis (1977) as well as a generally applicable method for estimating the effective properties of many complex multiphase composites with any kind of phase anisotropy. Its core property is a constant ellipsoidal spatial distribution for all inclusion phases. As will be highlighted later in this paper, the PCW scheme can be obtained from the IDD scheme by setting the phase distribution polarization and eigenstiffness tensors to a constant value ($\mathbb{P}_\alpha^{\mathrm{D}} = \mathbb{P}^{\mathrm{D}}$, $\mathbb{Q}_\alpha^{\mathrm{D}} = \mathbb{Q}^{\mathrm{D}}$) (Zheng and Du, 2001; Du and Zheng, 2002). This is illustrated in Fig. 4.6. Under this premise, the

stiffness tensor can then be derived from Eq. (4.24) and reads

$$\bar{\mathbb{C}}^{\mathrm{PCW}} = \mathbb{C}_{\mathrm{M}} + c_{\mathrm{F}} \left\langle \Delta\mathbb{C}_\alpha \mathbb{A}_\alpha^{\mathrm{dil}} \right\rangle_{\mathrm{F},\alpha} \left(\mathbb{I}^{\mathrm{S}} - c_{\mathrm{F}} \mathbb{P}^{\mathrm{D}} \left\langle \Delta\mathbb{C}_\beta \mathbb{A}_\beta^{\mathrm{dil}} \right\rangle_{\mathrm{F},\beta} \right)^{-1}. \quad (4.28)$$

Although this equation does not coincide with that of the original work by Ponte Castañeda and Willis (1995), simple algebraic transformations are sufficient to reveal that they are indeed equivalent (cf. Aboutajeddine and Neale, 2005). The strain localization tensors can then be given as

$$\mathbb{A}_\alpha^{\mathrm{PCW}} = \mathbb{A}_\alpha^{\mathrm{dil}} \left(\mathbb{I}^{\mathrm{S}} - c_{\mathrm{F}} \mathbb{P}^{\mathrm{D}} \left\langle \Delta\mathbb{C}_\beta \mathbb{A}_\beta^{\mathrm{dil}} \right\rangle_{\mathrm{F},\beta} \right)^{-1}. \quad (4.29)$$

The effective compliance tensor and the stress localization tensor of the PCW scheme can be easily obtained by the same substitutions, previously described for the MT scheme in Section 4.3.3, or by replacing $\mathbb{Q}_\alpha^{\mathrm{D}}$ by $\mathbb{Q}^{\mathrm{D}}$ in Equations (4.25) and (4.27):

$$\mathbb{B}_\alpha^{\mathrm{PCW}} = \mathbb{B}_\alpha^{\mathrm{dil}} \left(\mathbb{I}^{\mathrm{S}} - c_{\mathrm{F}} \mathbb{Q}^{\mathrm{D}} \left\langle \Delta\mathbb{S}_\beta \mathbb{B}_\beta^{\mathrm{dil}} \right\rangle_{\mathrm{F},\beta} \right)^{-1}, \quad (4.30)$$

$$\bar{\mathbb{S}}^{\mathrm{PCW}} = \mathbb{S}_{\mathrm{M}} + c_{\mathrm{F}} \left\langle \Delta\mathbb{S}_\alpha \mathbb{B}_\alpha^{\mathrm{dil}} \right\rangle_{\mathrm{F},\alpha} \left(\mathbb{I}^{\mathrm{S}} - c_{\mathrm{F}} \mathbb{Q}^{\mathrm{D}} \left\langle \Delta\mathbb{S}_\beta \mathbb{B}_\beta^{\mathrm{dil}} \right\rangle_{\mathrm{F},\beta} \right)^{-1}. \quad (4.31)$$

Two-Step scheme

The Two-Step homogenization scheme in the form used in this work was formulated by Pierard et al. (2004) to circumvent some of the issues that may arise for complex multiphase composites when applying models such as the Mori-Tanaka scheme. Its underlying principle can be seen as a decomposition of the microstructure into domains – also referred to as the unidirectional (UD) *pseudo-grains* – of constant inclusion phase properties, orientation and aspect ratio, with each domain containing the inclusion phase at a volume fraction of $1 - c_{\mathrm{M}}$. In the first step, the effective properties of each domain are computed using any suitable homogenization scheme. Then, the overall effective properties are com-

puted by assembling the (generally anisotropic) domains and applying another appropriate homogenization model.

Previous publications have used different combinations of schemes for the first and second step. Nevertheless, the Mori-Tanaka scheme remains the most prevalent for computing the domain properties in the first step. The domain stiffness and strain (equivalently stress) localization tensors belonging to fiber type α are then computed as (cf. Eq. (4.14))

$$\bar{\mathbb{C}}_\alpha^{\mathrm{UD}} = \mathbb{C}_\mathrm{M} + c_\mathrm{F}\Delta\mathbb{C}_\alpha\mathbb{A}_\alpha^{\mathrm{dil}}\Big(\mathbb{I}^\mathrm{S} - c_\mathrm{F}\mathbb{P}_\alpha\Delta\mathbb{C}_\alpha\mathbb{A}_\alpha^{\mathrm{dil}}\Big)^{-1}, \tag{4.32}$$

$$\mathbb{A}_\alpha^{\mathrm{UD}} = \mathbb{A}_\alpha^{\mathrm{dil}}\Big(\mathbb{I}^\mathrm{S} - c_\mathrm{F}\mathbb{P}_\alpha\Delta\mathbb{C}_\alpha\mathbb{A}_\alpha^{\mathrm{dil}}\Big)^{-1}. \tag{4.33}$$

For the second step, some authors have suggested using the implicit Self-Consistent scheme (Kammoun et al., 2015). In this work, as in most, Voigt's weighted arithmetic mean is employed to compute the overall effective stiffness as a function of the domain stiffness tensors $\bar{\mathbb{C}}_\alpha^{\mathrm{UD}}$ and weights $c_{\omega_\alpha} = c_\alpha / c_\mathrm{F}$ with $\sum_{\alpha=1}^{n} c_{\omega_\alpha} = 1$

$$\bar{\mathbb{C}}^{\mathrm{TS}} = \big\langle \bar{\mathbb{C}}_\alpha^{\mathrm{UD}} \big\rangle_{\mathrm{F},\alpha} = \mathbb{C}_\mathrm{M} + c_\mathrm{F}\left\langle \Delta\mathbb{C}_\alpha\mathbb{A}_\alpha^{\mathrm{dil}}\left(\mathbb{I}^\mathrm{S} - c_\mathrm{F}\mathbb{P}_\alpha\Delta\mathbb{C}_\alpha\mathbb{A}_\alpha^{\mathrm{dil}}\right)^{-1}\right\rangle_{\mathrm{F},\alpha}. \tag{4.34}$$

The overall fiber strain and stress localization tensors can be easily computed as the composition of the first and second-step localization tensors. In the present MT/Voigt case and with $\mathbb{A}_\alpha^{\mathrm{Voigt}} = \mathbb{I}^\mathrm{S}$ and $\mathbb{B}_\alpha^{\mathrm{Voigt}} = \bar{\mathbb{C}}_\alpha^{\mathrm{UD}}\bar{\mathbb{S}}$ this reads

$$\mathbb{A}_\alpha^{\mathrm{TS}} = \mathbb{A}_\alpha^{\mathrm{UD}}\mathbb{A}_\alpha^{\mathrm{Voigt}} = \mathbb{A}_\alpha^{\mathrm{dil}}\left(\mathbb{I}^\mathrm{S} - c_\mathrm{F}\mathbb{P}_\alpha\Delta\mathbb{C}_\alpha\mathbb{A}_\alpha^{\mathrm{dil}}\right)^{-1}, \tag{4.35}$$

$$\mathbb{B}_\alpha^{\mathrm{TS}} = \mathbb{B}_\alpha^{\mathrm{UD}}\mathbb{B}_\alpha^{\mathrm{Voigt}} = \mathbb{B}_\alpha^{\mathrm{dil}}\left(\mathbb{I}^\mathrm{S} - c_\mathrm{F}\mathbb{Q}_\alpha\Delta\mathbb{S}_\alpha\mathbb{B}_\alpha^{\mathrm{dil}}\right)^{-1}\mathbb{B}_\alpha^{\mathrm{Voigt}}. \tag{4.36}$$

4.3.4 Connections between models

A series of connections exist between the above-mentioned models. While these have been mentioned in literature, the goal of this section is to give a comprehensive and clear summary. Due to the consistent formulations given in Section 4.3.3, we can summarize all model equations compactly, as shown in Table 4.2. This overview shows that the IDD, MT and PCW schemes only differ due to the properties and role of the $\mathbb{P}$ and $\mathbb{Q}$ tensors (cf. Fig. 4.6). Furthermore, the TS (MT/Voigt) scheme inherits the MT scheme's structure, except for the missing averaging within the strain and stress localization tensors.

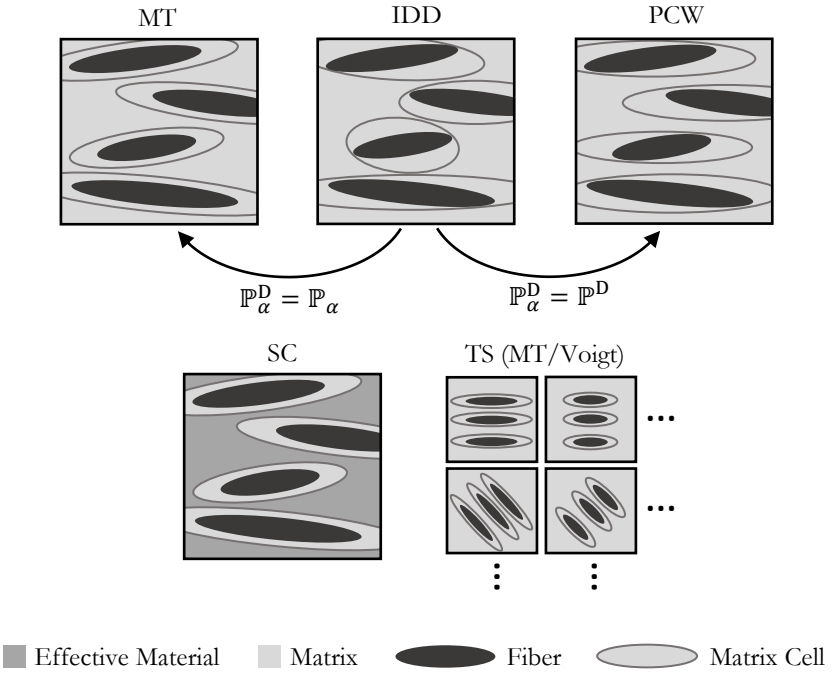

Figure 4.6: Schematics of the different mean field models. Furthermore, the relationship between the spheroidal fibers and their spatial distribution (matrix cell) for the MT, IDD and PCW models is highlighted.

Table 4.2: Summary of the SC, MT, IDD, PCW and TS mean field homogenization schemes. The fiber strain and stress localization tensors are given, either of which fully define the different models.

	Strain localization tensor $\mathbb{A}_\alpha$	Stress localization tensor $\mathbb{B}_\alpha$
SC	$\mathbb{A}_\alpha^{\mathrm{dil}}(\bar{\mathbb{C}})$ (implicit problem)	$\mathbb{B}_\alpha^{\mathrm{dil}}(\bar{\mathbb{C}})$ (implicit problem)
MT	$\mathbb{A}_\alpha^{\mathrm{dil}}\left(\mathbb{I}^{\mathrm{S}} - c_{\mathrm{F}}\left\langle \mathbb{P}_\beta \Delta\mathbb{C}_\beta \mathbb{A}_\beta^{\mathrm{dil}}\right\rangle_{\mathrm{F},\beta}\right)^{-1}$	$\mathbb{B}_\alpha^{\mathrm{dil}}\left(\mathbb{I}^{\mathrm{S}} - c_{\mathrm{F}}\left\langle \mathbb{Q}_\beta \Delta\mathbb{S}_\beta \mathbb{B}_\beta^{\mathrm{dil}}\right\rangle_{\mathrm{F},\beta}\right)^{-1}$
IDD	$\mathbb{A}_\alpha^{\mathrm{dil}}\left(\mathbb{I}^{\mathrm{S}} - c_{\mathrm{F}}\left\langle \mathbb{P}_\beta^{\mathrm{D}} \Delta\mathbb{C}_\beta \mathbb{A}_\beta^{\mathrm{dil}}\right\rangle_{\mathrm{F},\beta}\right)^{-1}$	$\mathbb{B}_\alpha^{\mathrm{dil}}\left(\mathbb{I}^{\mathrm{S}} - c_{\mathrm{F}}\left\langle \mathbb{Q}_\beta^{\mathrm{D}} \Delta\mathbb{S}_\beta \mathbb{B}_\beta^{\mathrm{dil}}\right\rangle_{\mathrm{F},\beta}\right)^{-1}$
PCW	$\mathbb{A}_\alpha^{\mathrm{dil}}\left(\mathbb{I}^{\mathrm{S}} - c_{\mathrm{F}}\mathbb{P}^{\mathrm{D}}\left\langle \Delta\mathbb{C}_\beta \mathbb{A}_\beta^{\mathrm{dil}}\right\rangle_{\mathrm{F},\beta}\right)^{-1}$	$\mathbb{B}_\alpha^{\mathrm{dil}}\left(\mathbb{I}^{\mathrm{S}} - c_{\mathrm{F}}\mathbb{Q}^{\mathrm{D}}\left\langle \Delta\mathbb{S}_\beta \mathbb{B}_\beta^{\mathrm{dil}}\right\rangle_{\mathrm{F},\beta}\right)^{-1}$
TS (MT/Voigt)	$\mathbb{A}_\alpha^{\mathrm{dil}}\left(\mathbb{I}^{\mathrm{S}} - c_{\mathrm{F}}\mathbb{P}_\alpha \Delta\mathbb{C}_\alpha \mathbb{A}_\alpha^{\mathrm{dil}}\right)^{-1}$	$\mathbb{B}_\alpha^{\mathrm{dil}}\left(\mathbb{I}^{\mathrm{S}} - c_{\mathrm{F}}\mathbb{Q}_\alpha \Delta\mathbb{S}_\alpha \mathbb{B}_\alpha^{\mathrm{dil}}\right)^{-1} \mathbb{B}_\alpha^{\mathrm{Voigt}}$

The MT scheme can be obtained as a special case of the IDD formalism when the fibers and their associated spatial distribution share the same ellipsoidal shape (Hu and Weng, 2000b; Zheng and Du, 2001). Restricting ourselves to spheroids, this translates into the fibers and the distributions spheroids sharing the same orientation and aspect ratio ($\boldsymbol{p}_\alpha = \boldsymbol{p}_\alpha^{\mathrm{D}}$ and $a_\alpha = a_\alpha^{\mathrm{D}}$). Hence, we get $\mathbb{P}_\alpha = \mathbb{P}_\alpha^{\mathrm{D}}$ such that Equations (4.19) and (4.24) coincide. The PCW estimate of any suitable microstructure can be constructed from the IDD scheme by setting the spatial distribution to be the same for all fibers and hence $\mathbb{P}_\alpha^{\mathrm{D}} = \mathbb{P}^{\mathrm{D}}$ (Zheng and Du, 2001). As noted by Ponte Castañeda and Willis (1995), Hu and Weng (2000b) and Zheng and Du (2001), the MT, PCW and IDD estimates coincide in the case where all fibers and the spatial distribution spheroids are aligned and have the same shape ($\mathbb{P}_\alpha = \mathbb{P} = \mathbb{P}^{\mathrm{D}}$). This is again due to the fact that the MT estimate implies that each inclusion's spatial distribution is of the same shape and orientation as the inclusion itself ($\mathbb{P}_\alpha = \mathbb{P}_\alpha^{\mathrm{D}}$) (Hu and Weng, 2000b).

Concluding, we can regard the IDD model as a generalized formulation, capable of producing the MT, PCW and related schemes by corresponding choices for the spatial distribution of the fibers (and hence the $\mathbb{P}^{\mathrm{D}}$ and $\mathbb{Q}^{\mathrm{D}}$ tensors). In its most general form, it introduces additional morphological parameters for the spatial distribution, which need to be chosen or derived from microstructural analyses.

It is worth noting that additional connections can be made between the three models and the Double Inclusion (DI) type models, originally suggested by Hori and Nemat-Nasser (1993), as published e.g. in Hu and Weng (2000a) and Aboutajeddine and Neale (2005).

The TS scheme in the present MT/Voigt variant displays a slightly different structure than the aforementioned three models. Due to the sequential nature of the model, the strain localization tensor lacks the coupling to the other phases through the averaging present in the other models. Only for a homogeneous fiber phase and aligned and equally

shaped fibers do the TS and MT schemes coincide. Interestingly, the specific MT/Voigt variant of the Two-Step framework is fully equivalent to a special case of the "equivalent poly-inclusion" approach suggested by Ferrari (1994) and to the modification of the Mori-Tanaka scheme proposed by Schjødt-Thomsen and Pyrz (2001).

4.3.5 Issue of major symmetry

The possible loss of major symmetry in the Mori-Tanaka scheme has been the subject of many publications (Benveniste et al., 1991; Ferrari, 1991; Schjødt-Thomsen and Pyrz, 2001; Brylka, 2017). In this section we will revisit the issue in a broader scope by employing the *unified* formulations introduced above. While we will restrict ourselves to using the stiffness tensor equations, the same statements can be made by studying the compliance tensors.

To continue, we can first note that the contraction of the phase stiffness increment and dilute strain localization tensor $\Delta\mathbb{C}_\alpha\mathbb{A}_\alpha^{\mathrm{dil}}$ is always major-symmetric (Walpole, 1981). Coincidentally, this alone proves the major symmetry of the SC scheme (Eq. (4.12)). We can now rearrange Eq. (4.24) of the IDD model as follows:

$$\bar{\mathbb{C}}^{\mathrm{IDD}} = \mathbb{C}_{\mathrm{M}} + c_{\mathrm{F}} \left\langle \Delta\mathbb{C}_\alpha\mathbb{A}_\alpha^{\mathrm{dil}} \right\rangle_{\mathrm{F},\alpha} \left(\mathbb{I}^{\mathrm{S}} - c_{\mathrm{F}} \left\langle \mathbb{P}_\alpha^{\mathrm{D}} \Delta\mathbb{C}_\alpha\mathbb{A}_\alpha^{\mathrm{dil}} \right\rangle_{\mathrm{F},\alpha} \right)^{-1} \tag{4.37}$$

$$= \mathbb{C}_{\mathrm{M}} + c_{\mathrm{F}} \Big(\left\langle \Delta\mathbb{C}_\alpha\mathbb{A}_\alpha^{\mathrm{dil}} \right\rangle_{\mathrm{F},\alpha}^{-1} - c_{\mathrm{F}} \left\langle \mathbb{P}_\alpha^{\mathrm{D}} \Delta\mathbb{C}_\alpha\mathbb{A}_\alpha^{\mathrm{dil}} \right\rangle_{\mathrm{F},\alpha} \left\langle \Delta\mathbb{C}_\alpha\mathbb{A}_\alpha^{\mathrm{dil}} \right\rangle_{\mathrm{F},\alpha}^{-1} \Big)^{-1} \tag{4.38}$$

This structure allows us to state that the IDD model has major symmetry when the contraction $\left\langle \mathbb{P}_\alpha^{\mathrm{D}} \Delta\mathbb{C}_\alpha\mathbb{A}_\alpha^{\mathrm{dil}} \right\rangle_{\mathrm{F},\alpha} \left\langle \Delta\mathbb{C}_\alpha\mathbb{A}_\alpha^{\mathrm{dil}} \right\rangle_{\mathrm{F},\alpha}^{-1}$ is symmetric, as both $\mathbb{C}_{\mathrm{M}}$ and $\Delta\mathbb{C}_\alpha\mathbb{A}_\alpha^{\mathrm{dil}}$ are always symmetric.

Looking next at the special case of the Mori-Tanaka scheme, we set $\mathbb{P}_\alpha^{\mathrm{D}} = \mathbb{P}_\alpha$, keeping in mind that $\mathbb{P}_\alpha$ only depends on the matrix stiffness tensor and geometry of the fiber.

If all fibers are perfectly aligned (UD) and have the same shape (or even possess spherical shape), hence $\boldsymbol{p}_\alpha = \boldsymbol{p},\ a_\alpha = a$, we get $\mathbb{P}_\alpha = \mathbb{P}$. This means that $\mathbb{P}$ can be taken out of the averaging, allowing for the transformation

$$\left\langle \mathbb{P}\Delta\mathbb{C}_\alpha\mathbb{A}_\alpha^{\mathrm{dil}}\right\rangle_{\mathrm{F},\alpha}\left\langle \Delta\mathbb{C}_\alpha\mathbb{A}_\alpha^{\mathrm{dil}}\right\rangle_{\mathrm{F},\alpha}^{-1} = \mathbb{P}\left\langle \Delta\mathbb{C}_\alpha\mathbb{A}_\alpha^{\mathrm{dil}}\right\rangle_{\mathrm{F},\alpha}\left\langle \Delta\mathbb{C}_\alpha\mathbb{A}_\alpha^{\mathrm{dil}}\right\rangle_{\mathrm{F},\alpha}^{-1} = \mathbb{P}, \tag{4.39}$$

which proves major symmetry in this case due to the symmetry of $\mathbb{P}$ itself. It should be noted that this even holds for a non-homogeneous fiber phase and any anisotropy of the matrix or fibers.

The MT scheme is known to yield symmetric results for composites with complex microstructures (e.g. with orientation or length distributions) as long as the fibers are *homogeneous* with the same (possibly) anisotropic stiffness tensor in the global reference frame (Benveniste et al., 1991). The most probable composite of this kind is arguably one with complex microstructure and homogeneous *isotropic* fibers (Ferrari, 1991; Brylka, 2017). Since the fiber stiffness tensor is constant for all fibers, we can take it out of the averaging

$$\left\langle \Delta\mathbb{C}_\alpha\mathbb{A}_\alpha^{\mathrm{dil}}\right\rangle_{\mathrm{F},\alpha}^{-1} = \left\langle \mathbb{A}_\alpha^{\mathrm{dil}}\right\rangle_{\mathrm{F},\alpha}^{-1}\left(\Delta\mathbb{C}_\alpha\right)^{-1}. \tag{4.40}$$

Due to this fact and following the logic of Equations (4.16), (4.17) and (4.18) in reverse order we can write

$$\begin{aligned}
&\left\langle \mathbb{P}\Delta\mathbb{C}_\alpha\mathbb{A}_\alpha^{\mathrm{dil}}\right\rangle_{\mathrm{F},\alpha}\left\langle \Delta\mathbb{C}_\alpha\mathbb{A}_\alpha^{\mathrm{dil}}\right\rangle_{\mathrm{F},\alpha}^{-1}\\
&= \left\langle \left(\left(\mathbb{A}_{\mathrm{F},\alpha}^{\mathrm{dil}}\right)^{-1} - \mathbb{I}^{\mathrm{S}}\right)\mathbb{A}_\alpha^{\mathrm{dil}}\right\rangle_{\mathrm{F},\alpha}\left\langle \Delta\mathbb{C}_\alpha\mathbb{A}_\alpha^{\mathrm{dil}}\right\rangle_{\mathrm{F},\alpha}^{-1}\\
&= \left\langle \mathbb{I}^{\mathrm{S}} - \mathbb{A}_\alpha^{\mathrm{dil}}\right\rangle_{\mathrm{F},\alpha}\left\langle \Delta\mathbb{C}_\alpha\mathbb{A}_\alpha^{\mathrm{dil}}\right\rangle_{\mathrm{F},\alpha}^{-1}\\
&= \left(\mathbb{I}^{\mathrm{S}} - \left\langle \mathbb{A}_\alpha^{\mathrm{dil}}\right\rangle_{\mathrm{F},\alpha}\right)\left\langle \mathbb{A}_\alpha^{\mathrm{dil}}\right\rangle_{\mathrm{F},\alpha}^{-1}\left(\Delta\mathbb{C}_\alpha\right)^{-1}\\
&= \left\langle \Delta\mathbb{C}_\alpha\mathbb{A}_\alpha^{\mathrm{dil}}\right\rangle_{\mathrm{F},\alpha}^{-1} - \left(\Delta\mathbb{C}_\alpha\right)^{-1}.
\end{aligned} \tag{4.41}$$

As both terms in the last line are symmetric, this shows the overall symmetry of the MT scheme for homogeneous fibers and complex microstructures.

The fact that the PCW scheme is always major-symmetric can be proven easily by using the same formalism. Reminding ourselves that the PCW scheme can be derived from the IDD scheme by setting $\mathbb{P}^{\mathrm{D}}_{\alpha} = \mathbb{P}^{\mathrm{D}}$ we can again exclude $\mathbb{P}^{\mathrm{D}}$ from the averaging

$$\left\langle \mathbb{P}^{\mathrm{D}} \Delta\mathbb{C}_{\alpha} \mathbb{A}^{\mathrm{dil}}_{\alpha} \right\rangle_{\mathrm{F},\alpha} \left\langle \Delta\mathbb{C}_{\alpha} \mathbb{A}^{\mathrm{dil}}_{\alpha} \right\rangle^{-1}_{\mathrm{F},\alpha} = \mathbb{P}^{\mathrm{D}} \left\langle \Delta\mathbb{C}_{\alpha} \mathbb{A}^{\mathrm{dil}}_{\alpha} \right\rangle_{\mathrm{F},\alpha} \left\langle \Delta\mathbb{C}_{\alpha} \mathbb{A}^{\mathrm{dil}}_{\alpha} \right\rangle^{-1}_{\mathrm{F},\alpha} = \mathbb{P}^{\mathrm{D}}. \tag{4.42}$$

This is sufficient to prove that the PCW scheme yields symmetric stiffness tensors for any type of complex and inhomogeneous composite as long as it is compatible with the notion of a constant spatial distribution of fibers.

The symmetry of the TS (MT/Voigt) scheme can be easily shown, as each UD domain consists of fibers of constant orientation and shape, for which the Mori-Tanaka effective stiffness tensor is always symmetric. The Voigt arithmetic average of the domain stiffness tensors is also symmetric, yielding an effective composite stiffness tensor whose symmetry is ensured for any type of microstructure (Pierard et al., 2004).

4.3.6 Multilayer formulation

As mentioned above, SFRCs can exhibit a quasi-layered microstructure – resembling laminates – due to the flow conditions during injection molding. In such cases it might be necessary or advantageous to separately model each layer including its specific microstructure, before assembling the overall properties. The simplest approach is the Voigt scheme where the overall stiffness is computed as the arithmetic mean of all layer stiffness tensors. Accordingly, it would be assumed that each layer (index γ) sees the same strain, equal to the macroscopic strain: $\bar{\boldsymbol{\varepsilon}}^{\mathrm{L}}_{\gamma} = \bar{\boldsymbol{\varepsilon}}$. The shortcomings of such an assumption become apparent

in the case of uniaxial loading, since the lateral contraction would be constant, independently of the layers' individual properties.

In this paper the more sophisticated approach of Glüge and Kalisch (2014) is used, who derive the laminate behavior based on the jump conditions between layer pairs. As a result we obtain the laminate stiffness tensor and layer strain and stress localization tensors $\mathbb{A}_\gamma^{\mathrm{L}}$ and $\mathbb{B}_\gamma^{\mathrm{L}}$ that relate the layer strain and stress tensor to their macroscopic counterparts: $\bar{\boldsymbol{\varepsilon}}_\gamma^{\mathrm{L}} = \mathbb{A}_\gamma^{\mathrm{L}}[\bar{\boldsymbol{\varepsilon}}]$ and $\bar{\boldsymbol{\sigma}}_\gamma^{\mathrm{L}} = \mathbb{B}_\gamma^{\mathrm{L}}[\bar{\boldsymbol{\sigma}}]$. To compute the strain or stress of fiber α within layer γ, the fiber and layer concentration tensors are simply composed

$$\boldsymbol{\varepsilon}_\alpha = \mathbb{A}_\alpha \mathbb{A}_\gamma^{\mathrm{L}}[\bar{\boldsymbol{\varepsilon}}], \qquad \boldsymbol{\sigma}_\alpha = \mathbb{B}_\alpha \mathbb{B}_\gamma^{\mathrm{L}}[\bar{\boldsymbol{\sigma}}]. \tag{4.43}$$

For more details on the models and the respective equations, the reader is referred to the original publication by Glüge and Kalisch.

4.3.7 Bounding scheme

Within the TS framework, Müller et al. (2015; 2016) formulate a bounding scheme for the effective properties of composites with complex microstructures. First, the lower and upper bounds ($\bar{\mathbb{C}}_\alpha^{\mathrm{UD}\pm}$) of each UD domain are computed using the Hashin-Shtrikman-type scheme of Willis (1977). Then, the overall lower and upper Two-Step/Hashin-Shtrikman bounds (TS/HS) for the composite are computed based on the the lower and upper domain bounds computed above (Willis, 1977; Ponte Castañeda and Suquet, 1997)

$$\mathbb{C}_\alpha^{\mathrm{TS/HS}\pm} = \left\langle \mathbb{C}_\alpha^{\mathrm{UD}\pm} \mathbb{M}_\alpha^{\pm} \left\langle \mathbb{M}^{\pm} \right\rangle^{-1} \right\rangle_{\mathrm{F},\alpha}, \tag{4.44}$$

$$\mathbb{M}_\alpha^{\pm} = \left(\mathbb{I}^{\mathrm{S}} + \mathbb{P}_0^{\pm} (\mathbb{C}_\alpha^{\mathrm{UD}\pm} - \mathbb{C}_0^{\pm}) \right)^{-1}. \tag{4.45}$$

Here, $\mathbb{P}_0^{\pm}$ accounts for the ellipsoidal shape and distribution of the domains. Within this work, as in Müller et al. (2015; 2016), a spherical

domain shape is used. The reference medium $\mathbb{C}_0^{\pm}$ for the lower/upper TS/HS bounds – which is also used to compute $\mathbb{P}_0^{\pm}$ – is defined as the minimum/maximum isotropic optimal zeroth-order bounds of all lower/upper domain bounds $\bar{\mathbb{C}}_\alpha^{\mathrm{UD}\pm}$ using the algorithm described in Nadeau and Ferrari (2001).

As Müller et al. (2015) note, this type of bounding scheme can be used to set limits to the effective properties of complex composites but does not constitute a rigorous second-order bounding scheme.

4.3.8 Resolving the orientation distribution

Different methods exists that incorporate the fiber orientation distribution into the above-mentioned mean field homogenization models. In the most general sense, orientation averaging of a tensor $\mathcal{A}$ can be written as the weighted integral (Advani and Tucker III, 1987)

$$\langle \mathcal{A} \rangle_{\psi_p} = \oint_{\mathcal{S}} \mathcal{A}(\boldsymbol{p}) \psi_p(\boldsymbol{p}) \, \mathrm{d}\boldsymbol{p}. \tag{4.46}$$

Advani and Tucker III (1987) provide a method for directly performing orientation-averaging using the fiber orientation tensors of second and fourth-order. Their method is accurate, fast and simple to apply, but requires all averaged quantities to be transversely isotropic, have major symmetry, to only differ from one another due to a rotation and be equal within their reference frame. Since the strain and stress localization tensors (e.g. in Eq. (4.14)) are generally non-symmetric, orientation-averaging using the Advani-Tucker method is not immediately possible, but can be achieved for the Mori-Tanaka model by modifying the formulation, as detailed in Brylka (2017).

For more than one fiber material, damaged fibers or non-transversely isotropic fiber phases, the Advani-Tucker orientation-averaging cannot be used. In such cases numerical integration schemes such as the

quadrature rules of Lebedev (1976) and related need to be employed and $\mathcal{A}$ is evaluated at N discrete orientations $\boldsymbol{p}_\alpha$ (or integration points) with integration weights w_α and $\sum_{\alpha=1}^{N} w_\alpha = 1$. The orientation averaging is then given as (e.g. Goldberg et al., 2017)

$$\langle \mathcal{A} \rangle_{\psi_p} = \oint_{\mathcal{S}} \mathcal{A}(\boldsymbol{p}) \psi_p(\boldsymbol{p}) \, \mathrm{d}\boldsymbol{p} \approx 4\pi \sum_{\alpha=1}^{N} w_\alpha \mathcal{A}(\boldsymbol{p}_\alpha) \psi_p(\boldsymbol{p}_\alpha). \tag{4.47}$$

In this paper the recently published adaptive integration scheme of Goldberg et al. (2017) is used. The authors show that by introducing the transformation rule

$$\boldsymbol{t}(\boldsymbol{p}) = \frac{\boldsymbol{B}^{-\frac{1}{2}} \boldsymbol{p}}{\| \boldsymbol{B}^{-\frac{1}{2}} \boldsymbol{p} \|} \tag{4.48}$$

Eq. (4.46) can be simplified to

$$\langle \mathcal{A} \rangle_{\psi_p} = \oint_{S} \mathcal{A}(\boldsymbol{p}) \, \psi_p(\boldsymbol{p}) \, \mathrm{d}\boldsymbol{p} = \frac{1}{4\pi} \int_{S} \mathcal{A}(\boldsymbol{t}(\boldsymbol{p})) \, \mathrm{d}\boldsymbol{p}. \tag{4.49}$$

Here, the orientation distribution ψ_p is modeled using the Angular Central Gaussian (ACG) distribution with the symmetric positive-definite second-order parameter tensor $\boldsymbol{B}$ with $\det(\boldsymbol{B}) = 1$.

The numerical integration is also simplified as the transformation $\boldsymbol{t}(\boldsymbol{p})$ adaptively moves the integration points such that they account for the orientation distribution themselves

$$\langle \mathcal{A} \rangle_{\psi_p} = \int_{S} \mathcal{A}(t(\boldsymbol{p})) \, \mathrm{d}\boldsymbol{p} \approx \sum_{\alpha=1}^{N} w_\alpha \mathcal{A}(\boldsymbol{t}(\boldsymbol{p}_\alpha)). \tag{4.50}$$

By doing so, even lower-order integration schemes with fewer integration points can more accurately account for the orientation distribution, especially for non-isotropic or highly aligned orientations states.

The tensor $\boldsymbol{B}$ associated with a second-order fiber orientation tensor $\boldsymbol{N}$ can be computed efficiently within their common eigensystem. We chose an iterative optimization algorithm to compute the eigenvalues B_1 and B_2 ($B_3 = (B_1 B_2)^{-1}$ due to $\det(\boldsymbol{B}) = 1$). During each iteration (index n) the current eigenvalues N_1^n, N_2^n and N_3^n of $\boldsymbol{N}^n$ can be efficiently computed from B_1^n, B_2^n and B_3^n using the Carlson elliptic integrals of the third kind and associated numerical implementations (Montgomery-Smith et al., 2011a). The algorithm continues until the error $\|\boldsymbol{N} - \boldsymbol{N}^n\|$ reaches the target tolerance.

4.4 Benchmark of models and approaches

After introducing the fundamental equations, different models and modeling approaches above, in this section, we present a set of benchmarks that aim at providing a comprehensive comparison. This includes the methods for orientation averaging, the influence of the degree of microstructural accuracy and finally a benchmark of the different mean field homogenization schemes.

4.4.1 Orientation averaging

In this section, the increased efficiency of the adaptive schemes of Goldberg et al. (2017) is highlighted by means of a benchmark of the predicted effective stiffness tensors. Therefore, let us consider a SFRT composite with the mechanical properties summarized in Table 4.1. The artificial microstructure is defined as consisting of fibers with aspect ratio $a = 20$, fiber volume fraction $c_\mathrm{F} = 20\,\%$ and three different orientation states: nearly uniform $\boldsymbol{A} \mathrel{\widehat{=}} \mathrm{diag}(0.4, 0.3, 0.3)$, intermediate $\boldsymbol{A} \mathrel{\widehat{=}} \mathrm{diag}(0.78, 0.2, 0.02)$ and nearly unidirectional $\boldsymbol{A} \mathrel{\widehat{=}} \mathrm{diag}(0.95, 0.03, 0.02)$. A reference solution $\mathbb{C}^\mathrm{ref}$ is generated for all microstructures using the MT scheme and the exact analytical Advani-Tucker averaging scheme

as formulated by Brylka (2017). It is important to note again that the analytical orientation averaging is advantageous when the fiber phase is homogeneous, but may not be used in some cases, e.g. for fibers with different stiffness tensors due to damage modeling. To compare the approaches, the integration order of the Lebedev quadrature rule was repeatedly increased and the effective stiffness tensor was computed using both the direct integration scheme (Eq. (4.47)) and the adaptive scheme of Goldberg et al. (2017) (Eq. (4.50)). In both cases, the symmetry $\psi_p(\boldsymbol{p}) = \psi_p(-\boldsymbol{p})$ of the orientation distribution was employed to decrease the computational effort; more specifically, by integrating only over one hemisphere $\mathcal{S}_{\mathrm{H}} \coloneqq \{\boldsymbol{p} \in \mathbb{R}^3 \,|\, \|\boldsymbol{p}\| = 1 \wedge p_1 \geq 0\}$.
By showing the error $\|\mathbb{C}-\mathbb{C}^{\mathrm{ref}}\|/\|\mathbb{C}^{\mathrm{ref}}\|$ against the number of integration points (i.e. the numerical cost) in Fig. 4.7, it becomes apparent that a considerable gain in accuracy is achieved for a given integration order. Inversely, a similar accuracy can be achieved with lower computational cost by employing the adaptive scheme. This effect is more prominent as the fiber orientation state becomes more highly oriented and the more naïve direct orientation averaging becomes effectively inadequate for nearly unidirectional cases. Therefore, the adaptive scheme of Goldberg et al. with the Lebedev integration scheme of the 35^{th} order and 217 integration points on the hemisphere (434 integration points on full sphere) is used hereafter.

4.4.2 Definition of microstructural setups

In the following sections, the influences of different degrees of accuracy with regard to the microstructural data are studied. Therefore, four characteristic setups are considered. A tabular overview can be found in Table 4.3.

In a first case (referred to as *mean/SL*), the microstructure is characterized by the overall average second-order fiber orientation tensor $\bar{\boldsymbol{N}}$, the nominal fiber volume fraction c_{F} and the overall average fiber

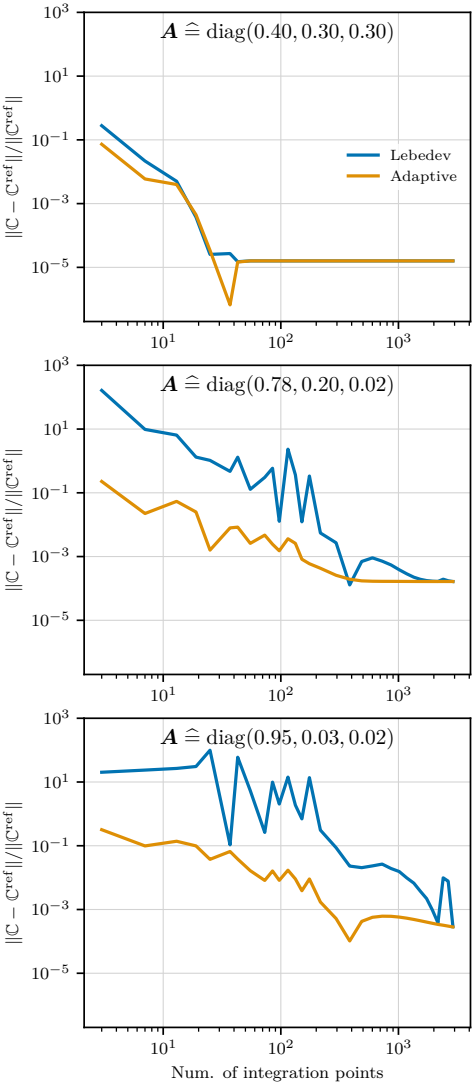

Figure 4.7: Error of the predicted effective stiffness tensor for three fiber orientation tensors using the Lebedev integration points and the adaptive scheme of Goldberg et al. (2017). The reference stiffness was computed using the exact Advani and Tucker III (1987) averaging scheme.

Table 4.3: Overview of the microstructural setups used in the following sections.

Name	Number of layers	Fiber orientation	Fiber length	Fiber diameter	Fiber volume fraction
mean/SL	1	$\bar{\boldsymbol{N}}$	$\bar{l}$	$\bar{d}$	c_F
mean/ML	9	$\boldsymbol{N}^i$	$\bar{l}$	$\bar{d}$	c_F
dist/ML	9	$\boldsymbol{N}^i$	$\psi_l(l)$	$\bar{d}$	c_F
µCT/ML	9	$\boldsymbol{p}^i_\alpha$	l^i_α	$\bar{d}^i_\alpha$	c^i_F
		Layers $i \in [1;9]$ and fibers $\alpha \in [1;N]$ per layer			

aspect ratio $\bar{a} = \bar{l}/\bar{d}$. To highlight the influence of the quasi-layered microstructure, in a second step (*mean/ML*) the material is modeled as a nine-layer composite with each layer (index i) described by its second-order fiber orientation tensor $\boldsymbol{N}^i$ (cf. Fig. 4.4) and the overall average fiber volume fraction and aspect ratio (c_F and $\bar{a}$). Such a setup corresponds to typical integrative simulation approaches using mold filling simulations. In a third setup (*dist/ML*) a stochastically independent fiber length distribution $\psi_l(l)$ (hence $\psi(\boldsymbol{p}, l) = \psi_p(\boldsymbol{p})\psi_l(l)$) is considered for all layers, which is often available from incinerated specimens or pyrolysis. In this work, the fiber length distribution of the µCT analyses is used (cf. Fig. 4.5 and Section 4.2.2). All three microstructures – *mean/SL*, *mean/ML* and *dist/ML* – are accounted for using the method of Goldberg et al. (2017) introduced in the previous section. In a last case (*µCT/ML*), the entire fidelity of the segmented µCT scans is included. Each segmented fiber (index α) is considered in the respective layer (index i) by means of its orientation p^i_α, length l^i_α, diameter d^i_α and aspect ratio $a^i_\alpha = l^i_\alpha/d^i_\alpha$. Each layer is also associated with its specific fiber volume fraction c^i_F.

4.4.3 Prediction of effective elastic properties

The first and arguably most important quantity predicted by any homogenization scheme is the effective stiffness tensor. In the following section, the different approaches' predictions for the effective anisotropic stiffness tensor are evaluated and compared, based on the PA66-GF35 microstructure.

The IDD model is only implicitly part of the following benchmarks through the special cases coinciding with the Mori-Tanaka and Ponte Castañeda-Willis models. This is due to the above-mentioned fact that the symmetry of the effective stiffness and compliance tensors cannot be ensured when exploiting the model's general structure with variable spatial distributions. Furthermore, the results are highly dependent on the fully independent spatial distribution of each fiber which cannot be specified objectively.

Model benchmark and comparison to numerical and experimental results

For comparing the different models, the *mean/SL* microstructure is considered and the Self-Consistent (SC), Mori-Tanaka (MT), Ponte Castañeda-Willis (PCW) and Two-Step (TS) schemes are included. While the SC, MT and TS schemes are fully described by the microstructural setups, the PCW scheme's spheroidal spatial distribution needs to be specified separately, i.e. the aspect ratio a^{D} and orientation $\boldsymbol{p}^{\mathrm{D}}$. In the case of $\boldsymbol{p}^{\mathrm{D}}$ it is reasonable to set it to be equal to the main fiber orientation ($\boldsymbol{e}_1$). The choice of the distribution aspect ratio is less obvious and hence three values $a^{\mathrm{D}} \in \{1, 3, 10, 30\}$ are compared, the first corresponding to an isotropic spatial distribution and the last being approximately the mean fiber aspect ratio.

In addition to the mean field schemes, the effective stiffness tensor was also computed using representative volume elements (RVEs) and the

Fast Fourier Transformation (FFT) solver *FeelMath* (Fraunhofer ITWM, Germany). The RVEs were created using *FiberGenerator* software (Fraunhofer ITWM, Germany) which implements the Sequential Addition and Migration (SAM) algorithm of Schneider (2017). The fibers' length and diameter coincide with those from Table 4.1 and a domain size of $(500\,\mu\mathrm{m})^3$ and a voxel size of $1\,\mu\mathrm{m}$ were chosen. The fourth-order reference fiber orientation tensor for generating the RVEs was taken directly from the results of Hessman et al. (2019)[5] without the necessity of a closure algorithm. To obtain statistically significant results, five RVEs based on this microstructural description were generated and used. A rendering of one RVE is given shown in Fig. 4.8.

The numerical and analytical results are visualized in Fig. 4.9 by applying the method outlined in Böhlke and Brüggemann (2001) and with the PCW scheme using $a^{\mathrm{D}} = 30$. It is apparent that the MT, TS and FFT approaches all predict a similar effective anisotropic stiffness. The SC method predicts a significantly higher stiffness, as is typically expected for the given material type (Tucker III and Liang, 1999; Müller et al., 2015). The PCW scheme also shows a considerable deviation when compared to the other models, especially for in-plane angles around $\pm 45°$. This can be attributed to the constant spheroidal spatial distribution: as the high aspect ratio spatial distribution is coaxial with the main fiber orientation, fibers which are misaligned do not "fit" into their matrix cell and the methodology loses its geometrical and physical meaning. Nevertheless, all predictions lie within the bounds provided by the TS/HS scheme. The conclusions above are supported by the shear moduli shown in Fig. 4.10, where the MT, TS and FFT results match well, whereas the SC and PCW schemes show larger deviations, especially for the G_{12} case. Furthermore, the fact that the MT and TS schemes yield similar results was recently reported by Naili et al. (2020), who analyzed different

[5] cf. Chapter 3 of this thesis

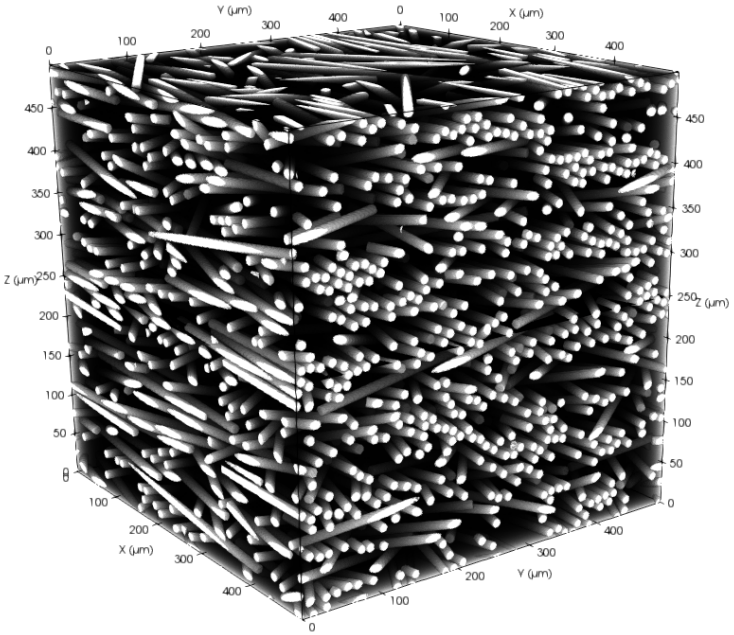

Figure 4.8: Rendering of one of the five RVEs used for the full field FFT homogenization.

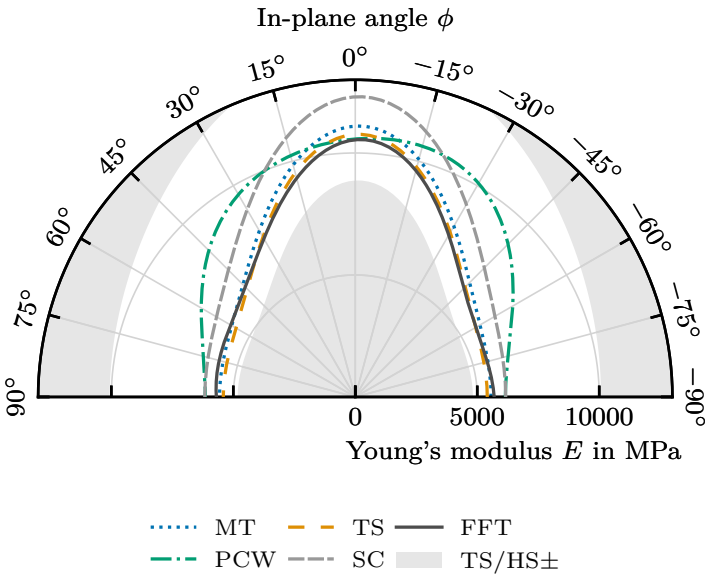

Figure 4.9: Effective Young's modulus for the *mean/SL* setup as predicted by the different analytical models and the numerical scheme (FFT). The TS/HS bounds are shown as reference.

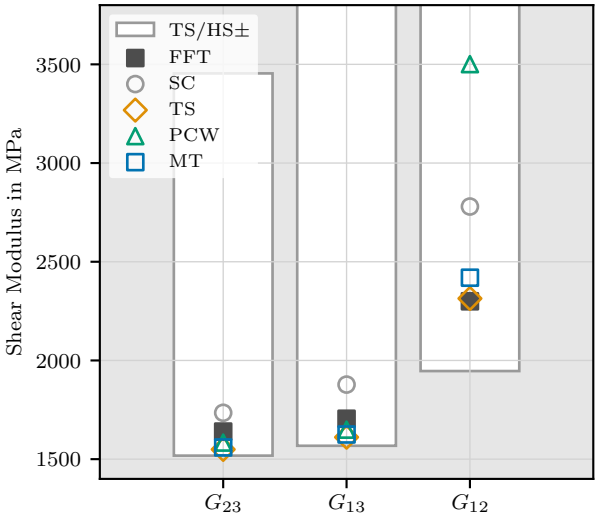

Figure 4.10: Effective shear moduli for the *mean/SL* setup as predicted by the different analytical models and the numerical scheme (FFT). The TS/HS bounds are shown as reference.

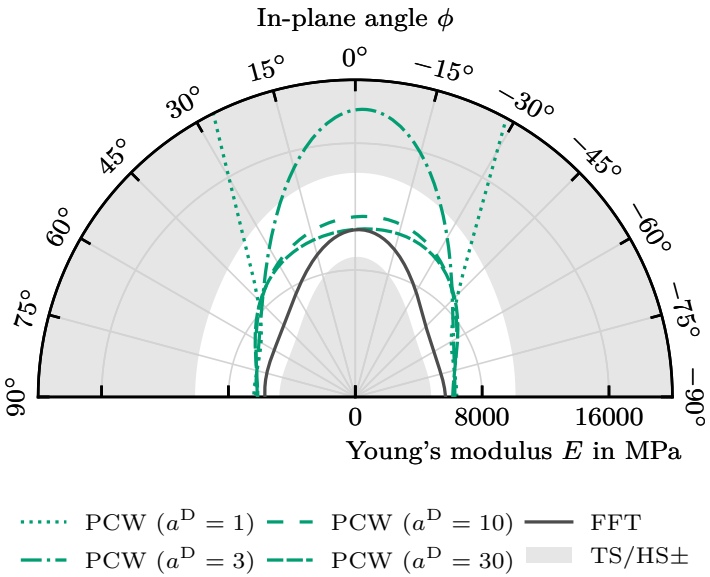

Figure 4.11: Effective Young's modulus for the PCW scheme with the *mean/SL* setup and four distribution aspect ratios of 1, 3, 10 and 30. The FFT results are given as reference.

homogenization schemes for short fiber reinforced composites using a combination of analytical and numerical methods.

To further highlight the influence of the PCW model's spatial distribution on the effective stiffness tensor, let us compare the predictions for the four different distribution aspect ratios of $a^{\mathrm{D}} \in \{1, 3, 10, 30\}$. The results are shown in Fig. 4.11. As a^{D} is decreased, the stiffness strongly increases for in-plane angles between $-45°$ and $45°$. For $a^{\mathrm{D}} = 1$, the orientation-dependent Young's modulus becomes unphysical and the stiffness tensor loses positive definiteness. The intuition behind this behavior is again that the fibers – with their aspect ratio of $a = 27$ – are incompatible with a spherical spatial distribution with volume fraction of $c_{\mathrm{F}} = 19.3\,\%$,

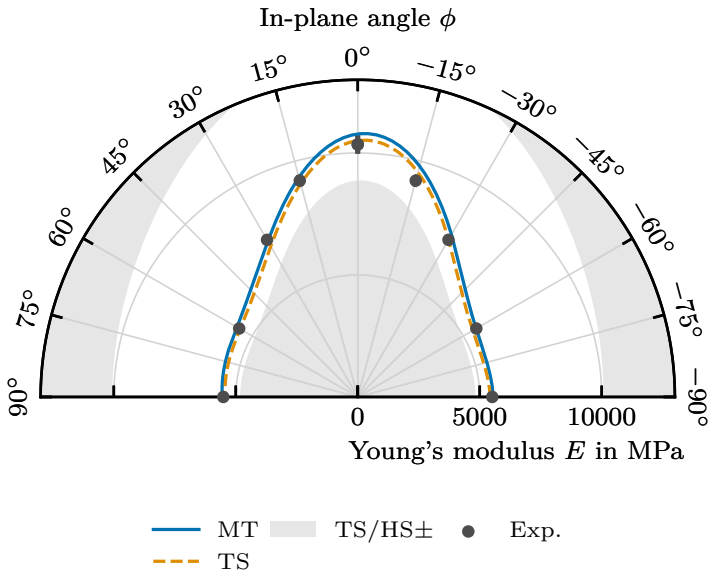

Figure 4.12: Comparison of the MT and TS schemes' effective Young's modulus for the *µCT/ML* setup and experimental data.

independent of the fibers' orientation. This issue can also be seen in Fig. 4.6.

The above results for the *mean/SL* microstructure indicate that only the MT and TS schemes are able to correctly and robustly approximate the effective stiffness tensor from the FFT homogenization. In a next step, both models are applied to the detailed *µCT/ML* microstructure and compared to the experimental results. As shown in Fig. 4.12, both models give accurate results that lie within close proximity of the experimental results, neither approach being superior. It is worth clarifying that the results are obtained directly from the analyzed microstructure and

literature constituent properties without the need for any parameter identification.

Influence of microstructural description

Next, all four different parametrizations of the composite's microstructure (*mean/SL*, *mean/ML*, *dist/ML*, *μCT/ML* and *μCT/ML*) are considered. For clarity, only the MT scheme is used for the comparison with results holding equivalently for the other schemes. As can be seen in Fig. 4.13 all four degrees of accuracy are able to capture the general shape of the anisotropic stiffness. Nevertheless, the *mean/SL* setup shows the largest deviations, especially at angles of approximately $\pm 45°$. The corresponding multilayer setup *mean/ML* increases the accuracy in these regions notably. By including the fiber length distribution (*dist/ML*) the stiffness in main fiber direction is predicted more accurately and the *μCT/ML* setup yields the most exact – albeit very similar – prediction, lying within the one standard deviation interval of the experimental data in all but one cases.

These results show that, while the high-fidelity microstructure from the segmented μCT data offers the most exact results, a stochastically independent fiber length distribution offers comparable accuracy. Reasonable predictions for the effective stiffness tensor are obtained by a all setups with maximum errors remaining below $10\,\%$.

4.4.4 Prediction of stresses in the fibers

In this section the influence of the different models and of the microstructural setup on the prediction of the fiber stresses is studied. The results hold equivalently for the fiber strains, which are not further considered here.

Two example macroscopic loadings with unit magnitude of $\bar{\sigma} = 1\,\mathrm{MPa}$ are applied: one in the main fiber direction ($\bar{\boldsymbol{\sigma}}_1 = \bar{\sigma}\, \boldsymbol{e}_1 \otimes \boldsymbol{e}_1$) and one at

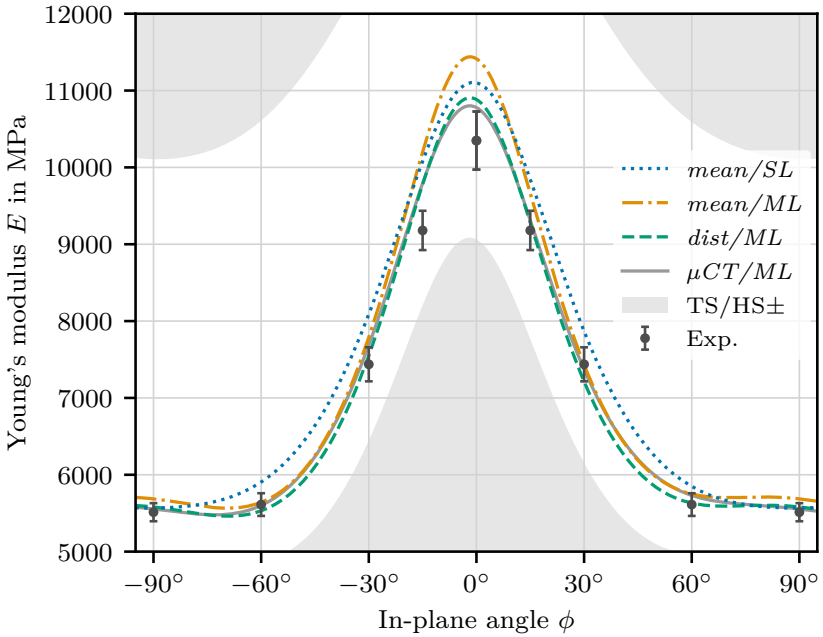

Figure 4.13: Comparison of the effective Young's modulus computed with the MT model for the four microstructural setups: single layer mean fiber length (*mean/SL*), multilayer mean fiber length (*mean/ML*), fiber length distribution (*dist/ML*) and layered µCT data (*µCT/ML*). The TS/HS bounds and experimentally measured stiffness values are shown as reference.

an angle of $90°$ ($\bar{\boldsymbol{\sigma}}_2 = \bar{\sigma}\, \boldsymbol{e}_2 \otimes \boldsymbol{e}_2$). The fiber stresses are then computed using the stress localization tensors $\boldsymbol{\sigma}_{i,\alpha} = \mathbb{B}_\alpha\, [\bar{\boldsymbol{\sigma}}_i]$ for the two examples $i \in \{1, 2\}$. In the following sections, the comparisons are performed on the basis of the maximum principal stress, with other scalar invariants being equally feasible.

The figures of this section feature the cumulative distribution function of the fiber stresses, which represents the fraction of fibers whose stresses are less or equal to a given stress. As such, the value of the cumulative distribution function lies between zero and one.

Comparison of models and full field results

To compare the fiber stress prediction of the different models, the *mean/SL* setup is considered. In addition to the mean field models, results from the full field (FFT) computations are also given.

From Fig. 4.14a one can see that MT, TS and PCW schemes yield similar results in the $0°$ case with the MT model predicting the highest maximum stresses. The SC scheme gives higher minimum and lower maximum fiber stresses, deviating from the other schemes. From the FFT computation we obtain a stress distribution that is more spread out and shows considerably higher maximum stresses than the mean field schemes. This can be explained by the fact that local stress concentrations can be resolved in the full field calculations which are not part of the averaged nature of the mean field schemes.

When loaded perpendicular to the main fiber direction ($90°$), as shown in Fig. 4.14b, both the mean field schemes and the full field FFT computation lie close to each other. The greatest difference of the cumulative distribution function are found for higher stresses, but contrary to the $0°$ loading case, the FFT results lie within the range spanned by the different mean field models. As before, the four mean field schemes only vary slightly and no model yields results that are clearly superior, i.e. closer to the full field results for the full stress range.

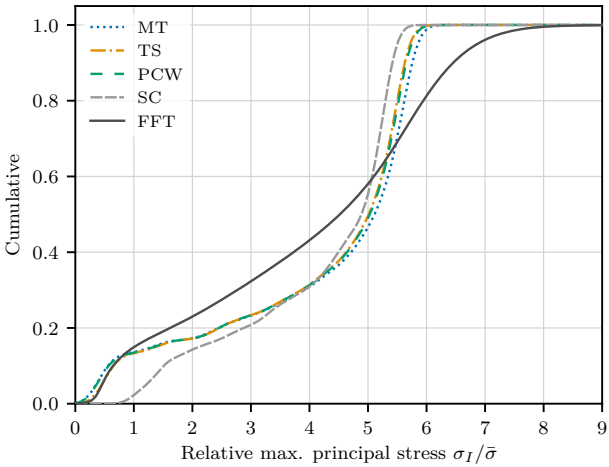

(a) Load in main fiber direction (0°).

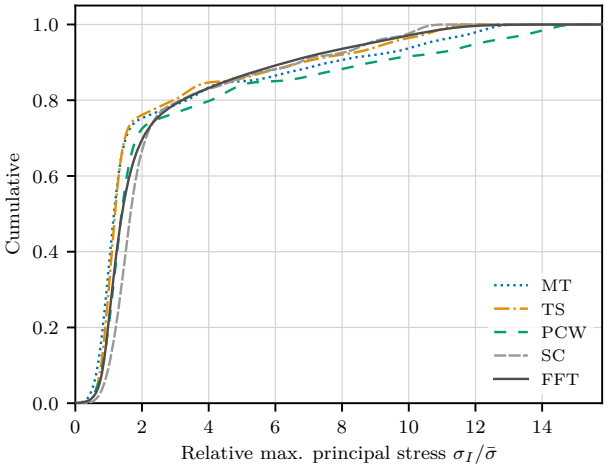

(b) Load perpendicular to main fiber direction (90°).

Figure 4.14: Cumulative distribution function of the maximum principal stress in the fiber phase for the four mean field models and the full field (FFT) calculations. The *mean/SL* microstructure setup was used for the comparison.

Contrary to suggestions in the literature (e.g. Jain et al., 2013), the MT and TS models both yield comparable results, even though the latter is based on a simple interaction scheme between the different fibers. At the same time, the results support the wide-spread application of the TS model in industry and commercial material modeling software.

Influence of microstructural description

The influence of the accuracy of the microstructural description is again evaluated based on the MT scheme. In Fig. 4.15 the cumulative distribution function of fiber stresses are given for both the $0°$ and $90°$ loadings and for all four microstructural setups. Similar to the results for the effective stiffness, only considering a single layer and mean fiber length (*mean/SL*) already allows the general behavior and the orientation-dependency to be recovered. While including the layered microstructure (*mean/ML*) has a minor influence, more accurate results are obtained by including the fiber length distribution *dist/ML*, for which the results nearly coincide with the even more detailed computation using the raw µCT data (*µCT/ML*). These differences are more pronounced for the $0°$ loading case, whereas in the $90°$ all four stress predictions lie close to each other.

4.5 Summary & conclusions

The present work revisited the topic of mean field homogenization of short fiber reinforced composites. Numerical and experimental studies were performed based on a commercial-grade short glass fiber reinforced polyamide 6.6 with a fiber mass fraction of of $35\,\%$.

A set of common mean field schemes were covered: the Mori-Tanaka (MT), Self-Consistent scheme (SC), Ponte Castañeda-Willis (PCW), Interaction Direct Derivative (IDD) and Two-Step (TS) models. We were

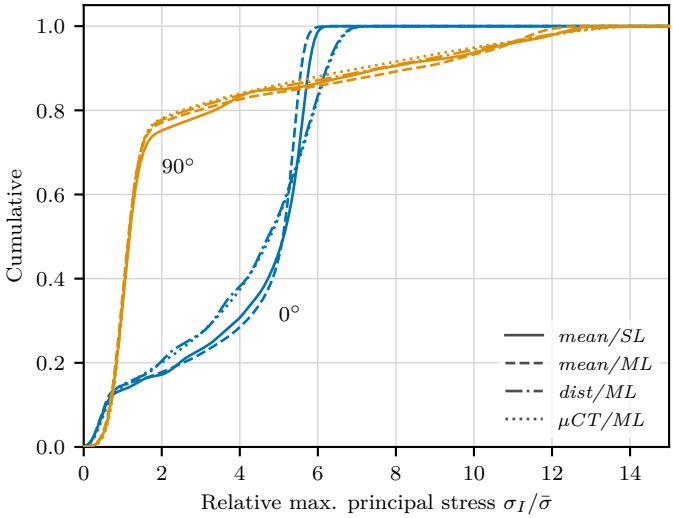

Figure 4.15: Cumulative distribution function of the fiber stresses computed by the MT scheme for four different microstructural setups.

able to show that the MT, PCW and IDD models can be given in a *unified* formulation which only differs in the location and specifics of the distribution polarization tensor, thereby highlighting their connections, limitations and allowing for a well-founded comparison.

In a series of benchmarks, the different mean field schemes and modeling approaches were compared against numerical results from Fast Fourier Transformation (FFT) homogenization and experimental data. These benchmarks showed that only the MT and TS schemes are generally applicable for the given material type, the former's application being restricted to homogeneous isotropic fiber properties. Both schemes yield accurate effective stiffness tensors that are in good agreement with experimental results. The IDD and PCW schemes require the fibers' spatial distribution to be specified separately, which is both difficult to determine and limited geometrically for composites with misaligned

fibers, restricting the application of these models. Regarding the prediction of fiber stresses, all mean field schemes showed deviations when compared with the stress prediction from the full field FFT computations when loaded in the main fiber direction, underestimating the maximum fiber stresses.

Since high-accuracy microstructural data is often not available, we compared different modeling setups. The results show that reasonable predictions for effective elastic properties are possible even with limited microstructural information. Including the layered microstructure and a separately measured fiber length distribution yielded results that are comparable to high-fidelity data from a single fiber segmentation. These results also hold for the fiber stress distributions, where the predictions for the different microstructural setups differed marginally. Including the fiber length distribution leads to results that are virtually coincident with the single fiber data.

The adaptive integration scheme of Goldberg et al. (2017) was used to numerically resolve the microstructure. A comparison to a more naïve approach showed that high accuracy results can be achieved at a fraction of the computational cost, especially for microstructures that feature strongly aligned fibers, commonly found in real parts.

Chapter 5

A micromechanical cyclic damage model for high cycle fatigue failure of short fiber reinforced composites[1]

5.1 Introduction

This chapter addresses the topic of micromechanical modeling of fatigue damage of SFRCs with the aim of predicting the high-cycle fatigue life of different composite variants and microstructural states. Within the scope of this thesis, this is applied to the example material class of short glass fiber reinforced PA6.6. The modeling approach thereby uses micromechanical data in the form of fiber orientation tensors from µCT scans (cf. Chapter 3). Both the damage of the fiber and its vicinity, and cyclic damage processes in the matrix are modeled using an analytical mean field homogenization scheme previously discussed in Chapter 4. A cycle-based formulation based on the work of Peerlings et al. (2000) is used to facilitate simulating the large number of cycles required for high-

[1] This chapter, including all tables and figures, is based on the publication "A micromechanical cyclic damage model for high cycle fatigue failure of short fiber reinforced composites" (Hessman et al., 2023), with some minor typographical and formatting changes to improve the readability and coherence within this thesis.

cycle fatigue load cases. The model is implemented in the commercial finite element solver *Abaqus* (Dassault Systèmes SE, France) and the algorithm as well as numerical aspects are discussed. The required parameters of both models are identified using experimental data and finite element simulations on specimen level are used to evaluated the model's capabilities to model and predict high-cycle fatigue in different composite grades with varying microstructures.

Chapter structure

This chapter is structured in five parts. First, in Section 5.2 the employed materials' information and the experimental data is summarized. The analytical micromechanical framework is introduced in Section 5.3. Section 5.4 covers the modeling approach with respect to fiber-related damage processes, whereas the cyclic matrix damage model is described in Section 5.5. Lastly, Section 5.6 presents various results from finite element simulation using the presented models and comparisons to the experimental data. A summary of the chapter's content and results is given in Section 4.5.

5.2 Material and experimental results

5.2.1 Short glass fiber reinforced polyamide 6.6

While the methods and models covered in this work are of general nature and applicable to many types of SFRCs, a particular class of commercial-grade short glass fibers reinforced polyamide 6.6 composites was chosen as an example material. Different varieties of the composite are considered: one unreinforced grade (PA66) and composite grades with fiber mass fractions of $15\,\%$, $25\,\%$, $35\,\%$ and $50\,\%$, referred to hereafter as PA66-GF15, PA66-GF25, PA66-GF35 and PA66-GF50.

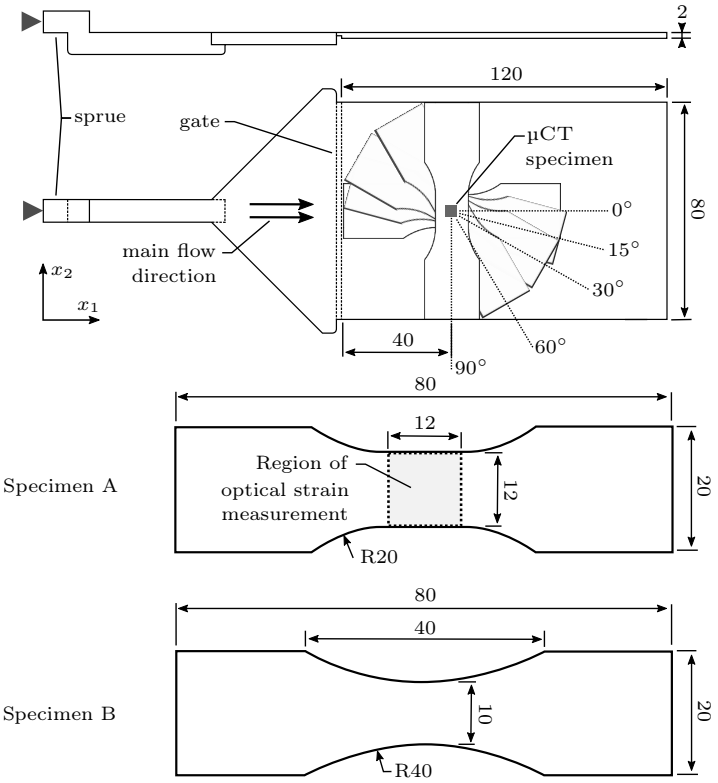

Figure 5.1: Outline of the plate geometry and location of µCT, tensile (A) and fatigue (B) specimens (units in mm).

Rectangular plates of $120 \times 80 \times 2\,\mathrm{mm}^3$ were injection molded for all materials (cf. Fig. 5.1). From these plates composite specimens for quasi-static tensile testing (Specimen A in Fig. 5.1, cf. Becker (2009)) were machined out of the center region of each plate at angles of $0°$, $15°$, $30°$, $60°$ and $90°$. Details on the experimental setup are given below in Section 5.2.3. The composite specimens for fatigue testing (Specimen B in Fig. 5.1) were taken at the same position and at angles of $0°$ and $90°$. In the case of the unreinforced material the specimens were cut out at $0°$. More information is given in Section 5.2.4. Finally, small cuboid specimens were also cut from the plates and used for analyzing the microstructure (Hessman et al., 2019)[2], as detailed in Section 5.2.2.

To keep the material state constant and reproducible, all specimens were subjected to a re-drying process in a vacuum chamber for $72\,\mathrm{h}$ at $80\,°\mathrm{C}$ and an absolute pressure below $50\,\mathrm{mbar}$, to remove any water absorbed by the polyamide 6.6 matrix and to remove potential residual stresses due to injection molding.

5.2.2 Results of the microstructural analysis

The influence of the microstructure (fiber orientation, length and volume fraction) of SFRCs on their mechanical behavior has been widely discussed in literature (Fakirov and Fakirova, 1985; Folgar and Tucker III, 1984; Horst and Spoormaker, 1996; Fu and Lauke, 1996; Fu et al., 1999; 2000; Arif et al., 2014; Bernasconi et al., 2007; Hessman et al., 2019; 2021, among others). This is especially relevant for short fiber reinforced thermoplastics – like those introduced in the subsection above – where during the injection molding process the fibers are aligned due to the shear flow in the cavity. This results in fibers being predominantly aligned with the main flow direction (x_1 direction in Fig. 5.1) in the so called "shell" region of the part cross-section, whereas the "core" (i.e.,

[2] cf. Chapter 3 of this thesis

middle) section of a part predominantly exhibit fibers which are oriented perpendicular to both the main flow direction and surface normal (x_2 direction in Fig. 5.1) (Fakirov and Fakirova, 1985; Horst and Spoormaker, 1996; Arif et al., 2014; Bernasconi et al., 2007; Hessman et al., 2019).

This quasi-layered structure of the part and the heterogeneity of the microstructure need to be resolved and analyzed in order to accurately model the given material type. To this end Hessman et al. (2019)[3] describe a single fiber segmentation method (SFS) to obtain accurate microstructure statistics based on x-ray micro-computed tomography (µCT). Using this method, high resolution scans of the PA66-GF35 material used in this work were analyzed and descriptors such as the second-order fiber orientation tensor (Advani and Tucker III, 1987; Kanatani, 1984) and fiber length distributions were obtained. Further details can be found in the original publication. For the work at hand the layer-wise second-order fiber orientation tensor and the average fiber length and diameter for the PA66-GF35 material are used.

In addition, data from Pietrogrande et al. (2021) is used, where µCT scans of all five reinforced materials were processed using the commercial software *VGSTUDIO MAX* (VG, Volume Graphics GmbH, Germany). The mean fiber length and diameter were assumed to be equal in all used grades and set to the above-mentioned results from Hessman et al. (2019)[4] for the PA66-GF35 material.

An overview of the fiber orientation data from Pietrogrande et al. (2021) (VG) and Hessman et al. (2019)[5] (SFS) is given in Fig. 5.2. In all cases, the shell-core morphology is clearly visible. A partially different curve is obtained for the PA66-GF15 material, which yields a less oriented state in the x_1 direction (N_{11} component), and the PA66-GF50 material, where the core layers take up a considerably larger portion of the cross-

[3] cf. Chapter 3 of this thesis
[4] cf. Chapter 3 of this thesis
[5] cf. Chapter 3 of this thesis

Table 5.1: Summary of the elastic properties of the PA66 matrix and glass fiber materials as well as the microstructural properties of the composite grades.

PA66 matrix Young's modulus	$E_{\mathrm{M}} = 3\,\mathrm{GPa}$
PA66 matrix Poisson's ratio	$\nu_{\mathrm{M}} = 0.4$
Fiber Young's modulus	$E_{\mathrm{F}} = 72\,\mathrm{GPa}$
Fiber Poisson's ratio	$\nu_{\mathrm{F}} = 0.22$
Fiber volume fraction PA66-GF15	$c_{\mathrm{F}}^{\mathrm{GF15}} = 7.25\,\%$
Fiber volume fraction PA66-GF25	$c_{\mathrm{F}}^{\mathrm{GF25}} = 12.90\,\%$
Fiber volume fraction PA66-GF35	$c_{\mathrm{F}}^{\mathrm{GF35}} = 19.30\,\%$
Fiber volume fraction PA66-GF50	$c_{\mathrm{F}}^{\mathrm{GF50}} = 30.70\,\%$
Mean fiber diameter	$\bar{d} = 10.2\,\mathrm{mm}$
Mean fiber length	$\bar{l} = 275.7\,\mathrm{mm}$

section, such that overall more fiber are aligned in the x_2 direction (N_2 component).

More detailed explanations of the analysis setups and regarding the use of fiber orientation tensors for describing the fiber orientation state in SFRCs can be found in the publications of Hessman et al. (2019)[6] and Pietrogrande et al. (2021) as well as Kanatani (1984); Advani and Tucker III (1987); Müller and Böhlke (2016).

5.2.3 Quasi-static testing

Fiber breakage and interfacial damage are an integral part of the damage mechanics of short fiber reinforced composites (Sato et al., 1991; Rolland et al., 2016; 2018). In Section 5.4 below, a combined fiber/fiber-interface damage model is introduced which accounts for these processes. To qualitatively or even quantitatively assess the amount of damage for a given type and amount of loading, in-situ x-ray micro-computed tomography (in-situ µCT) can be used (Rolland et al., 2016; 2018) but is associated with considerable cost and effort. Within this work, an

[6] cf. Chapter 3 of this thesis

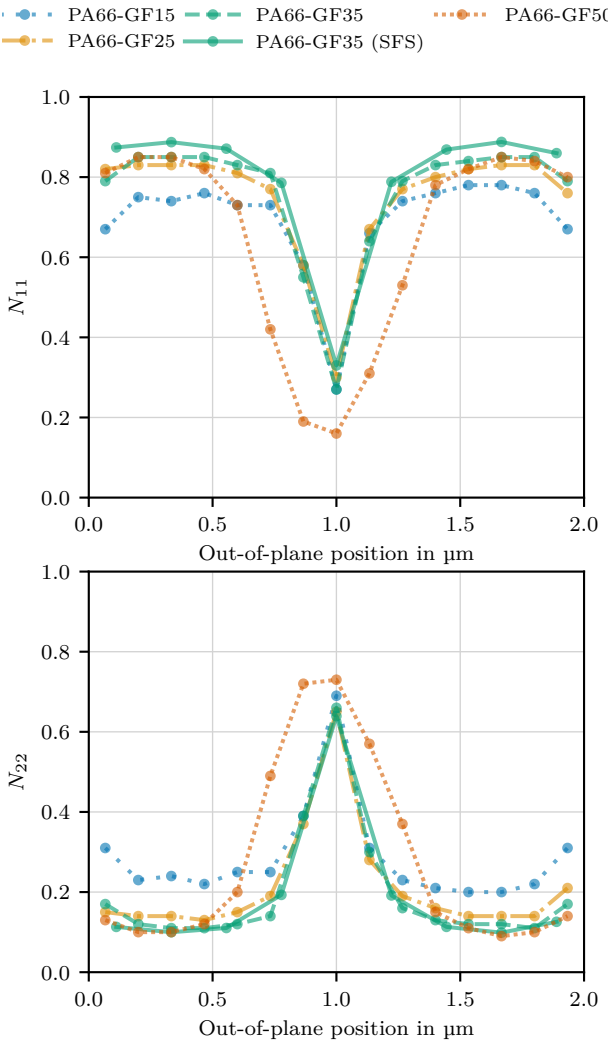

Figure 5.2: Visualization of the pseudo-layered fiber orientation data of the four composite materials from Pietrogrande et al. (2021) (solid lines), as described by the first two diagonal components (N_{11} and N_{22}) of the fiber orientation tensor. The results of the single fiber segmentation (SFS) from Hessman et al. (2019)(cf. Chapter 3 of this thesis) for the PA66-GF35 composite are shown as dashed lines.

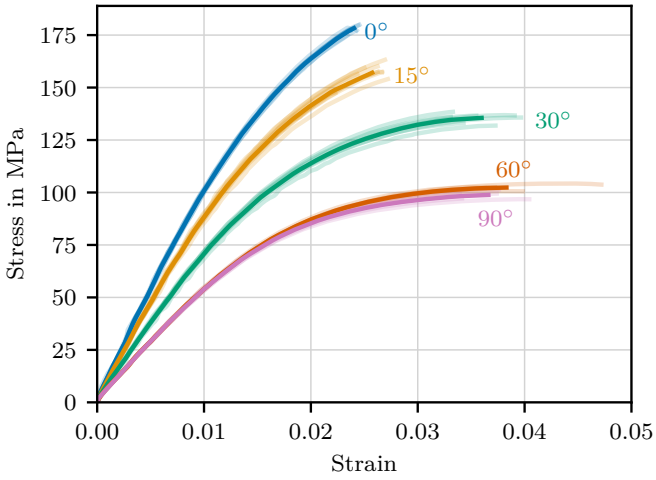

Figure 5.3: Stress-strain curves for the PA66-GF35 composite material at angles of 0°, 15°, 30°, 60° and 90°. The different tests per angle and the average curves are shown. All tests were performed at room temperature and using dried specimens.

inverse approach is chosen (cf. Kabir et al., 2006), where experimental data from tensile tests of composite specimens at different loading angles with respect to the main fiber orientation are used to identify the model parameters of the damage model.

The tensile tests were performed at the Institute of Engineering Mechanics (Karlsruhe Institute of Technology (KIT), Germany). Results of these tests were previously also reported in Hessman et al. (2021)[7]. A Zwick (ZwickRoell GmbH & Co. KG, Germany) tensile testing setup was used in combination with a *GOM Aramis 3D 4M* (GOM GmbH, Germany) optical strain measurement setup. Statistical results were obtained by testing between five and nine specimens per case and the nominal strain rate was set to $1\,\%\,\mathrm{min}^{-1}$. From this data, one averaged

[7] cf. Chapter 4 of this thesis

stress-strain curve was generated per angle for use in all further analyses. An overview of the resulting stress-strain curves are shown in Fig. 5.3. As typical for the given material class (cf. Müller et al., 2015; Hessman et al., 2021), the material is considerably stiffer at angles close to the main flow direction (cf. Fig. 5.1). As the angle increases, the average stress at failure successively decreases from $178\,\mathrm{MPa}$ ($0°$) to $99\,\mathrm{MPa}$ ($90°$). At the same time, the average strain at failure increases from $2.4\,\%$ for the $0°$ curve to a maximum of $3.8\,\%$ for $60°$ and a marginally lower value of $3.7\,\%$ for $90°$. Overall, the scatter within one orientation class is low, with the largest deviations found in the strain at failure for the tests are $60°$ and $90°$. Additional data related to the orientation-dependent Young modulus of the material and details on the experimental campaign can be found in Hessman et al. (2021)[8].

5.2.4 Fatigue testing

Both the unreinforced and short glass fiber reinforced polyamide 6.6 materials were tested under fatigue loading in the Robert Bosch GmbH Corporate Research Polymer Engineering department (Renningen, Germany). The test setup consisted of a servo-hydraulic Instron 8000 testing machine and a $25\,\mathrm{kN}$ load cell. The load frequency was adjusted between $1\,\mathrm{Hz}$ and $20\,\mathrm{Hz}$ for each specimen in order to limit self-heating effects. Throughout this work the force-controlled tests were performed at a load ratio of $R_F = F_{\min}/F_{\max} = 0$, meaning that the fatigue test load oscillates between $F_{\min} = 0\,\mathrm{N}$ and $F_{\max} = 2F_{\mathrm{amp}}$.

In order to study both the influence of the fiber mass fraction and of the orientation of the reinforcing glass fibers, tests at different fiber orientations and for composite grades with different fiber mass fractions were considered: $90°$ fiber orientation for PA66 reinforced with short glass fibers of $15\,\%$, $25\,\%$, $35\,\%$ and $50\,\%$ fiber mass fraction (from Pietrogrande

[8] cf. Chapter 4 of this thesis

Table 5.2: Summary of available experimental results.

	µCT	Tensile					Fatigue	
		0°	15°	30°	60°	90°	0°	90°
PA66							×	
PA66-GF15	×[a]							×[a]
PA66-GF25	×[a]							×[a]
PA66-GF35	×[a/b]	×	×	×	×	×	×	×[a]
PA66-GF50	×[a]							×[a]

[a]Results were taken from Pietrogrande et al. (2021).
[b]The µCT data was published in Hessman et al. (2019).

et al. (2021)) and $0°$ fiber orientation for a fiber mass fraction of $35\,\%$ and unreinforced PA66 thermoplastic material, also cut out in an angle of $0°$. The available fatigue data is summarized in Table 5.2.

S-N curves for the unreinforced PA66 material and the PA66-GF35 $0°$ and $90°$ tests are given in Fig. 5.4 alongside linear regression curves within the log-log plot. It can be seen that the fatigue strength of the unreinforced PA66 material lies between that of the PA66-GF35 $0°$ with higher fatigue strength and the PA66-GF35 $90°$ data with lower fatigue strength. While the increased strength in the $0°$ tests can be attributed to the strengthening effect of the mostly aligned glass fibers, the decreased strength of the $90°$ case suggests a weakening effect of the mostly misaligned fibers.

In Fig. 5.5 fatigue results for the unreinforced material and the $90°$ tests of the four different fiber fractions are shown. Comparing the curves, it first becomes apparent that the fatigue strengths of the reinforced materials are lower in most cases than that of the unreinforced material. In alignment to the previous case, the reason for the strength (or lifetime) reduction can be attributed to the fact that the misaligned fibers do not increase the strength (i.e., reinforce the composite) enough to counteract

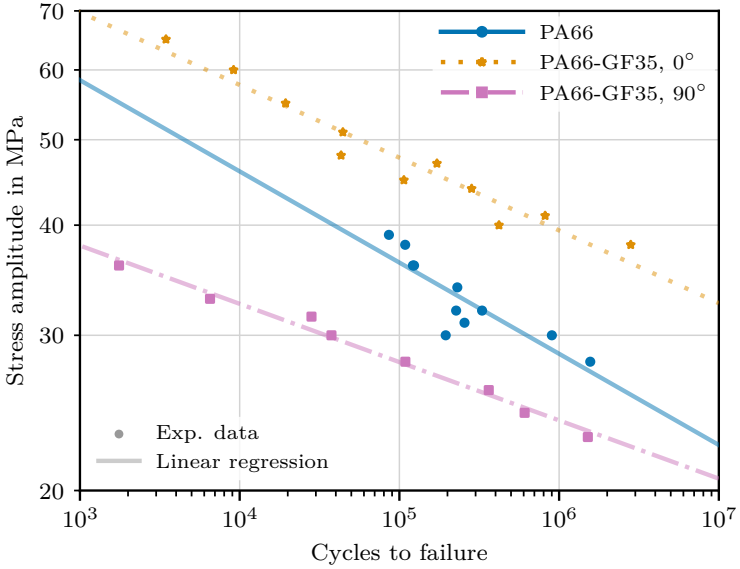

Figure 5.4: S-N curves for the unreinforced PA66 and the composite PA66-GF35 0° and 90° fatigue tests, highlighting the influence of the fiber orientation.

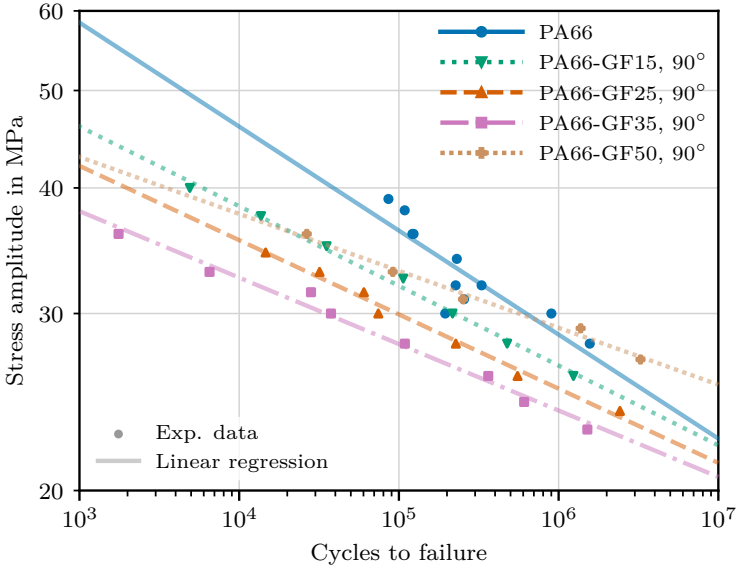

Figure 5.5: S-N curves for the 90° and unreinforced matrix tests, highlighting the influence of the fiber content.

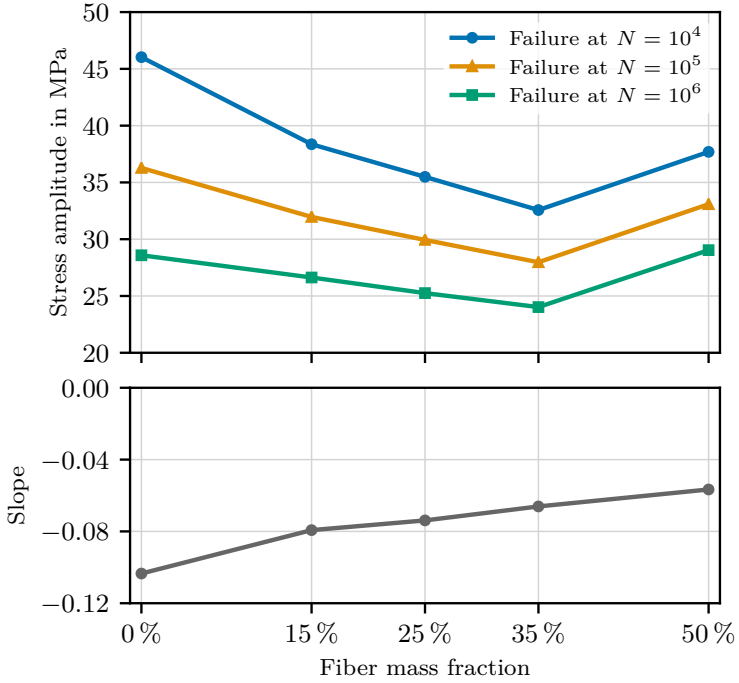

Figure 5.6: Slope and intercept (at $N = 10^4$, $N = 10^5$ and $N = 10^6$) of the linear fatigue regression curves for the $90°$ fatigue tests as a function of the fiber mass fraction.

the additional local stress concentrations in the matrix in the vicinity of the fibers. This effect then leads to an early failure when compared to the unreinforced case.

To further highlight this effect, the fatigue strength was evaluated at cycles to failure of $10^4, 10^5$ and 10^6 for the $90°$ and bulk tests using their regression curves. As shown in Fig. 5.6, the fatigue strengths decrease monotonically from the $0\,\%$ to $35\,\%$ fiber mass fraction specimens before increasing again at $50\,\%$. At the same time, the S-N curve slope increases monotonically throughout the fiber fraction range.

5.3 Micromechanical framework

Multiscale methods are crucial to modeling SFRC materials as they allow the linkage of microscopic material properties and structures to the macroscopic properties of the composite material, such as the effective stiffness. Furthermore, they enable the computation of the average microscopic stresses and strains for a given macroscopic loading scenario, thereby facilitating micromechanical models for damage and failure of the material.

5.3.1 Two-Step homogenization scheme

Within this work we have chosen the Two-Step (TS) mean-field homogenization scheme introduced by Pierard et al. (2004) in the Mori-Tanaka/Voigt variant, as it allows for microstructural damage phenomena to be included and guarantees valid result with respect to the symmetry of the stiffness tensor (cf. Hessman et al., 2021; Pierard et al., 2004; Benveniste et al., 1991; Ferrari, 1991; 1994). Some other models were shown to either be unsuitable for the given type of materials or may yield unphysical results (cf. Hessman et al., 2021; Benveniste et al., 1991; Ferrari, 1991). A detailed overview and summary of mean field homogenization schemes for SFRCs and SFRTs including more detailed derivations for the TS method are given in Hessman et al. (2021)[9] as well as in Tucker III and Liang (1999); Klusemann and Svendsen (2010); Müller et al. (2015; 2016); Pierard et al. (2004).

Below, a short summary of the relevant equations of the Two-Step Mori-Tanaka/Voigt scheme is given. For simplicity, the label TS is not used in the naming of the tensors related to the homogenization method.

[9] cf. Chapter 4 of this thesis

The effective stiffness tensor $\bar{\mathbb{C}}$ of a composite relates the macroscopic stress and strain tensors

$$\bar{\boldsymbol{\sigma}} = \bar{\mathbb{C}}\,[\bar{\boldsymbol{\varepsilon}}]\,. \tag{5.1}$$

In the applied TS homogenization scheme we can compute the overall effective stiffness tensor based on microstructural information by taking the Voigt average of a set of unidirectional (UD) domains (cf. Pierard et al., 2004) with indices $\alpha = 1 \dots n_{\mathrm{F}}$ and stiffness tensors $\bar{\mathbb{C}}_{\alpha}^{\mathrm{UD}}$

$$\bar{\mathbb{C}} = \left\langle \bar{\mathbb{C}}_{\alpha}^{\mathrm{UD}} \right\rangle_{\mathrm{F},\alpha}\,. \tag{5.2}$$

The averaging over these domains is defined as

$$\langle\cdot\rangle_{\mathrm{F},\alpha} = \sum_{\alpha=1}^{n_{\mathrm{F}}} \frac{c_{\alpha}}{c_{\mathrm{F}}}\,(\cdot)_{\alpha}, \tag{5.3}$$

where c_{α} is the volume fraction of a fiber family of equal orientation and shape (i.e., length and diameter) and c_{F} is the overall fiber volume fraction ($c_{\mathrm{F}} = \sum_{\alpha=1}^{n_{\mathrm{F}}} c_{\alpha}$). Conversely, the matrix volume fraction of the composite reads $c_{\mathrm{M}} = 1 - c_{\mathrm{F}}$. Each UD domain consists of the matrix material and fibers of one fiber family. The fiber volume fraction within each UD domain is chosen such that the matrix volume fraction always remains equal to c_{M}.

Applying the Mori-Tanaka homogenization scheme (Mori and Tanaka, 1973; Benveniste, 1987) to each UD domain we get the domain stiffness tensor

$$\bar{\mathbb{C}}_{\alpha}^{\mathrm{UD}} = \mathbb{C}_{\mathrm{M}} + c_{\mathrm{F}}\Delta\mathbb{C}_{\alpha}\mathbb{A}_{\alpha}^{\mathrm{dil}}\left(\mathbb{I}^{\mathrm{S}} - c_{\mathrm{F}}\mathbb{P}_{\alpha}\Delta\mathbb{C}_{\alpha}\mathbb{A}_{\alpha}^{\mathrm{dil}}\right)^{-1} \tag{5.4}$$

with

$$\mathbb{P}_{\alpha} = \mathbb{E}_{\alpha}\mathbb{C}_{\mathrm{M}}^{-1} \tag{5.5}$$

and

$$\mathbb{A}_{\alpha}^{\mathrm{dil}} = \left(\mathbb{I}^{\mathrm{S}} + \mathbb{P}_{\alpha}\Delta\mathbb{C}_{\alpha}\right)^{-1}. \tag{5.6}$$

Here, $\mathbb{P}_\alpha$ is Hill's polarization tensor (Hill, 1963), $\mathbb{E}_\alpha$ refers to Eshelby's tensor (Eshelby, 1957) and $\mathbb{A}_\alpha^{\mathrm{dil}}$ is the fiber's strain localization tensor for the dilute approximation. $\Delta\mathbb{C}_\alpha = \mathbb{C}_\alpha - \mathbb{C}_\mathrm{M}$ is used as shorthand for the difference between the stiffness tensor $\mathbb{C}_\alpha$ of fiber family α and the matrix stiffness $\mathbb{C}_\mathrm{M}$.

We can then compute $\bar{\mathbb{C}}$ from Equations (5.2) and (5.4)

$$\bar{\mathbb{C}} = \mathbb{C}_\mathrm{M} + c_\mathrm{F} \left\langle \Delta\mathbb{C}_\alpha \mathbb{A}_\alpha^{\mathrm{dil}} \left(\mathbb{I}^\mathrm{S} - c_\mathrm{F} \mathbb{P}_\alpha \Delta\mathbb{C}_\alpha \mathbb{A}_\alpha^{\mathrm{dil}} \right)^{-1} \right\rangle_{\mathrm{F},\alpha} . \tag{5.7}$$

To compute the average strain of a fiber family ($\boldsymbol{\varepsilon}_\alpha$) from the macroscopic stain $\bar{\boldsymbol{\varepsilon}}$ we use the fiber strain localization tensor $\mathbb{A}_\alpha$, which in the given model can be computed by (Benveniste, 1987; Benveniste et al., 1991; Hessman et al., 2021)

$$\mathbb{A}_\alpha = \mathbb{A}_\alpha^{\mathrm{dil}} \left(\mathbb{I}^\mathrm{S} - c_\mathrm{F} \mathbb{P}_\alpha \Delta\mathbb{C}_\alpha \mathbb{A}_\alpha^{\mathrm{dil}} \right)^{-1} . \tag{5.8}$$

Then, we can compute $\boldsymbol{\varepsilon}_\alpha = \mathbb{A}_\alpha \left[\bar{\boldsymbol{\varepsilon}}\right]$ and from this the average fiber stress $\boldsymbol{\sigma}_\alpha = \mathbb{C}_\alpha \left[\bar{\boldsymbol{\varepsilon}}_\alpha\right]$.

The average matrix strain $\boldsymbol{\varepsilon}_\mathrm{M}$, i.e., average matrix strain over all UD domain matrix phases, can be computed as $\boldsymbol{\varepsilon}_\mathrm{M} = \mathbb{A}_\mathrm{M} \left[\bar{\boldsymbol{\varepsilon}}\right]$ using the average matrix strain localization tensor

$$\mathbb{A}_\mathrm{M} = \frac{1}{1 - c_\mathrm{F}} \left(\mathbb{I}^\mathrm{S} - c_\mathrm{F} \left\langle \mathbb{A}_\alpha \right\rangle_{\mathrm{F},\alpha} \right) . \tag{5.9}$$

5.3.2 Resolving the microstructure

In order to apply analytical homogenization schemes like the one introduced above, it is necessary to analytically or numerically resolve the microstructure of the given composite material. For the SFRC materials addressed in this work this is typically either done via closed-form orientation-averaging using orientation tensors (Advani and Tucker III,

1987) or by numerically integrating over the fiber orientation distribution function (Pierard et al., 2004; Kammoun et al., 2011; Goldberg et al., 2017; Hessman et al., 2021). As the models proposed here require the damage state of each family of fibers to be tracked separately, only the latter approach is applicable.

To increase the accuracy of the required numerical integration scheme, the adaptive integration scheme of Goldberg et al. (2017) is used. It resorts to a transformation function

$$\boldsymbol{t}(\boldsymbol{p}) = \frac{\boldsymbol{B}^{-\frac{1}{2}}\boldsymbol{p}}{\|\boldsymbol{B}^{-\frac{1}{2}}\boldsymbol{p}\|} \tag{5.10}$$

that yields orientation-adapted integration points $\boldsymbol{t}(\boldsymbol{p})$ from a previously quasi-uniform set of integration points $\boldsymbol{p}$ on the unit sphere, thereby reducing the error and increasing the efficiency. The parameter tensor $\boldsymbol{B}$ of the associated angular central gaussian (ACG) distribution (cf. Goldberg et al., 2017) can be obtained from the second-order orientation tensor $\boldsymbol{N}$ (Montgomery-Smith et al., 2011b; Goldberg et al., 2017; Hessman et al., 2021). Details on this method, as well as comparisons to other approaches can be found in Hessman et al. (2021)[10].

Throughout this work the adaptive integration scheme was used with 25 Lebedev integration points (Lebedev, 1976), while taking advantage of the symmetry of the orientation distribution function (cf. Hessman et al., 2021, [11]). The mean fiber length and diameter from Table 5.1 yield a mean fiber aspect ratio of approximately 27 and the fiber mass fractions of the different composite grades can be easily converted to the fiber volume fractions required in the model, with the resulting values also being shown in Table 5.1 above.

[10] cf. Chapter 4 of this thesis
[11] cf. Chapter 4 of this thesis

5.4 Fiber damage model

In this paper a unified approach to modeling the effective fiber damage is used, which does not distinguish between fiber fracture, fiber/matrix debonding and matrix damage in the direct vicinity of the fiber. The reasoning behind this is that a) a fiber's ability to reinforce the composite material is reduced by all of the three mentioned damage mechanisms and that b) research has shown that while some composite grades show an increased tendency for fiber fracture or fiber/matrix debonding (e.g., Rolland et al., 2018), others may exhibit stronger fiber interfaces and hence increased matrix cracking close to fibers (Belmonte et al., 2017a;b). As it is often not possible to conduct extensive micromechanical analyses similar to those mentioned above in order to quantify the exact shares of each damage type, the simplified approach suggested here offers a pragmatic solution which nevertheless accounts for the material type's specific microstructure. Consequently, and for the sake of brevity, the mentioned damage processes are often simply referred to as *fiber* damage hereafter.

5.4.1 Model equations

An isotropic damage law is introduced, in which the damaged fiber domain is replaced by an equivalent undamaged fiber with a reduced effective stiffness (Fitoussi et al., 1996; Lenz and Mahnken, 2019; 2023) of

$$\mathbb{C}_\alpha = (1 - d_\alpha)\mathbb{C}_\mathrm{F}^0. \tag{5.11}$$

Here, $\mathbb{C}_\mathrm{F}^0$ is the undamaged isotropic stiffness of the fiber and d_α is the fiber's scalar damage parameter.

To account for the presence of multiple fibers of the same orientation and length – all of which are modeled using a single representative fiber phase with index α – a Weibull-type formulation is chosen (cf. Fitoussi

et al., 1996). Thereby, the statistical nature of the fracture strength and fiber-interface strengths of the fibers is taken into account. The overall damage parameter of the fiber ensemble can then be calculated by

$$d_\alpha = d_\mathrm{F}(f_\alpha) = D_\mathrm{F}^\mathrm{max} \left(1 - \exp\left[-\left(\frac{f_\alpha}{f_0}\right)^{k_\mathrm{F}}\right]\right), \tag{5.12}$$

where f_α is the damage-driving history variable, f_0 is the Weibull scale parameter (set to one within the given context), and k_F is the Weibull shape parameter. $D_\mathrm{F}^\mathrm{max}$ can be used to set the maximum value of fiber damage and was set to 0.5 throughout this work. The reasoning behind this is that after initial fiber damage occurs, progressive fracture of the matrix and – finally – of the entire composite dominate the overall material degradation, limiting further fiber damage growth, i.e., up to a fully damaged state. This notion is supported by results from Rolland et al. (2018), where matrix microcracks were shown to initiate near highly stressed fiber damage regions (especially fiber failure) and coalesce into mesocracks, while other fiber regions show lower levels of damage.

Within the given approach, fiber damage is driven by a dimensionless effective scalar fiber loading function $f_\mathrm{F}(\boldsymbol{\sigma}_\alpha)$, which is computed using a Tsai-Wu-type loading function (Tsai and Wu, 1971) in order to account for the anisotropic and pressure-dependent damage behavior observed for fiber and fiber-interface damage (Sato et al., 1991). The related history variable f_α in Eq. (5.12) is computed as $f_\alpha = \max_{\tau\in[0;t]} f_\mathrm{F}(\boldsymbol{\sigma}_\alpha(\tau))$, where τ is a time variable defined in the time interval up to the current time t. Due to the fiber's isotropic material and spheroidal shape, the transversely isotropic variant of the Tsai-Wu criterion (e-Xstream engineering,

2020)

$$f_{\mathrm{F}}(\hat{\sigma}_{ij}) = \frac{\hat{\sigma}_{11}^2}{X_t X_c} + \frac{\hat{\sigma}_{22}^2 + \hat{\sigma}_{33}^2}{Y_t Y_c} + \frac{\hat{\sigma}_{12}^2 + \hat{\sigma}_{13}^2}{S^2} + \frac{4\hat{\sigma}_{23}^2}{Y_t Y_c} - \frac{\hat{\sigma}_{11}\hat{\sigma}_{22} + \hat{\sigma}_{11}\hat{\sigma}_{33}}{2Y_t Y_c} - \frac{2\hat{\sigma}_{22}\hat{\sigma}_{33}}{Y_t Y_c} + \left(\frac{1}{X_t} - \frac{1}{X_c}\right)\hat{\sigma}_{11} + \left(\frac{1}{Y_t} - \frac{1}{Y_c}\right)(\hat{\sigma}_{22} + \hat{\sigma}_{33}) \tag{5.13}$$

can be used, where the components $\hat{\sigma}_{ij}$ of the stress tensor are evaluated with respect to a coordinate system whose x_1 axis is aligned with the current fiber's main axis. The coefficients are the strength under axial tension and compression (X_t and X_c), the strength for transverse tension and compression (Y_t and Y_c) and the shear strength (S). Due to the lack of compression tests, the axial and transverse compression strength parameters were assumed as $X_c = 2X_t$ and $Y_c = 2Y_t$.

For reference, this formulation of the Tsai-Wu model can be obtained from the original equation for transversely isotropic materials (Tsai and Wu, 1971, Eq. 54) by setting the parameters

$$\begin{aligned} F_1 &= (X_t)^{-1} - (X_c)^{-1}, & F_{12} &= -(4X_t X_c)^{-1}, \\ F_2 &= (Y_t)^{-1} - (Y_c)^{-1}, & F_{23} &= -(Y_t Y_c)^{-1}, \\ F_{11} &= (X_t X_c)^{-1}, & F_{66} &= S^{-2}. \\ F_{22} &= (Y_t Y_c)^{-1}, \end{aligned} \tag{5.14}$$

It is important to note that while the loading function in Eq. (5.13) is anisotropic in nature, the damage variable itself is scalar and the resulting damage effect is isotropic. While this does not account for fiber-related *anisotropic* damage effects in the real composite, it remains a legitimate tradeoff within the given modeling framework and with regard to computational efficiency.

It is also worth noting that the Tsai-Hill loading function, which does not distinguish between tension and compression states, has been applied to

the failure and damage modeling of SFRCs in works such as Kammoun et al. (2011) and Kaiser and Stommel (2012). Unlike the model proposed here, both publications applied the loading functions on the composite level, or – more specifically – the pseudo-grain level of the Two-Step homogenization model, and not for computing the damage of the fiber phase as proposed here.

Variations of this model have been published by Fitoussi et al. (1996; 1998) and Schemmann et al. (2018), among others. They apply a Coulomb-type loading function to model interfacial decohesion on each surface element of each fiber. Furthermore, Böhlke and Othmani (2013) applied a similar approach to modeling the failure of silicone nitride. Naturally, such models allow for more detailed insight into the specific damage processes at the microscale. Nevertheless, the chosen Tsai-Wu-based approach offers clear advantages with respect to the computational effort of evaluating the fiber loading while retaining most of the micromechanical modeling accuracy needed for the macroscopic material behavior. This is supported by the fact, that the underlying mean field schemes only offer *average* values of the inclusion (and hence fiber) stresses and strains anyway.

5.4.2 Parameter identification

To identify the model parameters for the fiber damage model introduced in Section 5.4 an inverse identification process based on the quasi-static tensile tests from Section 5.2.3 was chosen (cf. Kabir et al., 2006). More specifically, a fully automated computation workflow was implemented using the *optiSLang* (DYNARDO GmbH) software to run repeated finite element analyses of the tensile specimens. The employed modeling setup is shown in Fig. 5.7 and included the layer-wise fiber orientation tensor information outlined in Section 5.2.2 and evaluated at nine distinct layers, which has proven to be a good compromise of computation efficiency and accuracy with respect to resolving the fiber orientation distribution

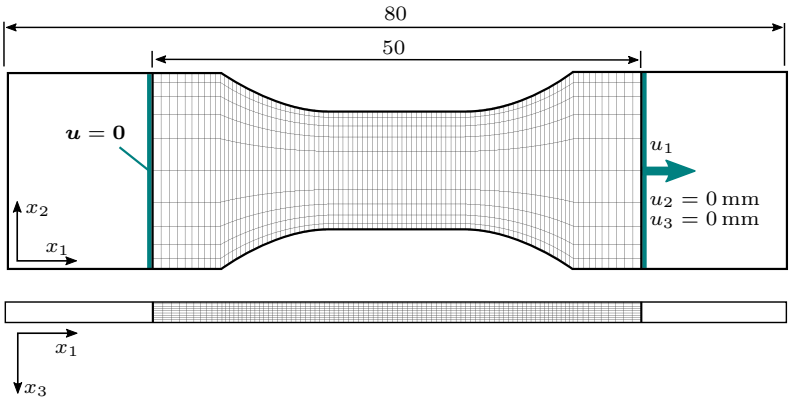

Figure 5.7: Outline of the finite element model used for simulating the tensile tests, showing the part of the specimen geometry included for modeling purposes (units in mm). The mesh consists of nine layers and a total of 8640 linear hexahedron elements.

(cf. Hessman et al., 2021, [12]). Each layer-specific fiber orientation tensor was resolved using 25 Lebedev quadrature points on the hemisphere (details regarding the integration scheme can be found in Hessman et al. (2021)[13]). The matrix and fiber material properties are summarized in Table 5.1. Within each optimization iteration all five loading angles were computed and the resulting nominal stress-strain curves were compared to the experimental results. As the fiber damage model is only meant to account for the initial damage close to the fibers and early fiber breakage, the simulated and measured curves were only compared up to a stress of $2/3$ of the ultimate tensile stress in the experiments. At larger strains the damage is gradually dominated by matrix cracking between fibers (Sato et al., 1991) and large-scale debonding of fibers at the scale of the specimen (Rolland et al., 2016). The optimization problem was then formulated to minimize the root mean squared deviation of the two

[12] cf. Chapter 4 of this thesis
[13] cf. Chapter 4 of this thesis

stress curves by adapting the fiber damage model parameters X_t, Y_t, S and k_F (cf. Section 5.4).

The optimal parameter set was found to be $X_t = 960.5\,\mathrm{MPa}$, $Y_t = 109.8\,\mathrm{MPa}$, $S = 194.2\,\mathrm{MPa}$ and $k_\mathrm{F} = 1.64$ for which the final curves are shown in Fig. 5.8. These strength values obtained for the fiber domain are considerably lower than the typical strength of the glass fiber itself, which lies above $3\,\mathrm{GPa}$ (Wallenberger and Bingham, 2010). This is explained by the fact that the model is set up to account for both fiber breakage and also other fiber-related damage mechanisms such as fiber tip debonding, fiber-matrix debonding and matrix microcracks close to the fiber surface (cf. Rolland et al., 2016). The latter mechanisms can be reasonably assumed to occur at lower stresses than the glass fiber material strength and lead to the presented lower strength values. This highlights the important notion, that the models' strength parameters represent heuristic parameters that cannot be directly obtained from physical material properties such as material or interfacial strength values. As such, they have to be identified inversely for every material, as presented in this work.

The average fiber damage $\bar{d}_\mathrm{F} = \langle d_\alpha \rangle_{\mathrm{F},\alpha}$ (cf. Eq. (5.3)) at the end of the presented curves (up to 2/3 ultimate tensile strength) was found to be between $23\,\%$ for the $0°$ test and $28\,\%$ for the $90°$ test.

5.5 Matrix fatigue damage model

In this section the matrix fatigue damage model is introduced. First, the model equations are derived in the time domain before cycle-based formulations are introduced and benchmarked. Then the model's implementation into the commercial finite-element solver *Abaqus* (Dassault Systèmes SE, France) is covered and the model parameter sensitivities are studied. Finally, the identification of the model parameters based on

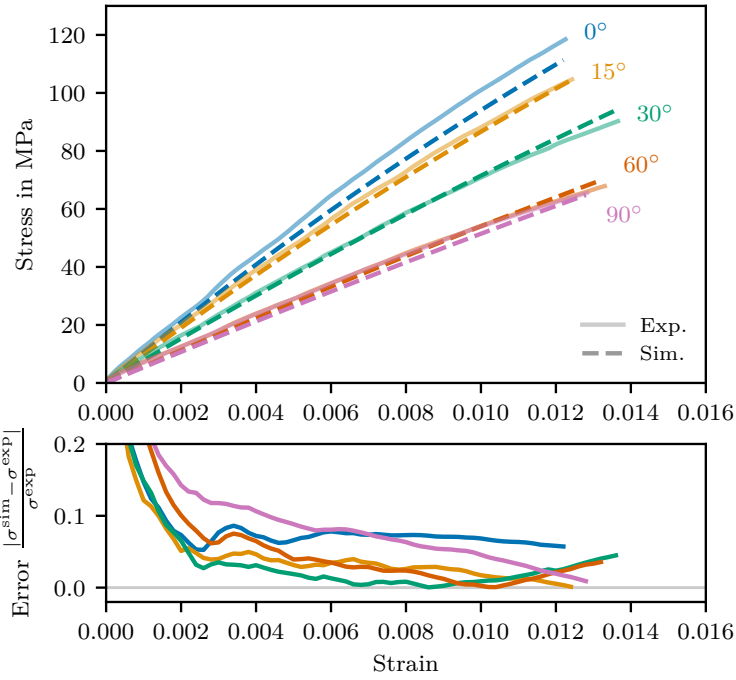

Figure 5.8: Plot showing the stress-strain curves for the five specimen orientations from the tensile tests and the corresponding simulated curves using the newly identified fiber damage model. All curves were truncated at the strain corresponding to an experimental stress value of 2/3 of the ultimate tensile stress for any given orientation. The second plot shows the relative error between simulated and measured curves.

the experimental data and the final results of the simulation campaign are discussed.

5.5.1 Model equations

The progressive damage in the matrix phase is modeled using an isotropic linear-elastic continuum damage approach (Chaboche, 1988; Lemaitre and Chaboche, 1990; Kammoun et al., 2015; Schemmann et al., 2018). To this end, a scalar matrix damage parameter d_{M} is introduced, which takes values between zero in the initial state, and one for a fully damaged material. From this, the effective matrix stiffness tensor of the damaged material can be computed from the undamaged matrix material ($\mathbb{C}^0_{\mathrm{M}}$)

$$\mathbb{C}_{\mathrm{M}} = (1 - d_{\mathrm{M}})\, \mathbb{C}^0_{\mathrm{M}}. \tag{5.15}$$

The cyclic matrix damage model and the related equations proposed in this work are based on the work of Peerlings et al. (Peerlings, 1999; Peerlings et al., 2000), who derive evolution equations for the damage parameter and introduce time- and cycle-based numerical schemes.

The driving force of the matrix damage variable is given in the dimensionless form used in Peerlings (1999):

$$Y = \sqrt{\frac{1}{E^0}\, \boldsymbol{\varepsilon}_{\mathrm{M}} \cdot \mathbb{C}^0_{\mathrm{M}}\, [\boldsymbol{\varepsilon}_{\mathrm{M}}]}, \tag{5.16}$$

where E^0 is a normalizing constant.

Following the work of Peerlings et al. (2000), we define a damage loading function $f = Y - Y_c$ such that damage only increases when the threshold parameter Y_c is exceeded ($f \geq 0$) and the rate of f is non-negative ($\dot{f} \geq 0$), meaning that unloading ($\dot{f} < 0$) does not lead to damage progression.

Peerlings et al. (2000) then define the rate of the damage variable as

$$\dot{d}_{\mathrm{M}} = \begin{cases} g(Y, d_{\mathrm{M}})\dot{Y} & \text{if} \quad f \geq 0 \text{ and } \dot{f} \geq 0 \text{ and } d_{\mathrm{M}} < 1 \\ 0 & \text{else.} \end{cases} \tag{5.17}$$

Hence, the rate of matrix damage is proportional to the rate of the driving force and to the so-called evolution function $g(Y, d_{\mathrm{M}})$. Peerlings et al. (2000) suggest the following formulation

$$g(Y, d_{\mathrm{M}}) = C \, \exp\left(\alpha d_{\mathrm{M}}\right) \, Y^{\beta}. \tag{5.18}$$

Here, the main parameters of the matrix damage law are introduced: the factor C, the damage factor α, and the loading exponent β.

It is important to mention that the original publication of Peerlings et al. (2000) formulate their damage law using macroscopic quantities and in the context of a homogeneous material (i.e., steel). In order to account for the influence of fiber damage on the local loading of the matrix material in SFRCs we suggest a novel and material-specific modification of the damage rate function:

$$g(Y, d_{\mathrm{M}}) = C \, \exp\left(\alpha \left(d_{\mathrm{M}} + \gamma \, c_{\mathrm{F}} \, \bar{d}_{\mathrm{F}}\right)\right) \, Y^{\beta}. \tag{5.19}$$

Thereby, the mean matrix damage d_{M} in Eq. (5.18) is substituted with the term $d_{\mathrm{M}} + \gamma \, c_{\mathrm{F}} \, \bar{d}_{\mathrm{F}}$ where $\bar{d}_{\mathrm{F}} = \langle d_{\alpha} \rangle_{\mathrm{F},\alpha}$ is the volume-weighted mean fiber damage and γ shall be referred to as the *fiber damage interaction parameter*.

This micromechanically motivated modification stems from the observation that damage effects localized at or in the direct vicinity of the fiber – such as cavitation, microcracks, debonding and fiber fracture – lead to additional stress concentrations in the matrix and facilitate the initiation, growth and progression of mesoscopic matrix cracks (Rolland et al., 2018; Belmonte et al., 2017a). Furthermore, this effect becomes more

pronounced with an increased fiber fraction, as this implies a higher density of fiber-related damage regions. In mathematical terms this is expressed by the fact that, as the average fiber damage (meaning fiber and fiber-interface damage as explained in Section 5.4) $\bar{d}_{\mathrm{F}}$ increases, the exponential term in the evolution function in Eq. (5.19) will increase the matrix damage rate in Eq. (5.17). Without such an interaction, the average matrix stress state obtained from mean field schemes would lead to unrealistically low rates of damage. Further details on why this modification is needed in the context of SFRCs[14] are given further below in Section 5.5.8.

In order to then compute the matrix damage for each time increment within a numerical study, we can write (Peerlings et al., 2000)

$$d_{\mathrm{M}}(t^{n+1}) = d_{\mathrm{M}}(t^{n}) + \int_{\tau=t^{n}}^{t^{n+1}} \dot{d}_{\mathrm{M}} \, \mathrm{d}\tau. \tag{5.20}$$

As noted by (Peerlings et al., 2000), one needs to ensure that the temporal resolution is chosen to be sufficiently small, such that each cycle within a cyclic loading scenario is accurately resolved.

5.5.2 Cycle-based formulation

While computing the above integral in time-domain may be possible within the context of low cycle fatigue, it becomes unfeasible for high cycle fatigue (Peerlings et al., 2000). Therefore – again following Peerlings et al. (2000) – this section covers a cycle-based formulation. While the equations in the above-mentioned publication were given for the example of fully-reversed loading ($R_F = -1$), we will establish equations that cover all possible loading scenarios.

[14] The original paper erroneously used the acronym “SFRPs”, thereby referring to short fiber reinforced polymer.

Let us start by restructuring Eq. (5.20) in terms of cycles $N \in \{0, 1, \ldots\}$ and cycle increments ΔN:

$$d_{\mathrm{M}}\left(t^{N+\Delta N}\right) = d_{\mathrm{M}}\left(t^{N}\right) + \sum_{n=N}^{N+\Delta N-1} \int_{\tau=t^n}^{t^{n+1}} \dot{d}_{\mathrm{M}}\, \mathrm{d}\tau. \tag{5.21}$$

Next, we will try to eliminate the integral over time above by directly integrating over the driving force. For the following derivations, we will introduce the lower driving force $Y_{lo} = Y(\boldsymbol{\varepsilon}_{\mathrm{M,min}})$ and the upper driving force $Y_{up} = Y(\boldsymbol{\varepsilon}_{\mathrm{M,max}})$ of a cycle as the driving forces associated with the matrix strain at the lower (minimum) and upper (maximum) levels of the current local cyclic loading state (see more details on this in Section 5.5.5). Due to the formulation of the driving force, this does not necessarily mean that Y_{lo} is smaller than Y_{up}. This notion is highlighted by the examples in Fig. 5.9, where a single cycle is plotted for three simplified uniaxial load cases of an arbitrary example material. In the first case (pure tension), the driving force increases from Y_{lo} to Y_{up} before decreasing back down to Y_{lo} ($Y_{up} > Y_{lo}$). Within each cycle only the region marked in red is associated with a positive damage rate as both $f \geq 0$ and $\dot{f} \geq 0$. In the second case (pure compression) the limit driving forces are flipped as the lower driving force Y_{lo} corresponding to the smaller (i.e., negative) strain is actually larger than the upper driving force: $Y_{lo} > Y_{up}$. The third case (tension/compression) is a combination of the first two and yields two regions of positive damage rates: one associated with the driving force increasing from Y_c to Y_{up} while the strain increases to the upper limit and one in which the driving force increases from Y_c to Y_{lo} in conjunction with the strain decreasing to the lower limit.

To now further simplify the integral in Eq. (5.21) we will restructure the equation explicitly considering only the above-mentioned regions of positive damage rate, thereby dropping the distinction of cases in

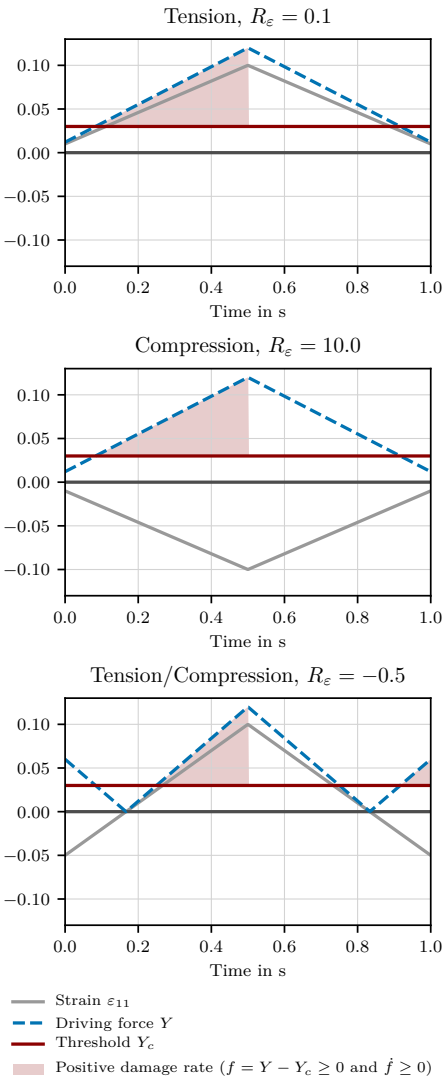

Figure 5.9: Schematic of the relationship between uniaxial strain ε_{11}, resulting driving force Y and the damage-driving part of Y (red area) for three uniaxial example load cases: pure tension, pure compression and tension/compression.

Eq. (5.17). This furthermore allows us to facilitate the substitution $\dot{Y}\,\mathrm{d}t = \mathrm{d}Y$, avoiding integrating over time (Peerlings et al., 2000). Combining these steps we arrive with the following equation, depending on the load case: Tension (hereafter abbreviated as "T") for which $R_F \in [0, 1)$, compression ("C") with $R_F = -\infty \vee R_F > 1$ or tension/compression ("T/C") in case of $R_F \in (-\infty, 0)$.

$$
\begin{aligned}
d_{\mathrm{M}}^{N+\Delta N} &= d_{\mathrm{M}}^{N} + \sum_{n=N}^{N+\Delta N-1} \begin{cases} \displaystyle\int_{Y=\max(Y_c,Y_{lo}^n)}^{\max(Y_c,Y_{up}^n)} g\left(Y, d_{\mathrm{M}}\right) \mathrm{d}Y & \mathrm{T} \\ \displaystyle\int_{Y=\max(Y_c,Y_{up}^n)}^{\max(Y_c,Y_{lo}^n)} g\left(Y, d_{\mathrm{M}}\right) \mathrm{d}Y & \mathrm{C} \\ \displaystyle\int_{Y=Y_c}^{\max(Y_c,Y_{lo}^n)} g\left(Y, d_{\mathrm{M}}\right) \mathrm{d}Y + \int_{Y=Y_c}^{\max(Y_c,Y_{up}^n)} g\left(Y, d_{\mathrm{M}}\right) \mathrm{d}Y & \mathrm{T/C} \end{cases} \\
&= d_{\mathrm{M}}^{N} + \sum_{n=N}^{N+\Delta N-1} \begin{cases} H(\max(Y_c, Y_{lo}), \max(Y_c, Y_{up}), d_{\mathrm{M}}) & \mathrm{T} \\ H(\max(Y_c, Y_{up}), \max(Y_c, Y_{lo}), d_{\mathrm{M}}) & \mathrm{C} \\ H(Y_c, \max(Y_c, Y_{lo}), d_{\mathrm{M}}) + H(Y_c, \max(Y_c, Y_{up}), d_{\mathrm{M}}) & \mathrm{T/C} \end{cases}
\end{aligned}
\tag{5.22}
$$

The function $H(Y_1, Y_2, d_\mathrm{M})$ is introduced to make the equations more compact and is defined by

$$\begin{aligned} H(Y_1, Y_2, d_\mathrm{M}) &:= \int_{Y=Y_1}^{Y_2} g\left(Y, d_\mathrm{M}\right) \,\mathrm{d}Y \\ &= \frac{1}{\beta+1} C \,\exp\left(\alpha\left(d_\mathrm{M} + \gamma\, c_\mathrm{F}\, \bar{d}_\mathrm{F}\right)\right)\, Y^{\beta+1}\Big|_{Y_1}^{Y_2} \\ &= \frac{1}{\beta+1} g(Y, d_\mathrm{M}) Y\Big|_{Y_1}^{Y_2} \end{aligned} \tag{5.23}$$

where we also make use of the notion that the matrix damage d_M changes relatively slowly during one cycle as compared to the matrix strain, driving function and damage rate (Peerlings et al., 2000).

The cycle-based formulation in Eq. (5.21) with the transformations in Eq. (5.22) and Eq. (5.23) above reduces the computational effort considerably when compared to the time-based equations in Section 5.5.1. Nevertheless, computing each cycle within each element remains a computationally expensive task for real-world parts and for load cases with many millions of cycles to failure. Therefore, Peerlings (1999) suggest an approach where the above equations are only evaluated at selected cycles with a cycle increment ΔN between them. More specifically, the damage at cycle $N + \Delta N$ can be computed using the trapezoidal integration rule

$$\begin{aligned} d_\mathrm{M}^{N+\Delta N} = d_\mathrm{M}^{N} + \frac{\Delta N}{2}\Bigg(& G\left(Y_{lo}^{N}, Y_{up}^{N}, d_\mathrm{M}^{N}\right) \\ & + G\left(Y_{lo}^{N+\Delta N}, Y_{up}^{N+\Delta N}, d_\mathrm{M}^{N+\Delta N}\right)\Bigg), \end{aligned} \tag{5.24}$$

where the function $G\left(Y_{lo}, Y_{up}, d_{\mathrm{M}}\right)$ distinguishes the load cases as outlined in Eq. (5.22)

$$G\left(Y_{lo}, Y_{up}, d_{\mathrm{M}}\right) := \begin{cases} H(\max(Y_c, Y_{lo}), \max(Y_c, Y_{up}), d_{\mathrm{M}}) & \mathrm{T} \\ H(\max(Y_c, Y_{up}), \max(Y_c, Y_{lo}), d_{\mathrm{M}}) & \mathrm{C} \\ H(Y_c, \max(Y_c, Y_{lo}), d_{\mathrm{M}}) & \\ + H(Y_c, \max(Y_c, Y_{up}), d_{\mathrm{M}}) & \mathrm{T/C}. \end{cases} \tag{5.25}$$

The Newton-Raphson method is then used to solve the implicit problem in Eq. (5.24) for the matrix damage $d_{\mathrm{M}}^{N+\Delta N}$ at the end of the cycle increment.

While the time-based scheme yields a computational cost proportional to the number of cycles to failure, with the cycle-based formulation the computational cost becomes decoupled from the number of cycles, as the cycle increment ΔN can be chosen in such a way that it is as large as possible and as small as numerically necessary.

5.5.3 Comparison of time- and cycle-based approaches

Here we present a brief comparison of the time- and cycle-based model equations, highlighting the numerical benefits of the latter and quantifying the error over time. The comparison is performed for a single integration point within a uniaxial loading setup. The stress equilibrium is solved for using a Newton-Raphson-based solver implemented in *Python*. Furthermore, the average microstructural properties of the PA66-GF35 composite are used, as summarized in Hessman et al. (2019)[15]. For simplicity, only the matrix fatigue damage law is considered and the parameters were set to $C = 20$, $\alpha = 5$, $\beta = 8$ and $Y_c = 0$.

[15] cf. Chapter 3 of this thesis

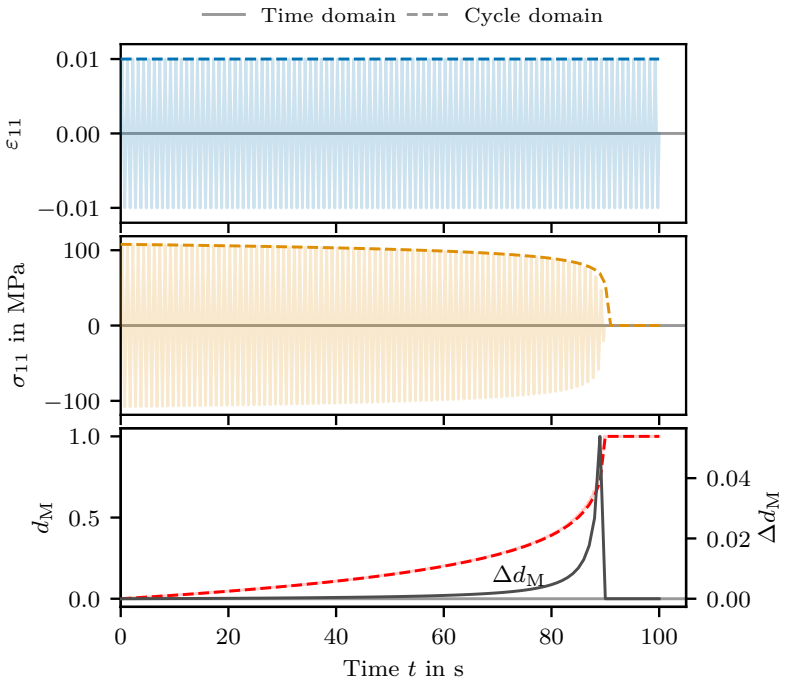

Figure 5.10: Results of the comparison of time and cycle-based matrix damage models from uniaxial single-element benchmark computations. Benchmark 1: constant strain amplitude.

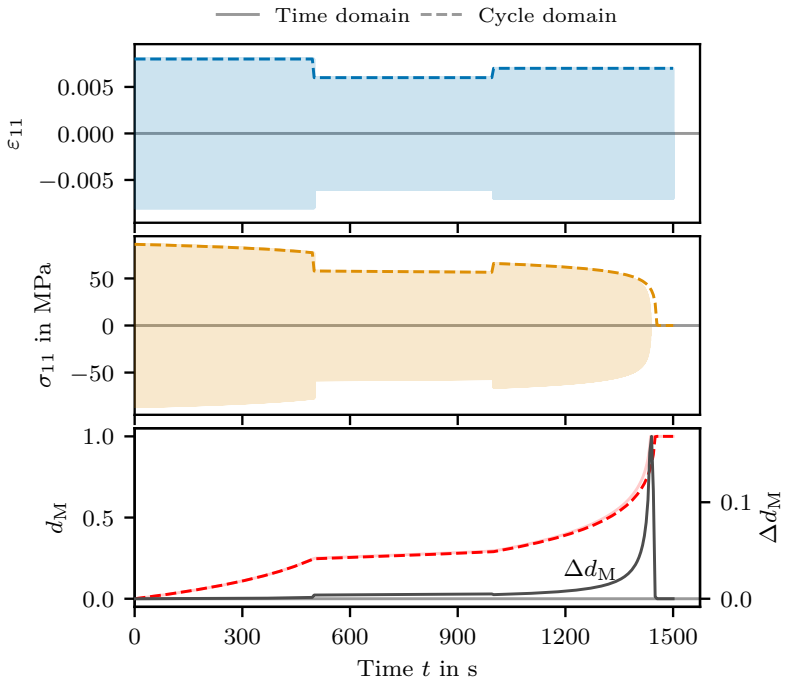

Figure 5.11: Results of the comparison of time and cycle-based matrix damage models from uniaxial single-element benchmark computations. Benchmark 2: three amplitude levels.

In a first comparison of the two approaches, the material is subjected to 100 cycles of constant amplitude strain loading with a load ratio of $R_\varepsilon = \varepsilon_{\min}/\varepsilon_{\max} = -1$ and a loading frequency of $1\,\mathrm{Hz}$. A constant cycle-increment of $\Delta N = 1$ was chosen for the cycle-based approach. Reviewing the results (Fig. 5.10), we see that the evolution of d_M is recovered very well by the cycle-based model with the deviation Δd_M lying below $1\,\%$ for most of the duration and reaching a maximum just below $6\,\%$ at failure. Accordingly, the calculated stress values and the time of failure also accurately match those of the time-based reference.

For the second comparison a more complex strain profile was used, consisting of three amplitudes of $0.8\,\%$, $0.6\,\%$ and $0.7\,\%$ and 500 cycles each. A larger cycle increment of $\Delta N = 5$ was used. The results in Fig. 5.11 show that the damage and stress evolution match well, the deviations remaining small and below $1\,\%$ up until the final cycles before failure. This highlights the model's ability to accurately model the damage evolution over a larger duration, including varying amplitudes and using larger cycle increments while requiring significantly lower computation times.

5.5.4 Parameter sensitivity study

Apart from the well-known elastic matrix material properties, the damage model is mainly governed by three parameters: C, α and β (cf. Equations (5.18) and (5.19)). In this section the influence of these parameters on the evolution of the damage variable and on the resulting S-N curves is studied. For this, a base parameter set of $C = 20$, $\alpha = 5$ and $\beta = 8$ is defined. Furthermore, single-element computations are used based on the average PA66-GF35 microstructure given in Hessman et al. (2019)[16].

In a first step, S-N curves for three values are computed to study the influence of parameter C, each curve consisting of multiple stress-controlled

[16] cf. Chapter 3 of this thesis

constant-amplitude $R_\sigma = -1$ computations up to failure. The curves – shown in Fig. 5.12 – demonstrate that the parameter leads to a parallel shift of the S-N curves. In other words, the cycles to failure decrease as the value of C is increased, whereas the slope of the S-N curve remains constant.

An increase of the exponent β, on the other hand, leads to S-N curves that become less steep and which are shifted to higher stresses and cycles, respectively (cf. Fig. 5.13). This means that larger values of β increase the model's sensitivity to the matrix loading parameter Y and hence the material load or loading amplitude.

Lastly, the parameter α controls the damage rate amplifying effect of the matrix damage. In other words, larger values of α lead to the material more quickly degrading once damage occurs. This effect is highlighted in Fig. 5.14 where the resulting stress amplitudes for constant strain amplitude loading with $R_\epsilon = -1$ and four different values of α are shown. At first the initial curves nearly coincide. Then, after some initial damage is encountered and the stress amplitude drops as a consequence, the high-α curves drop more quickly to zero as the matrix damage also increases more quickly. Conversely, for low values of α the material degradation does not accelerate as quickly, even for larger matrix damage levels.

5.5.5 Implementation

The multiscale cyclic damage model proposed in this paper was implemented in Fortran as a *User Defined Material* (UMAT) for the commercial finite element solver Abaqus. The loading condition of the overall part can then be specified in Abaqus and the UMAT is automatically called in each solver iteration and for each integration point. By restricting ourselves to proportional loading, we can use the specified Dirichlet or Neumann boundary conditions of the finite element model such that they represent the loading *amplitude* $(\cdot)_{\mathrm{amp}}$ instead of the minimum

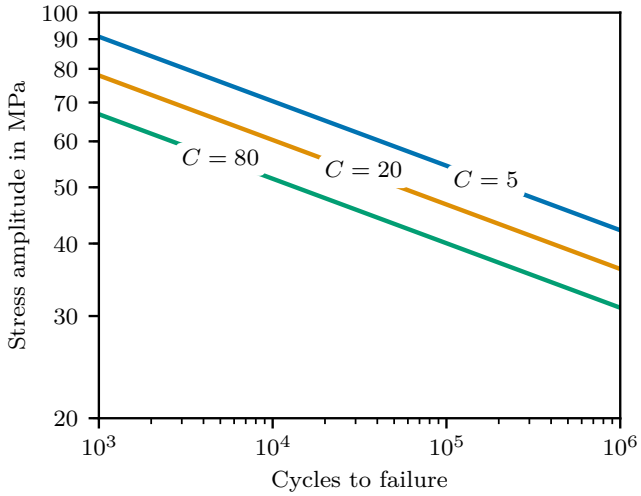

Figure 5.12: S-N curves from the parameter study of C and based on base parameter values $\alpha = 5$ and $\beta = 8$.

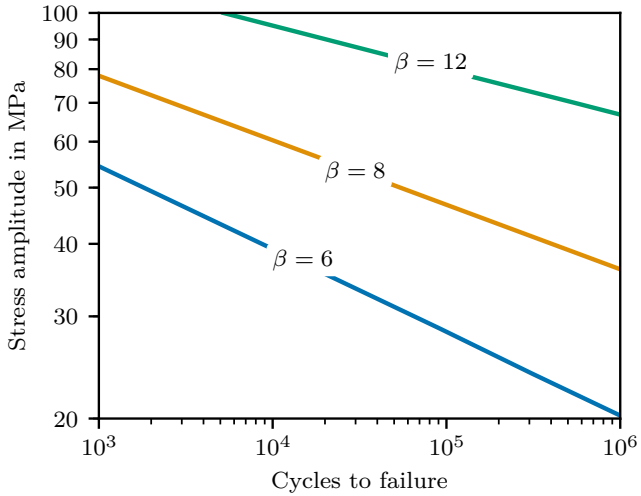

Figure 5.13: S-N curves from the parameter study of β and based on base parameter values $C = 20$ and $\alpha = 5$.

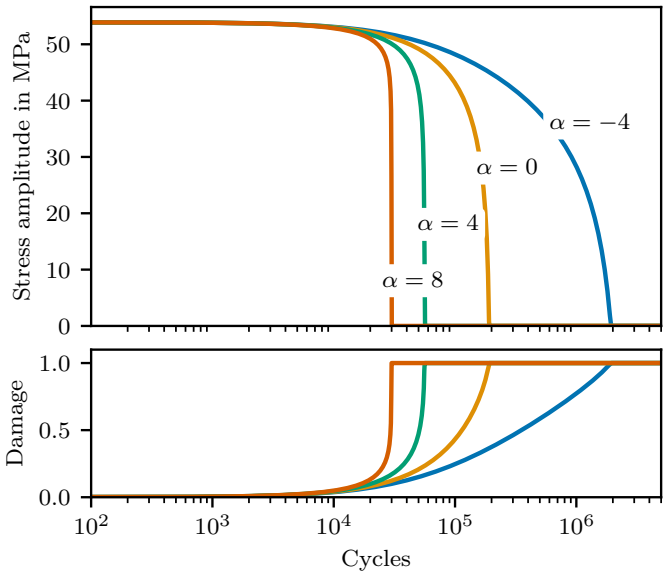

Figure 5.14: Stress amplitude curves from the parameter study of α and based on base parameter values $C = 20$ and $\beta = 8$.

or maximum load of a cycle. This way we can compute both the macroscopic minimum and maximum loading states from the amplitude and load ratio R:

$$\begin{aligned} F_{\min} &= R_F F_{\max} = \frac{2R_F}{1-R_F} F_{\text{amp}} \qquad \text{and} \\ F_{\max} &= \frac{1}{R_F} F_{\min} = \frac{2}{1-R_F} F_{\text{amp}}. \end{aligned} \tag{5.26}$$

In these equations the relationships are given for a cyclic outer force F, but hold equally for any prescribed cyclic displacement boundary conditions.

The composite model parameters are specified as a property vector, including the components of the fiber orientation tensor, fiber volume fraction, elastic properties and strength parameters. The above-mentioned load ratio is also specified within this properties vector. By employing the UEXTERNALDB subroutine in Abaqus it is also possible to specify a different fiber orientation tensor for each element of the mesh where this data is available – e.g., from mold filling simulations. Such a mapping of fiber orientation tensors was not employed in this work as the layer-wise fiber orientation was modeled using separate layers of elements with layer-wise constant fiber orientation tensors.

From a numerical standpoint, the cycle-based trapezoidal scheme from Section 5.5.2 is implemented by using the solver's time-variable as the real-valued cycle indicator. Within each iteration of each pseudo-time increment (i.e., cycle increment), the integration point's minimum and maximum strain at the beginning and at the end of the cycle increment ($\bar{\varepsilon}^{N}_{min/max}$ and $\bar{\varepsilon}^{N+\Delta N}_{min/max}$) are computed from the strain amplitudes at the beginning and at the end of the cycle increment, $\bar{\varepsilon}^{N}_{\text{amp}}$ and $\bar{\varepsilon}^{N+\Delta N}_{\text{amp}} = \bar{\varepsilon}^{N}_{\text{amp}} + \Delta\bar{\varepsilon}^{N+\Delta N}_{\text{amp}}$ respectively. Here we leverage the fact that since the damage variables change slowly within a cycle increment, we can assume the overall finite element model to remain linear. In other words, the minimum/maximum strains at an integration point and

within one cycle increment remain proportional to the macroscopic minimum/maximum loading and we can compute them using the macroscopic load ratio R and the local strain amplitudes (cf. Eq. (5.26)):

$$\begin{aligned} \bar{\boldsymbol{\varepsilon}}_{\mathrm{min}}^{N/N+\Delta N} &= \frac{2R}{1-R}\bar{\boldsymbol{\varepsilon}}_{\mathrm{amp}}^{N/N+\Delta N} \qquad \text{and} \\ \bar{\boldsymbol{\varepsilon}}_{\mathrm{max}}^{N/N+\Delta N} &= \frac{2}{1-R}\bar{\boldsymbol{\varepsilon}}_{\mathrm{amp}}^{N/N+\Delta N} \end{aligned} \tag{5.27}$$

In a next step, the micromechanical model is set up for the current set of damage variables, the damage of each family of fibers is computed and the Newton-Raphson scheme is used to solve for the new matrix damage variable $d_{\mathrm{M}}^{N+\Delta N}$ at the end of the cycle increment. After convergence is achieved, the UMAT returns the updated state variables and the stress *amplitude* tensor at the end of the cycle increment ($N + \Delta N$) to the finite element solver. The full details of the algorithm are shown in Fig. 5.15.

5.5.6 Parameter identification

The model parameters for the matrix fatigue damage model were again obtained by an inverse identification using a similar workflow as described above for the fiber damage model (Section 5.4.2). The finite element model – outlined in Fig. 5.16 – was set up to include the original dog-bone specimen geometry (Specimen B in Fig. 5.1) with the layered fiber orientation tensors of each composite grade and the force (and thus nominal stress) *amplitude* value as a constant load. As the load ratio $R_F = F_{\mathrm{min}}/F_{\mathrm{max}}$ was constant and equal to zero for all tests, this value was set within the property vector of the UMAT. The moment of failure for the simulated fatigue tests was defined as the cycle (i.e., simulation pseudo time) at which the first element reaches a matrix damage parameter value of more than 0.95. The marginal inaccuracy of this definition is legitimized by avoiding the computational cost and mathematical pitfalls of continuing the simulation post localization.

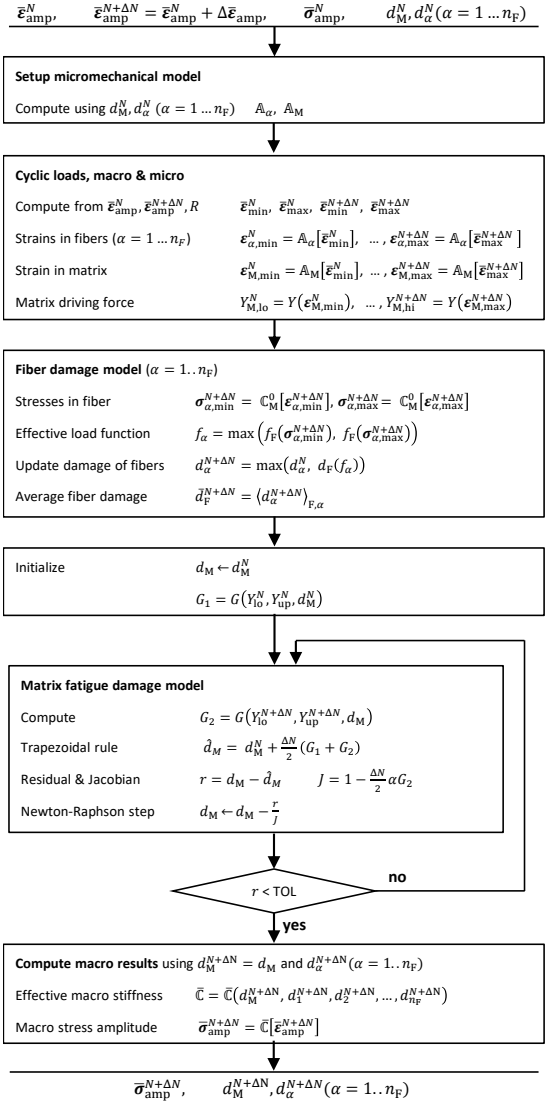

Figure 5.15: Flow chart of the implementation of the entire model as run at each integration point and for each increment. This includes micromechanics, fiber damage and matrix fatigue damage model.

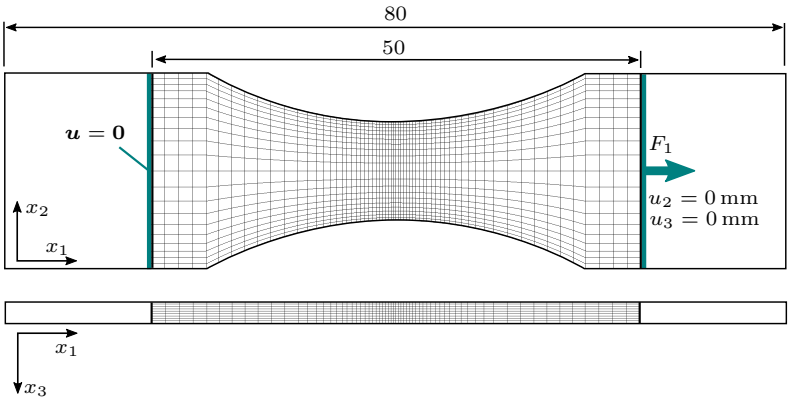

Figure 5.16: Outline of the finite element model used for simulating the fatigue tests, showing the part of the specimen geometry included for modeling purposes (units in mm). The mesh consists of nine layers and 72720 linear hexahedron elements.

More detailed modeling of post-localization damage propagation is often not the focus of industrial applications and not within the scope of this work.

To decouple the identification of the matrix and fiber damage models, only the unreinforced PA66 specimens and tests were employed for fitting the matrix damage parameters. The optimal matrix fatigue damage model parameters (C, α and β) obtained from this process are given in Table 5.3 and will be hereafter referred to as the *no-interact* model in prospect of further results. The resulting S-N curve for the PA66 tests and simulation are shown in Fig. 5.17, highlighting a tight fit between the experimental data (i.e., the regression curve) and the simulation results.

5.5.7 Model validation

A test of the newly fitted matrix fatigue damage model was performed based on simulations of all $90°$ fatigue tests for all composite grades

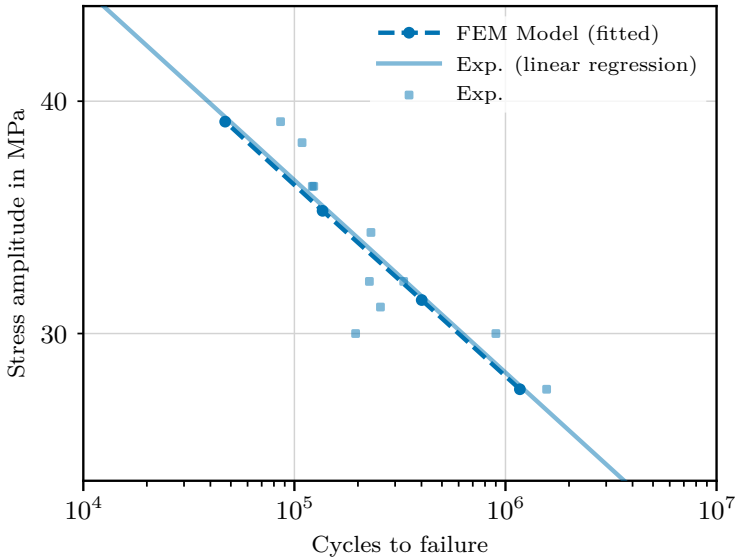

Figure 5.17: Results of the parameter identification process for the matrix fatigue model using the unreinforced PA66 specimens and based on finite element simulations.

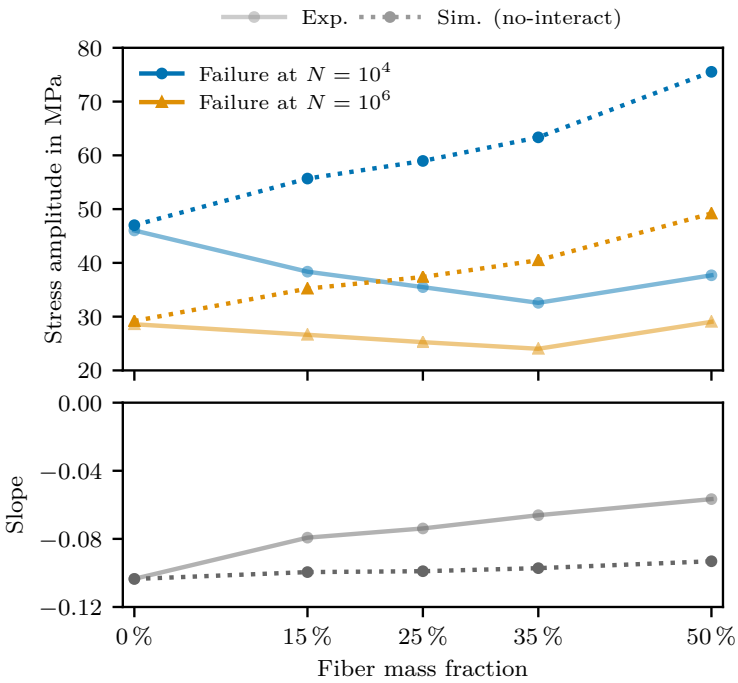

Figure 5.18: Fatigue results for the different 90° composites, including experimental results ("Exp.") and the "no-interact" model fitted using only the matrix material. Simulations were performed on a single-element basis.

introduced in Section 5.2.4. A single-element solver using the mean fiber orientation (cf. Table 5.1) was used, neglecting any geometry-induced stress concentrations. Alongside the matrix fatigue model parameters from above, the previously identified fiber damage parameters from Section 5.4.2 were employed. The results are summarized in Fig. 5.18 using the slope of the log-log S-N curves and stress amplitudes for cycles to failure of $N = 10^4$ and $N = 10^6$. While the experimental results (cf. Section 5.2.4) suggest that the slopes of the S-N curves increase (i.e., becoming more flat) with higher contents of fibers in the composite, the simulation results of the "no-interact" model (dotted lines) underestimate this effect significantly, showing a limited influence of the fiber mass fraction on the slope. In addition, the stress amplitudes for failure at the two selected cycle levels increase instead of decrease for higher fiber mass fractions. Both effects suggest that the given matrix fatigue model – derived purely from unreinforced tests – is not sufficient for modeling the complex dependency of the fatigue behavior on the reinforcing fibers. More specifically, the decreasing material fatigue strength for higher fiber content for the non-aligned tests is not retrieved.

5.5.8 Fatigue model with fiber damage interaction

To improve the model with regards to the shortcomings highlighted above, the model was extended to include a *fiber damage interaction* term – hereafter called the "interact" model. As detailed in Section 5.5.1, this term scales the exponential influence of the current composite damage state on the damage rate by including the product of fiber volume fraction and the average fiber damage in the evolution function (cf. Eq. (5.19)). This modification thereby leads to a higher damage rate and hence reduces the fatigue strength (or lifetime) of the $90°$ specimens, especially at higher fiber fractions and in cases where fibers have already seen damage.

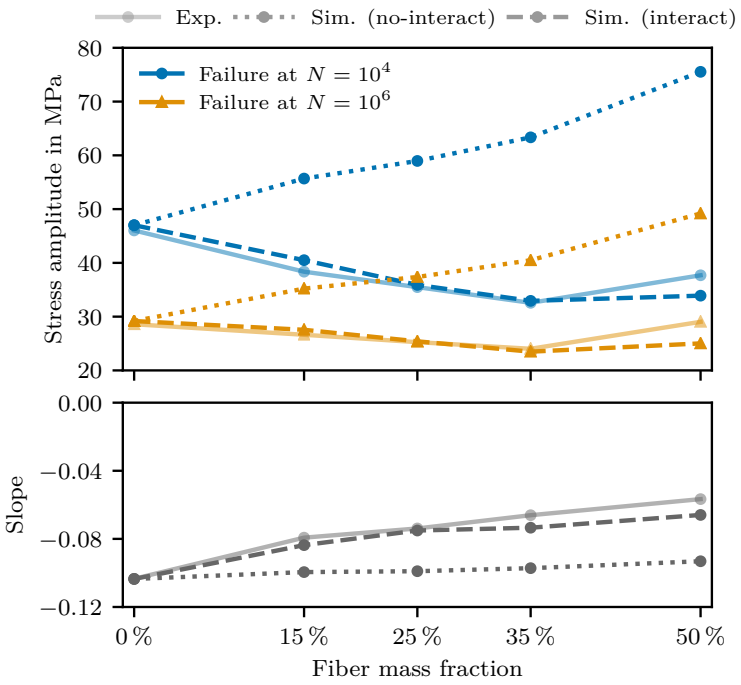

Figure 5.19: Fatigue results for the different 90° composites, including experimental results ("Exp.") and the two models, denoted as "Sim. (no-interact)" and "Sim. (interact)". Simulations were performed on a single-element basis.

The additional *fiber damage interaction parameter* γ can be identified by the same method as for the previous parameters, but based on one arbitrary composite S-N curve. In the present work the PA66-GF35 S-N curve with 90° fiber orientation was used and a fiber damage interaction parameter of $\gamma = 24.5$ was obtained (see also Table 5.3).

To validate the addition to the model and the identified parameter value, single-element computations were employed in the same fashion as in the previous sub-section. The extracted slope and selected fatigue strength values are shown in Fig. 5.19 as dashed lines. Indeed, the new

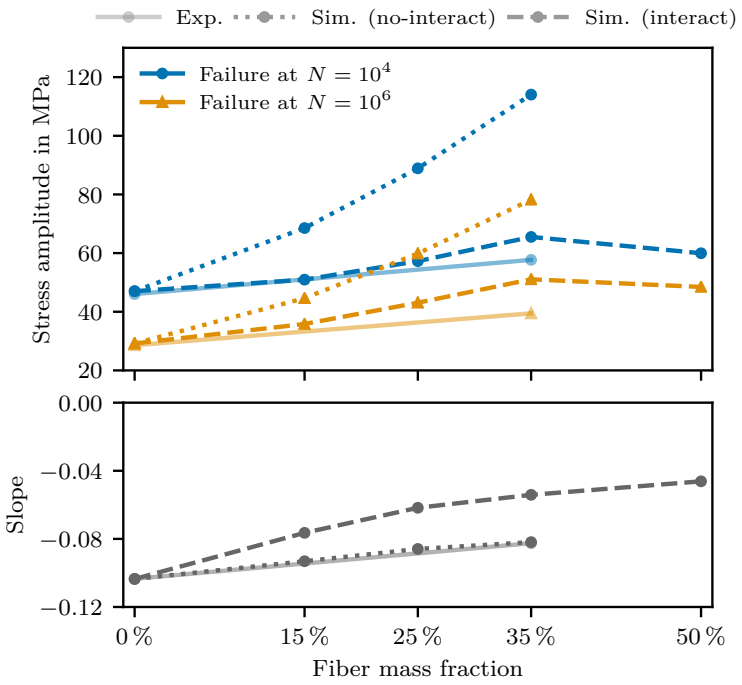

Figure 5.20: Fatigue results for the different 0° composites, including experimental results ("Exp.") and the two models, denoted as "Sim. (no-interact)" and "Sim. (interact)". Simulations were performed on a single-element basis.

fiber damage interaction term is able to accurately model the fiber mass fraction dependent fatigue behavior, not only for the two curves used for the parameter identifications – unreinforced (0 %) and 90° PA66-GF35 (35 %) – but also the other fiber mass fractions. Extrapolation to the highly filled PA66-GF50 (50 %) yields larger deviations with the two modeled fatigue strength curves remaining at nearly the same levels as for the PA66-GF35 case. While the two simulated curves indeed also show an increased slope, the experimental curves show the non-monotonic progression already discussed in Section 5.2.4.

Table 5.3: Table of all model parameters as obtained by the identification procedures.

Fiber damage model			
Axial fiber strength	X_t	=	$960.5\,\mathrm{MPa}$
Transverse fiber strength	Y_t	=	$109.8\,\mathrm{MPa}$
Shear fiber strength	S	=	$194.2\,\mathrm{MPa}$
Weibull shape parameter	k_F	=	1.64
Matrix fatigue damage model			
Critical load	Y_c	=	0
Evolution factor	C	=	9.762×10^{-6}
Damage factor	α	=	4.840
Loading exponent	β	=	8.674
Fiber damage interaction parameter	γ	=	24.5

Further analyses of the model predictions were performed for the predicted fatigue behavior in the $0°$ cases, as highlighted in Fig. 5.20 alongside experimental data for the pure matrix and the $0°$ PA66-GF35 composite. As before, the model including the new interaction term reduces the error in the predicted fatigue life considerably, yielding the expected increased fatigue strength up to a fiber mass fraction of $35\,\%$ and displaying a maximum error of $12\,\mathrm{MPa}$ for the PA66-GF35 composite at 10^6 cycles. At $50\,\%$ fiber mass fraction a reduction of fatigue strength is predicted, similar to the increase observed in the $90°$ predictions.

5.6 Finite-Element results

In the previous section, the model parameters for the relevant PA66-GF50 composites were identified and the first validations using single-element simulations were presented. Using the parameter set summarized in Table 5.3, a final set of finite element analyses of the entire fatigue test specimens for all orientations and fiber mass fractions was performed. As with the finite element analyses performed during the parameter identification procedures, the simulation model was set up as outlined

in Fig. 5.16. The load cycle of fatigue failure was defined as the cycle at which an element reaches the damage threshold of $d_{\mathrm{M}} = 0.95$, indicating the onset of unstable propagation of a macroscopic crack. For each simulated S-N curve the stress amplitude limits were taken from the experimental results and four equally log-spaced stress amplitudes within this range were used for the single simulations. The required computation time for each specimen model with 72720 elements varied between $20\,\mathrm{min}$ and $1.5\,\mathrm{h}$ when run on an eight-core Intel Xeon Gold 6342 CPU.

The S-N curves including the finite element analyses are given in Figs. 5.21, 5.22 and 5.23. All figures also include the unreinforced PA66 S-N curves, as it also serves as a reference for the other data. Naturally, the experimental and simulated PA66 S-N curves match very well, as these tests were the basis for the parameter identification in Section 5.5.6.

A good agreement of experiment and simulation is also achieved for the lower volume fraction materials PA66-GF15 and PA66-GF25, which were not part of the parameter identification set. The $90°$ S-N curves in Fig. 5.21 show that both the increasing slope for higher fiber fractions and the predicted cycles to failure lie close to the experimental data and the maximum error in terms of the stress amplitude for a given number of cycles to failure for both cases remains below $5\,\%$. Similarly good results are also achieved for the $90°$ PA66-GF35 case in Fig. 5.22, which was used to identify the fiber damage interaction parameter. On the other hand, the simulated S-N curve for the $90°$ PA66-GF50 tests exhibit larger deviations from the experimental data. While the slope is predicted well, the cycles to failure are off by more than one order of magnitude. When evaluating the results in terms of the stress amplitude for a given number of cycles to failure, the error lies between $4.8\,\mathrm{MPa}$ (approx. $15\,\%$) and $8.9\,\mathrm{MPa}$ (approx. $20\,\%$). Fig. 5.23 presents the results for the $0°$ PA66-GF35 and previously discussed $90°$ PA66-GF35 curves. Thereby, the *average* cycle to failure for the $0°$ tests is predicted with

acceptable accuracy. Due to the more flat (that is higher-valued) slope of the simulated curve, the predicted cycles to failure show an error of up to one order of magnitude at higher stress amplitudes and a maximum error of $18\,\%$ with respect to the stress amplitude. In this context it remains important to note that no $0°$ S-N curves of any composite grade were included in the identification of the matrix fatigue damage model parameters.

In addition to the S-N curves, the stress amplitudes for three characteristic numbers of cycles to failure ($N = 10^4$, $N = 10^5$ and $N = 10^6$) and the slope of the linear regression of the log-log S-N curves are illustrated in Fig. 5.24 for the $90°$ tests. This supports the previous assessments in that the presented model is able to accurately capture the fatigue behavior, including the slope of the S-N curves for the unreinforced PA66 and $90°$ tests up to and including the PA66-GF35 composite. In case of the PA66-GF50 composite material, the slope is predicted well, but the accuracy for the predicted fatigue life or fatigue strength is low. The explanation for this larger deviation can be reasonably associated with two effects. Firstly, Mori-Tanaka-based mean field homogenization scheme are known to yield lower accuracy results for higher fractions of reinforcing inclusions (eg. Tucker III and Liang, 1999) which might play a stronger role for the high fiber volume fraction of above $30\,\%$ for the PA66-GF50 composite. Secondly, the experimental results suggest that additional damage processes play a role for the PA66-GF50 composite, which are not captured by the model.

Finally, Figures 5.26 and 5.27 show contour plots of the average fiber damage $\bar{d}_{\mathrm{F}}$ and matrix damage d_{M} of the specimen FEM models at the point of predicted fatigue failure. Fig. 5.26 highlights the difference for the different fiber fractions in the $90°$ cases. It becomes apparent that the average fiber damage is higher for the lower fiber content composites, which can be explained by the notion that for these less brittle materials, higher levels of local fiber damage can be endured without leading to

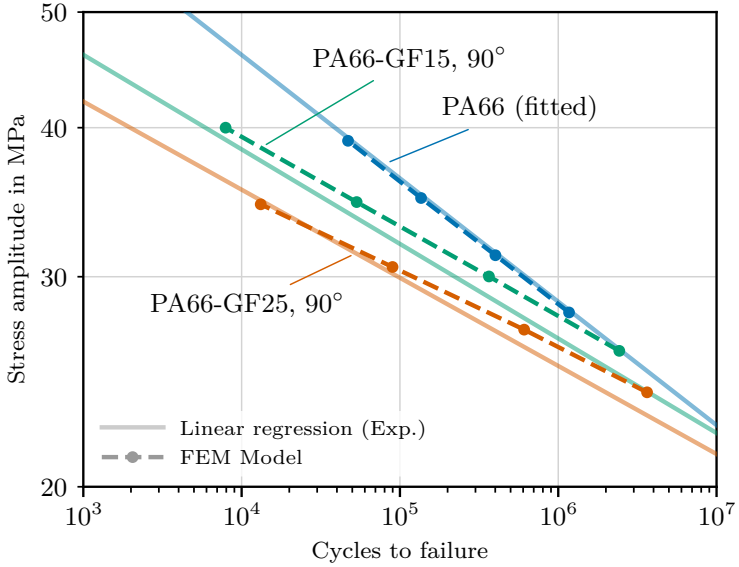

Figure 5.21: S-N curves for the unreinforced PA66, 90° PA66-GF15 and 90° PA66-GF25 materials. Both the linear regression of the log-log experimental data and simulated curves are shown.

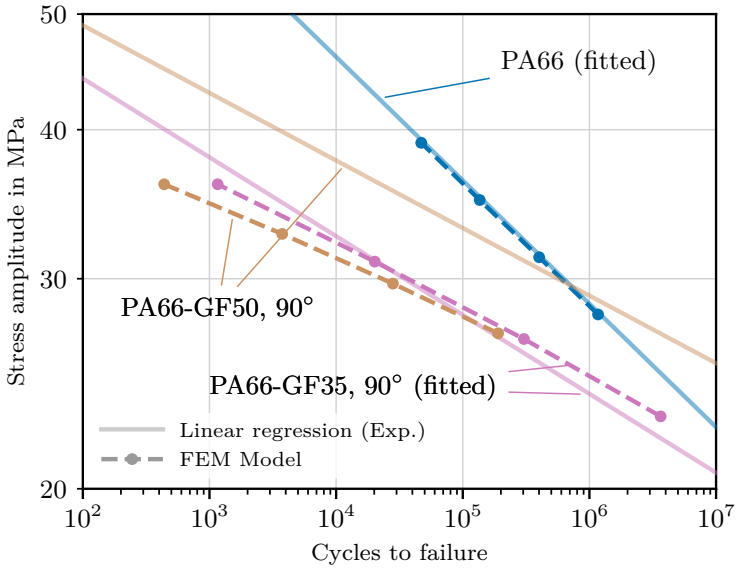

Figure 5.22: S-N curves for the unreinforced PA66, 90° PA66-GF35 and 90° PA66-GF50 materials. Both the linear regression of the log-log experimental data and simulated curves are shown.

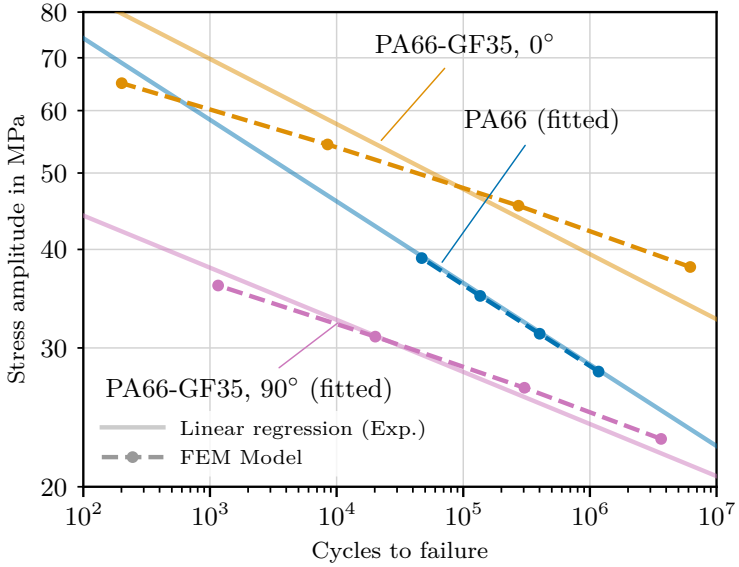

Figure 5.23: S-N curves for the unreinforced PA66, 0° PA66-GF35 and 90° PA66-GF35 materials. Both the linear regression of the log-log experimental data and simulated curves are shown.

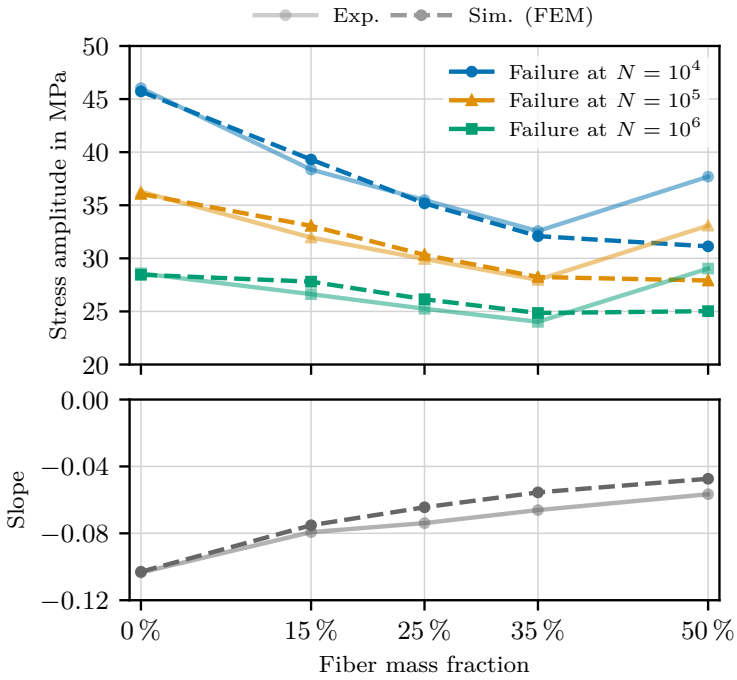

Figure 5.24: Fatigue results for the different 90° composites, including experimental results ("Exp.") and the FEM results, denoted as "Sim. (FEM)"

meso- and macroscopic cracks in the matrix material. A similar behavior is observed for the matrix damage, where the less brittle PA66-GF15 material shows some extent of diffuse matrix damage in the specimen's middle segment, whereas the PA66-GF35 and PA66-GF50 cases yield only localized damage. In all composite grades the matrix damage and hence the predicted location of failure-initiation is found in the shell (i.e., the outer material layers), where the fibers are aligned perpendicular to the loading direction. A comparison of the two specimen orientations ($0°$ and $90°$) of the PA66-GF35 composite is shown in Fig. 5.27. Similar to the above-discussed influence of the fiber fraction, here, the stiffer $0°$ specimen also shows lower levels of diffuse fiber damage whereas the less stiff $90°$ specimen yields higher fiber damage values. As expected, the location of maximum matrix damage in the $0°$ case switches to the core layer, as this is the region with an unfavorable perpendicular fiber orientation.

The observed locations of the localized maximum matrix damage match observations from literature (Rolland et al., 2018), where mesocracks were found to initiate in the core region for $0°$ specimens and at the outer edge of the shell region in the $90°$ case.

While a detailed quantitative analysis of the progressive stiffness reduction on specimen level due to the modeled damage processes was not part of the main scope of the present work, the finite element results yielded the following macroscopic stiffness reduction factors at the end of fatigue life, evaluated at the model clamping length of $50\,\mathrm{mm}$ shown in Fig. 5.16: Between $0.2\,\%$ for the stiffer PA66-GF35 $0°$ tests, $0.4\,\%$ for the PA66-GF35 $90°$ specimens and up to $1.6\,\%$ for the PA66-GF15 $90°$ case. For the pure matrix, a typical stiffness reduction was found to be $2.5\,\%$. Naturally, the local loss of stiffness for the highest loaded elements is much higher, as the matrix damage in these elements reaches levels of up to $95\,\%$, after which the simulation is stopped.

The evolution of the damage variables for the highest-loaded integration points of the finite element model are demonstrated in Fig. 5.25, where a set of representative fatigue simulations with a stress amplitude of $35\,\mathrm{MPa}$ are shown. It can be seen that the average fiber damage variable increases strongly within the first few cycles and shows little change over the following fatigue life. This suggests that the amount of cross-coupling of the cyclic matrix damage law and the quasi-static fiber damage formulation – where a change of matrix stiffness leads to increased loading and further damage of the fiber phase – is limited at best. A noteworthy increase of the fiber damage state is not observed, even after significant matrix damage is present. Progressive debonding or other fiber-related damage mechanisms occurring over larger parts of fatigue life as observed by Rolland et al. (2018) and De Monte et al. (2010a) would be possible with a cyclic fiber damage approach resembling that of the matrix material. Notwithstanding, the level of fiber damage is higher for the lower fiber fraction composite grades and the lowest for the PA66-GF35 $0°$ case. The matrix damage progresses over the entire duration, before increasing strongly within the last $10\,\%$ of fatigue life. Within this evaluation, the final damage increase is more rapid in the low fiber fraction grades and the pure matrix case.

5.7 Summary and outlook

We have presented a micromechanical cyclic damage model for modeling high-cycle fatigue failure of short fiber reinforced composites. An example short glass fiber reinforced thermoplastic composite was used, for which microstructural data and experimental data of different fiber volume fractions was considered.

The Two-Step micromechanical framework in the Mori-Tanaka/Voigt variant was chosen to model the micromechanical behavior of the composite. Previous research had shown that this mean field homogeniza-

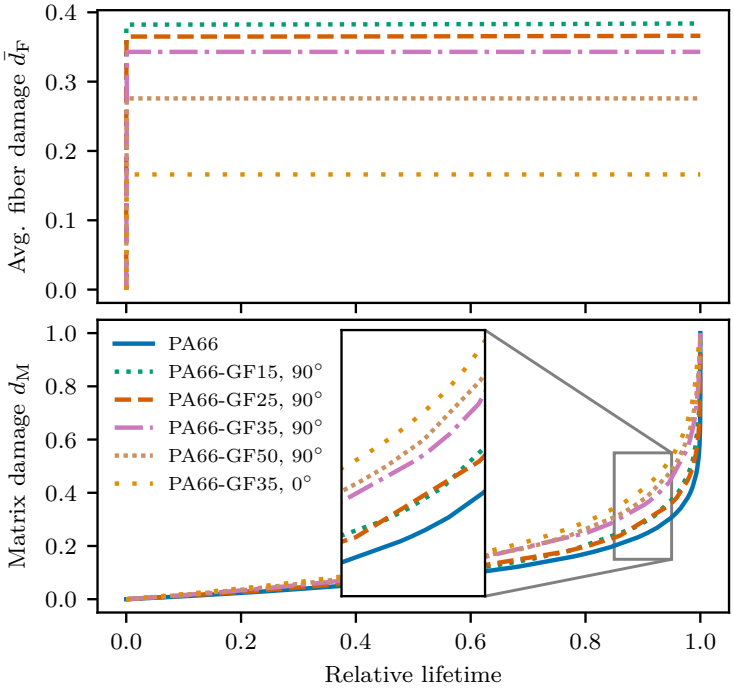

Figure 5.25: Evolution of the average fiber damage variable $\bar{d}_F$ and of the matrix damage variable d_M for the highest-loaded integration point of a set of fatigue simulations with a stress amplitude of 35 MPa and varying fiber fractions.

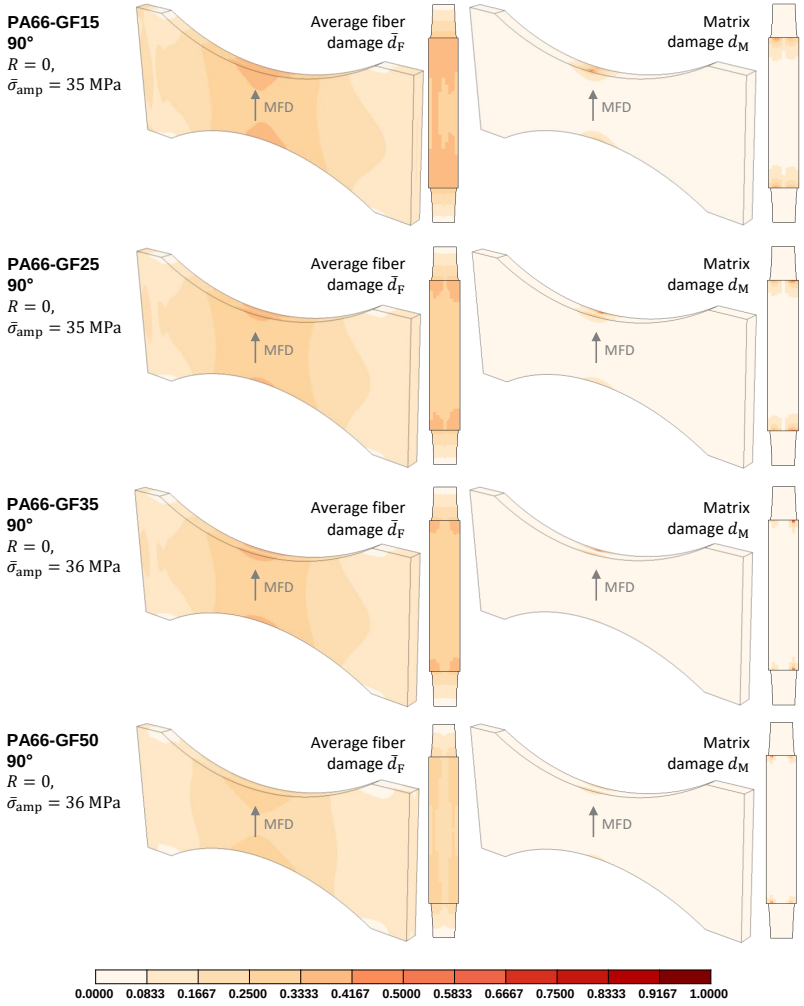

Figure 5.26: Contour plots of the average fiber damage $\bar{d}_F$ and matrix damage d_M at the point of predicted fatigue failure. The cross-sectional view represents the middle (i.e., the thinnest cross-section) of the specimen. All composite grades are given for the 90° configuration. The main fiber direction due to the cavity flow is highlighted as MFD. To simplify comparisons, all results are given for similar loading scenarios between 35 MPa and 36 MPa.

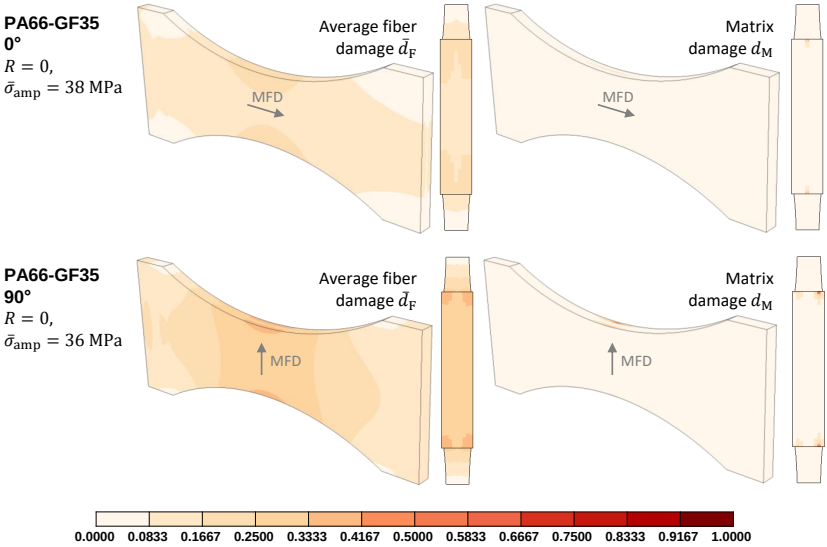

Figure 5.27: Contour plots of the average fiber damage $\bar{d}_F$ and matrix damage d_M at the point of predicted fatigue failure. The cross-sectional view represents the middle (i.e., the thinnest cross-section) of the specimen. Results for the $0°$ and $90°$ test of the PA66-GF35 composite are shown. The main fiber direction due to the cavity flow is highlighted as MFD. To simplify comparisons, all results are given for similar loading scenarios between $36\,\mathrm{MPa}$ and $38\,\mathrm{MPa}$.

tion scheme offers reasonable accuracy while being suitable for modeling complex microstructures. This allows the composite damage to be modeled on the phase level (i.e., matrix and fibers). With respect to the fiber phase, the failure of fibers and of the fiber-matrix interface is modeled using a combination of a Weibull-type probabilistic failure function and a Tsai-Wu transversally isotropic loading function. To account for cyclic loading and fatigue failure, a matrix damage model was proposed, which leveraged the cyclic damage formulation outlined in Peerlings et al. (2000) and included a novel extension which allows the material-specific damage accelerating effect of the fiber damage to be included in the evolution of the matrix damage. This extension was shown to be necessary for the model to correctly describe the influence of the different fiber volume fractions on the fatigue failure limits (i.e., S-N curves). Due to the model's cycle-based formulation, efficient simulations of larger (part-scale) models are made possible, which would otherwise not be feasible for models formulated in time-domain.

Finally, the parameters for the fiber failure model can be identified using regular tensile tests of one composite grade and for different fiber orientation states. The parameters of the matrix damage model can be derived from either two composite S-N curves with different fiber fractions or from one composite S-N curve and one curve for the pure matrix material.

The proposed micromechanical fatigue model including the novel fiber damage interaction term was shown to accurately predict the S-N curves of composite grades between the unreinforced PA66 and reinforced PA66-GF35 $90°$ specimens used for parameter identification. Reasonably good predictions were possible for specimens with a different ($0°$) fiber orientation, but larger deviations were found for a composite with higher fiber content (PA66-GF50) at the $90°$ orientation. This highlights the current limitations of the proposed model for very high volume frac-

tions, where both the employed analytical mean field homogenization techniques and the modeled damage processes seem to be insufficient.

To further improve the model and its predictive qualities, further research should take into account additional loading scenarios with pronounced compressive or multi-axial loading and additional experiments with varying fiber fractions for the $0°$ case. This should include extensions of the matrix model to accommodate the corresponding damage processes. An extension to gradient-enhanced damage modeling (Peerlings et al., 2000; Lenz and Mahnken, 2023) would allow the analysis of damage localization phenomena. With regard to the fiber damage model, a cyclic approach resembling that of the matrix model in this work would allow the fiber and fiber-related damage progression to be more accurately accounted for. Furthermore, future iterations of the model should also put emphasis on the correct prediction of the degradation of the composite stiffness due to the evolution of the progressive damage and comparisons to related experimental results.

Chapter 6

Summary and conclusions

Within this thesis the topic of micromechanical modeling of high cycle fatigue in short glass fiber reinforced thermoplastics (SFRTs) was addressed, leveraging a method for detailed microstructural analyses of x-ray micro-computed tomography (µCT) scans and a micromechanical material modeling framework. While all three parts of this thesis – microstructural analysis, micromechanical modeling and fatigue modeling – are described in a general manner applicable to various short fiber reinforced composites (SFRCs), the focus within this work is on the above-mentioned sub-class of short glass fiber reinforced thermoplastic composites. Furthermore, all experimental data and explicit modeling results refer to a set of commercial short glass fiber reinforced PA66.

After an initial introduction of the over-arching topic, its importance and a summary of the current state of the art for the relevant fields of research in Chapter 1, a brief overview of the fundamentals of SFRTs and their microstructural description was given in Chapter 2.

In **Chapter 3** the analysis of SFRT microstructures using high-resolution µCT and a novel single-fiber segmentation algorithm for raw µCT scan data was covered. This novel method used a set of filtering and segmentation steps to find fibers within the composite material and a successive merging algorithm to join possibly over-segmented fiber parts. The resulting data is comprised of a set of fibers with their parametric description, including location, length, radius and orientation. The method

was applied to three scans of PA66-GF35 specimens, for which between 86 % and 88 % of the entire fiber phase volume could be retrieved.

Validations were performed using both artificially generated 3D scan images with known microstructural statistics and using analysis results of fiber orientation tensors from commercial software, demonstrating the accuracy of the retrieved fiber orientation. The quality of the fiber length analysis was successfully validated by comparing it to the length distribution of an experimental analysis of an incinerated specimen. Because the presented algorithm can relate a single fiber's orientation with its length, it could be shown that there exists a noteworthy correlation between fiber length and orientation, where long fibers are predominantly found to be oriented in the main flow direction, whereas the fiber orientation of very short fibers was found to be less highly oriented.

Limitations of the presented algorithm were found to be associated with very high fiber content composites, such as the studied PA66-GF50 composite, for which a lower volumetric detection rate of 59 % was observed.

The chapter's results indicate that the developed algorithm is a capable and valuable method for obtaining high-accuracy microstructural information for SFRTs when paired with high-resolution µCT data. This kind of microstructural data offers insights that are invaluable for detailed models of the given material class, especially due to the linking of orientation, location and shape for each fiber.

Chapter 4 covers the micromechanical modeling of SFRTs using analytical mean field homogenization schemes, which enable efficient modeling of this material class by including microstructural influence factors. The Self-Consistent (Hill, 1965; Budiansky, 1965), Mori-Tanaka (MT) (Mori and Tanaka, 1973; Benveniste, 1987), Ponte Castañeda-Willis (PCW) (Ponte Castañeda and Willis, 1995), Interaction Direct Derivative (IDD) (Zheng and Du, 2001) and Two-Step (TS) (Pierard et al., 2004)

homogenization schemes are introduced, as they represent a set of typically applied and studied mean field models.

Great emphasis was put on a unified algebraic formulation of the models, which allows for a clearer and more intuitive comparison. It was shown that the equations for the MT, PCW and IDD models only differ in the specific role and formulation of the $\mathbb{P}_\beta^{\mathrm{D}}$ (or $\mathbb{Q}_\beta^{\mathrm{D}}$) tensors, which can be associated with the spatial distribution of the inclusions, i.e., the fibers. Furthermore, the multilayer formulation of Glüge and Kalisch (2014) and the adaptive orientation averaging scheme of Goldberg et al. (2017) were introduced, alongside the canonical Advani-Tucker averaging method and a classical quadrature scheme.

Using these tools and detailed fiber orientation data obtained using the method described in Chapter 3, different benchmarks were performed. This included the accuracy and computational effort of the orientation averaging schemes, the accuracy of different levels of microstructural fidelity and, finally, of the different homogenization schemes. Therein, both the predicted effective stiffness tensor of the composite as well as the prediction of the local stresses were considered.

To validate the different results, both experimentally measured Young's moduli from tensile tests and results from full-field FFT simulations were employed.

In conclusion, it was shown that for the given SFRT material, the MT and TS schemes yield robust and accurate stiffness predictions, when compared to the full-field results and experimental data. Due to the MT scheme's limitations with respect to composites with inclusions of different shape or non-isotropic or inhomogeneous inclusion materials, the TS scheme stands out as a robust and widely applicable model. The expected limitations due to the TS model's simple structure were not observed in the predicted stiffness tensors and the differences in the predicted phase stresses – when compared to other models, such as the MT scheme – were small. Larger deviations in the fiber stress

predictions were found only for the $0°$ loading case, where all models underestimated the prevalence of high-stress regions in the fiber phase that were predicted by the full-field FFT results.

With respect to the influence of the fidelity of the microstructural setup, it was shown that the effective stiffness of the composite was most accurately predicted when either considering the full microstructural data – i.e., the layered microstructure with layer-specific volume fractions and considering every single fiber – or by modeling the specimen as a multilayer composite with layer-specific fiber orientation tensors and otherwise constant parameters. The predicted stress distribution in the fiber phase was found to be similar for most setups, with larger differences in the $0°$ case.

Finally, **Chapter 5** introduced a micromechanical model for high cycle fatigue damage and failure in SFRTs. It was developed and tested on different grades of the same short glass fiber reinforced thermoplastic PA66 as in the two previous chapters, with fiber mass fractions between $15\,\%$ and $50\,\%$. For this purpose, the detailed microstructural data from Chapter 3 and additional fiber orientation tensors from Pietrogrande et al. (2021) were used. Based on the insights from Chapter 4, the Two-Step homogenization framework from Pierard et al. (2004) was chosen. It offers a favorable algebraic structure and was shown to be robust with respect to heterogeneous (eg., damaged) fiber phase materials (cf. Chapter 4).

The damage modeling was split in two parts: the fiber domain and its vicinity and the matrix domain. For the prior, a quasi-static damage law was proposed, which was calibrated using tensile tests for the PA66-GF35 composite. In the latter case, a modification of the Peerlings et al. (2000) cyclic damage law was used, which was extended by a novel interaction term that couples the matrix damage rate to the average state of damage in the fiber domain. This extension drastically improved the model's ability to predict the fatigue behavior of other composite grades and

orientation states. The cycle-based formulation allows the model to be used for high-cycle fatigue, where time-based numerical schemes are unfeasible.

In the end, the parametrization of the model required two composite S-N curves – one of the unreinforced PA66 material and one for the PA66-GF35 $90°$ composite – to predict the composite S-N curves of the intermediate fiber fractions and – with reasonable accuracy – of the PA66-GF35 $0°$ case, as demonstrated by comparison to experimental data. Larger errors were observed for the high fiber fraction PA66-GF50 composite in the $90°$ case. To this end, the results suggest that the model captures many micromechanical influence factors necessary to predict the fatigue behavior of different orientation states and fiber volume fractions within the given fiber fraction range.

Bibliography

Aboutajeddine, A., Neale, K., Feb. 2005. The double-inclusion model: a new formulation and new estimates. Mechanics of Materials 37 (2-3), 331–341.

Advani, S. G., Tucker III, C. L., 1987. The use of tensors to describe and predict fiber orientation in short fiber composites. Journal of Rheology 31 (8), 751–783.

Arif, M., Saintier, N., Meraghni, F., Fitoussi, J., Chemisky, Y., Robert, G., May 2014. Multiscale fatigue damage characterization in short glass fiber reinforced polyamide-66. Composites Part B: Engineering 61, 55–65.

Axelsson, M., Dec. 2008. Estimating 3D fibre orientation in volume images. In: 2008 19th International Conference on Pattern Recognition. IEEE.

Bary, B., Oct. 2011. Estimation of poromechanical and thermal conductivity properties of unsaturated isotropically microcracked cement pastes. International Journal for Numerical and Analytical Methods in Geomechanics 35 (14), 1560–1586.

Bay, R. S., Tucker III, C. L., Feb. 1992. Stereological measurement and error estimates for three-dimensional fiber orientation. Polymer Engineering and Science 32 (4), 240–253.

Becker, F., 2009. Entwicklung einer Beschreibungsmethodik für das mechanische Verhalten unverstärkter Thermoplaste bei hohen Deformationsgeschwindigkeiten. Doctoral Thesis, Martin-Luther-Universität Halle-Wittenberg.

Belmonte, E., De Monte, M., Hoffmann, C.-J., Quaresimin, M., Mar. 2017a. Damage initiation and evolution in short fiber reinforced polyamide under fatigue loading: Influence of fiber volume fraction. Composites Part B: Engineering 113, 331–341.

Belmonte, E., De Monte, M., Hoffmann, C.-J., Quaresimin, M., Jan. 2017b. Damage mechanisms in a short glass fiber reinforced polyamide under fatigue loading. International Journal of Fatigue 94, 145–157.

Belmonte, E., De Monte, M., Quaresimin, M., Hoffmann, C., 2014. Damage evolution in short fiber reinforced polyamide under fatigue loading: influence of the fiber volume fraction. In: 43° Convegno Nazionale AIAS. Rimini.

Benveniste, Y., 1987. A new approach to the application of Mori-Tanaka's theory in composite materials. Mechanics of Materials 6 (2), 147–157.

Benveniste, Y., Dvorak, G. J., Chen, T., 1991. On diagonal and elastic symmetry of the approximate effeffect stiffness tensor of heterogeneous media. Journal of the Mechanics and Physics of Solids 39 (7), 927–946.

Bernasconi, A., Cosmi, F., Dreossi, D., Sep. 2008. Local anisotropy analysis of injection moulded fibre reinforced polymer composites. Composites Science and Technology 68 (12), 2574–2581.

Bernasconi, A., Davoli, P., Basile, A., Filippi, A., Feb. 2007. Effect of fibre orientation on the fatigue behaviour of a short glass fibre reinforced polyamide-6. International Journal of Fatigue 29 (2), 199–208.

Bertram, A., 2012. Elasticity and Plasticity of Large Deformations: An Introduction. Springer Berlin Heidelberg, Berlin, Heidelberg.

Böhlke, T., Brüggemann, C., 2001. Graphical representation of the generalized Hooke's law. Technische Mechanik 21 (2), 145–158.

Böhlke, T., Othmani, Y., Dec. 2013. A two-scale weakest link model based on a micromechanical approach. Computational Materials Science 80, 43–50.

Blanc, R., Germain, C., Da Costa, J. D., Baylou, P., Cataldi, M., Feb. 2006. Fiber orientation measurements in composite materials. Composites Part A: Applied Science and Manufacturing 37 (2), 197–206.

Brylka, B., 2017. Charakterisierung und Modellierung der Steifigkeit von langfaserverstärktem Polypropylen. Doctoral Thesis, Karlsruhe Institute of Technology (KIT).

Buck, F., Brylka, B., Müller, V., Müller, T., Weidenmann, K. A., Hrymak, A. N., Henning, F., Böhlke, T., 2015. Two-scale structural mechanical modeling of long fiber reinforced thermoplastics. Composites Science and Technology 117, 159–167.

Budiansky, B., Aug. 1965. On the elastic moduli of some heterogeneous materials. Journal of the Mechanics and Physics of Solids 13 (4), 223–227.

Burger, W., Burge, M. J., 2009a. Principles of Digital Image Processing. Undergraduate Topics in Computer Science. Springer London, London.

Burger, W., Burge, M. J., 2009b. Principles of digital image processing: fundamental techniques. Undergraduate topics in computer science. Springer, London.

Chaboche, J. L., 1988. Continuum Damage Mechanics: Part I—General Concepts. Journal of Applied Mechanics 55 (1), 59.

Charpin, L., Ehrlacher, A., Sep. 2014. Microporomechanics study of anisotropy of ASR under loading. Cement and Concrete Research 63, 143–157.

Christensen, R. M., Lo, K. H., 1979. Solutions for effective shear properties in three phase sphere and cylinder models. J. Mech. Phys. Solids 27, 315–330.

Clarke, A., Archenhold, G., Davidson, N., Jan. 1995. A novel technique for determining the 3D spatial distribution of glass fibres in polymer composites. Composites Science and Technology 55 (1), 75–91.

Dask Development Team, 2016. Dask: Library for dynamic task scheduling.
URL https://dask.org

Davidson, N. C., Clarke, A. R., Archenhold, G., Feb. 1997. Large-area, high-resolution image analysis of composite materials. Journal of Microscopy 185 (2), 233–242.

De Monte, M., Moosbrugger, E., Jaschek, K., Quaresimin, M., 2010a. Multiaxial fatigue of a short glass fibre reinforced polyamide 6.6 - Fatigue and fracture behaviour. International Journal of Fatigue 32, 17–28.

De Monte, M., Moosbrugger, E., Quaresimin, M., Oct. 2010b. Influence of temperature and thickness on the off-axis behaviour of short glass fibre reinforced polyamide 6.6 – cyclic loading. Composites Part A: Applied Science and Manufacturing 41 (10), 1368–1379.

De Monte, M., Moosbrugger, E., Quaresimin, M., Jul. 2010c. Influence of temperature and thickness on the off-axis behaviour of short glass fibre reinforced polyamide 6.6 – Quasi-static loading. Composites Part A: Applied Science and Manufacturing 41 (7), 859–871.

de Paiva, R. F., Bisiaux, M., Lynch, J., Rosenberg, E., Jun. 1996. High resolution x-ray tomography in an electron microprobe. Review of Scientific Instruments 67 (6), 2251–2256.

Domininghaus, H., Elsner, P., Eyerer, P., Hirth, T., 2012. Kunststoffe: Eigenschaften und Anwendungen. Springer Berlin Heidelberg, Berlin, Heidelberg.

Du, D.-X., Zheng, Q.-S., 2002. A further exploration of the interaction direct derivative (IDD) estimate for the effective properties of multiphase composites taking into account inclusion distribution. Acta Mechanica 157 (1-4), 61–80.

e-Xstream engineering, 2020. Digimat User's Manual, Release 2020.0.

Eberhardt, C., Clarke, A., Vincent, M., Giroud, T., Flouret, S., Oct. 2001. Fibre-orientation measurements in short-glass-fibre composites—II: A quantitative error estimate of the 2D image analysis technique. Composites Science and Technology 61 (13), 1961–1974.

Eberhardt, C. N., Clarke, A. R., Apr. 2002. Automated reconstruction of curvilinear fibres from 3D datasets acquired by X-ray microtomography. Journal of Microscopy 206 (1), 41–53.

Eshelby, J. D., Aug. 1957. The determination of the elastic field of an ellipsoidal inclusion, and related problems. Proceedings of the Royal Society A: Mathematical, Physical and Engineering Sciences 241 (1226), 376–396.

Eyre, D. J., Milton, G. W., Apr. 1999. A fast numerical scheme for computing the response of composites using grid refinement. The European Physical Journal Applied Physics 6 (1), 41–47.

Fakirov, S., Fakirova, C., Jan. 1985. Direct determination of the orientation of short glass fibers in an injection-molded poly(ethylene terephthalate) system. Polymer Composites 6 (1), 41–46.

Ferrari, M., May 1991. Asymmetry and the high concentration limit of the Mori-Tanaka effective medium theory. Mechanics of Materials 11 (3), 251–256.

Ferrari, M., Jan. 1994. Composite homogenization via the equivalent poly-inclusion approach. Composites Engineering 4 (1), 37–45.

Fischer, G., Schwarz, P., Mueller, U., Fritz, U., 1990. Measuring spatial fiber orientation—A method for quality control of fiber reinforced plastics. Advances in Polymer Technology 10 (2), 135–141.

Fitoussi, J., Bourgeois, N., Guo, G., Baptiste, D., Feb. 1996. Prediction of the anisotropic damaged behavior of composite materials: introduction of multilocal failure criteria in a micro-macro relationship. Computational Materials Science 5 (1-3), 87–100.

Fitoussi, J., Guo, G., Baptiste, D., Jan. 1998. A statistical micromechanical model of anisotropic damage for S.M.C. composites. Composites Science and Technology 58 (5), 759–763.

Folgar, F., Tucker III, C. L., Apr. 1984. Orientation behavior of fibers in concentrated suspensions. Journal of Reinforced Plastics and Composites 3 (2), 98–119.

Fritzen, F., Böhlke, T., Feb. 2011. Nonuniform transformation field analysis of materials with morphological anisotropy. Composites Science and Technology 71 (4), 433–442.

Fu, S.-Y., Hu, X., Yue, C.-Y., 1999. Effects of fiber length and orientation distributions on the mechanical properties of short-fiber-reinforced polymers—A review. Materials Science Research International 5 (2), 74–83.

Fu, S.-Y., Lauke, B., 1996. Effects of fiber length and fiber orientation distributions on the tensile strength of short-fiber-reinforced polymers. Composites Science and Technology 56 (10), 1179–1190.

Fu, S.-Y., Lauke, B., Mar. 1998. The elastic modulus of misaligned short-fiber-reinforced polymers. Composites Science and Technology 58 (3-4), 389–400.

Fu, S.-Y., Lauke, B., Mäder, E., Yue, C.-Y., Hu, X., 2000. Tensile properties of short-glass-fiber-and short-carbon-fiber-reinforced polypropylene composites. Composites Part A: Applied Science and Manufacturing 31 (10), 1117–1125.

Gajek, S., Schneider, M., Böhlke, T., Sep. 2020. On the micromechanics of deep material networks. Journal of the Mechanics and Physics of Solids 142, 103984.

Gavazzi, A. C., Lagoudas, D. C., 1990. On the numerical evaluation of Eshelby's tensor and its application to elastoplastic fibrous composites. Computational Mechanics 7 (1), 13–19.

Glöckner, R., Kolling, S., Heiliger, C., 2016. A monte-carlo algorithm for 3D fibre detection from microcomputer tomography. Journal of Computational Engineering 2016, 1–9.

Glüge, R., Kalisch, J., May 2014. The effective stiffness and stress concentrations of a multi-layer laminate. Composite Structures 111, 580–586.

Goldberg, N., Ospald, F., Schneider, M., 2017. A fiber orientation-adapted integration scheme for computing the hyperelastic Tucker average for short fiber reinforced composites. Computational Mechanics 60 (4), 595–611.

Gouillart, E., Nunez-Iglesias, J., van der Walt, S., 2016. Analyzing micro-tomography data with Python and the scikit-image library. Advanced Structural and Chemical Imaging 2 (18).

Hessman, P. A., Riedel, T., Welschinger, F., Hornberger, K., Böhlke, T., Oct. 2019. Microstructural analysis of short glass fiber reinforced thermoplastics based on x-ray micro-computed tomography. Composites Science and Technology 183, 107752.

Hessman, P. A., Welschinger, F., Hornberger, K., Böhlke, T., Nov. 2021. On mean field homogenization schemes for short fiber reinforced composites: Unified formulation, application and benchmark. International Journal of Solids and Structures 230-231, 111141.

Hessman, P. A., Welschinger, F., Hornberger, K., Böhlke, T., Sep. 2023. A micromechanical cyclic damage model for high cycle fatigue failure of short fiber reinforced composites. Composites Part B: Engineering 264, 110855.

Hill, R., 1963. Elastic properties of reinforced solids: some theoretical principles. Journal of the Mechanics and Physics of Solids 11 (5), 357–372.

Hill, R., Aug. 1965. A self-consistent mechanics of composite materials. Journal of the Mechanics and Physics of Solids 13 (4), 213–222.

Holzapfel, G. A., 2000. Nonlinear Solid Mechanics: A Continuum Approach for Engineering. Wiley, Chichester; New York.

Hori, M., Nemat-Nasser, S., Jan. 1993. Double-inclusion model and overall moduli of multi-phase composites. Mechanics of Materials 14 (3), 189–206.

Horst, J. J., Spoormaker, J. L., 1996. Mechanisms of fatigue in short glass fiber reinforced polyamide 6. Polymer Engineering & Science 36 (22), 2718–2726.

Hu, G., Weng, G., Aug. 2000a. The connections between the double-inclusion model and the Ponte Castaneda–Willis, Mori–Tanaka, and Kuster–Toksoz models. Mechanics of Materials 32 (8), 495–503.

Hu, G. K., Weng, G. J., Mar. 2000b. Some reflections on the Mori-Tanaka and Ponte Castañeda-Willis methods with randomly oriented ellipsoidal inclusions. Acta Mechanica 140 (1-2), 31–40.

Jain, A., Abdin, Y., Van Paepegem, W., Verpoest, I., Lomov, S. V., 2015a. Effective anisotropic stiffness of inclusions with debonded interface for Eshelby-based models. Composite Structures 131, 692–706.

Jain, A., Lomov, S. V., Abdin, Y., Verpoest, I., Van Paepegem, W., 2013. Pseudo-grain discretization and full Mori Tanaka formulation for random heterogeneous media: Predictive abilities for stresses in individual inclusions and the matrix. Composites Science and Technology 87, 86–93.

Jain, A., Veas, J. M., Straesser, S., Van Paepegem, W., Verpoest, I., Lomov, S. V., Dec. 2015b. The Master SN curve approach – A hybrid multi-scale fatigue simulation of short fiber reinforced composites. Composites Part A: Applied Science and Manufacturing 91, 510–518.

Jones, E., Oliphant, T., Peterson, P., , et al., 2001. Scipy: Open source scientific tools for python.

Kabir, M., Lutz, W., Zhu, K., Schmauder, S., Jul. 2006. Fatigue modeling of short fiber reinforced composites with ductile matrix under cyclic loading. Computational Materials Science 36 (4), 361–366.

Kaiser, J.-M., Stommel, M., 2012. Strength prediction of short fibre reinforced polymers. Zeitschrift Kunststofftechnik/ Journal of Plastics Technology 8 (3), 278–300.

Kammoun, S., Doghri, I., Adam, L., Robert, G., Delannay, L., Dec. 2011. First pseudo-grain failure model for inelastic composites with misaligned short fibers. Composites Part A: Applied Science and Manufacturing 42 (12), 1892–1902.

Kammoun, S., Doghri, I., Brassart, L., Delannay, L., Jun. 2015. Micromechanical modeling of the progressive failure in short glass–fiber reinforced thermoplastics – First Pseudo-Grain Damage model. Composites Part A: Applied Science and Manufacturing 73, 166–175.

Kanatani, K., Jan. 1984. Distribution of directional data and fabric tensors. International Journal of Engineering Science 22 (2), 149–164.

Köbler, J., Magino, N., Andrä, H., Welschinger, F., Müller, R., Schneider, M., Jan. 2021. A computational multi-scale model for the stiffness degradation of short-fiber reinforced plastics subjected to fatigue loading. Computer Methods in Applied Mechanics and Engineering 373, 113522.

Köbler, J., Schneider, M., Ospald, F., Andrä, H., Müller, R., Jun. 2018. Fiber orientation interpolation for the multiscale analysis of short fiber reinforced composite parts. Computational Mechanics 61 (6), 729–750.

Klusemann, B., Svendsen, B., 2010. Homogenization methods for multi-phase elastic composites: Comparisons and benchmarks. Technische Mechanik 30 (4), 374–386.

Krairi, A., Doghri, I., 2013. Multi-scale Damage Model for Mechanical High Cycle Fatigue (HCF) of Short Glass Fibre Reinforced Thermoplastics (SGFRTP). Procedia Engineering 66, 759–765.

Krairi, A., Doghri, I., Robert, G., Nov. 2016. Multiscale high cycle fatigue models for neat and short fiber reinforced thermoplastic polymers. International Journal of Fatigue 92, 179–192.

Krause, M., Hausherr, J. M., Burgeth, B., Herrmann, C., Krenkel, W., Feb. 2010. Determination of the fibre orientation in composites using the structure tensor and local X-ray transform. Journal of Materials Science 45 (4), 888–896.

Lebedev, V., Jan. 1976. Quadratures on a sphere. USSR Computational Mathematics and Mathematical Physics 16 (2), 10–24.

Lemaitre, J., Chaboche, J.-L., Feb. 1990. Mechanics of Solid Materials, 1st Edition. Cambridge University Press.

Lenz, P., Mahnken, R., Nov. 2019. Damage simulation of fiber reinforced composites using mean-field homogenization methods. PAMM 19 (1).

Lenz, P., Mahnken, R., Jun. 2023. Non-local integral-type damage combined to mean-field homogenization methods for composites and its parallel implementation. Composite Structures 314, 116911.

Liu, Z., Wu, C., Jun. 2019. Exploring the 3D architectures of deep material network in data-driven multiscale mechanics. Journal of the Mechanics and Physics of Solids 127, 20–46.

Liu, Z., Wu, C., Koishi, M., Mar. 2019. A deep material network for multiscale topology learning and accelerated nonlinear modeling of heterogeneous materials. Computer Methods in Applied Mechanics and Engineering 345, 1138–1168.

Magino, N., Köbler, J., Andrä, H., Welschinger, F., Müller, R., Schneider, M., Jan. 2022a. A multiscale high-cycle fatigue-damage model for the stiffness degradation of fiber-reinforced materials based on a mixed variational framework. Computer Methods in Applied Mechanics and Engineering 388, 114198.

Magino, N., Köbler, J., Andrä, H., Welschinger, F., Müller, R., Schneider, M., May 2022b. A space-time upscaling technique for modeling high-cycle fatigue-damage of short-fiber reinforced composites. Composites Science and Technology 222, 109340.

Michel, J., Suquet, P., Dec. 2003. Nonuniform transformation field analysis. International Journal of Solids and Structures 40 (25), 6937–6955.

Müller, V., Böhlke, T., Jun. 2016. Prediction of effective elastic properties of fiber reinforced composites using fiber orientation tensors. Composites Science and Technology 130, 36–45.

Müller, V., Brylka, B., Dillenberger, F., Glöckner, R., Kolling, S., Böhlke, T., Feb. 2016. Homogenization of elastic properties of short-fiber reinforced composites based on measured microstructure data. Journal of Composite Materials 50 (3), 297–312.

Müller, V., Kabel, M., Andrä, H., Böhlke, T., Aug. 2015. Homogenization of linear elastic properties of short-fiber reinforced composites – A comparison of mean field and voxel-based methods. International Journal of Solids and Structures 67-68, 56–70.

Montgomery-Smith, S., He, W., Jack, D. A., Smith, D. E., Aug. 2011a. Exact tensor closures for the three-dimensional Jeffery's equation. Journal of Fluid Mechanics 680, 321–335.

Montgomery-Smith, S., Jack, D., Smith, D. E., Apr. 2011b. The Fast Exact Closure for Jeffery's equation with diffusion. Journal of Non-Newtonian Fluid Mechanics 166 (7-8), 343–353.

Mori, T., Tanaka, K., May 1973. Average stress in matrix and average elastic energy of materials with misfitting inclusions. Acta Metallurgica 21 (5), 571–574.

Moulinec, H., Suquet, P., Apr. 1998. A numerical method for computing the overall response of nonlinear composites with complex microstructure. Computer Methods in Applied Mechanics and Engineering 157 (1-2), 69–94.

Mura, T., 1987. Micromechanics of defects in solids, 2nd Edition. No. 3 in Mechanics of elastic and inelastic solids. M. Nijhoff ; Distributors for the U.S. and Canada, Kluwer Academic Publishers, Dordrecht, Netherlands; Boston: Hingham, MA, USA.

Nadeau, J., Ferrari, M., Nov. 2001. On optimal zeroth-order bounds with application to Hashin–Shtrikman bounds and anisotropy parameters. International Journal of Solids and Structures 38 (44-45), 7945–7965.

Naili, C., Doghri, I., Kanit, T., Sukiman, M., Aissa-Berraies, A., Imad, A., Feb. 2020. Short fiber reinforced composites: Unbiased full-field evaluation of various homogenization methods in elasticity. Composites Science and Technology 187, 107942.

Nemat-Nasser, S., Hori, M., 2010. Micromechanics: overall properties of heterogeneous materials, 2nd Edition. Elsevier, Amsterdam.

Otsu, N., Jan. 1979. A threshold selection method from gray-level histograms. IEEE Transactions on Systems, Man, and Cybernetics 9 (1), 62–66.

Peerlings, R. H. J., 1999. Enhanced damage modelling for fracture and fatigue. Doctoral Thesis, Technische Universiteit Eindhoven.

Peerlings, R. H. J., Brekelmans, W. A. M., de Borst, R., Geers, M. G. D., Dec. 2000. Gradient-enhanced damage modelling of high-cycle fatigue. International Journal for Numerical Methods in Engineering 49 (12), 1547–1569.

Pierard, O., Friebel, C., Doghri, I., Aug. 2004. Mean-field homogenization of multi-phase thermo-elastic composites: a general framework and its validation. Composites Science and Technology 64 (10-11), 1587–1603.

Pietrogrande, R., Carraro, P., De Monte, M., Quaresimin, M., Jan. 2021. Modelling the influence of the micrustructure on the high cycle fatigue crack initiation in short fibre reinforced thermoplastics. Composites Science and Technology 201, 108533.

Pietrogrande, R., Carraro, P. A., De Monte, M., Quaresimin, M., Oct. 2018. A novel pseudo-grain approach for the estimation of the elastic stress distributions within the matrix of short fiber-reinforced polymers. Composites Part B: Engineering 150, 115–123.

Pinter, P., Dietrich, S., Bertram, B., Kehrer, L., Elsner, P., Weidenmann, K., Apr. 2018. Comparison and error estimation of 3D fibre orientation analysis of computed tomography image data for fibre reinforced composites. NDT & E International 95, 26–35.

Ponte Castañeda, P., Suquet, P., 1997. Nonlinear Composites. In: Advances in Applied Mechanics. Vol. 34. Elsevier, pp. 171–302.

Ponte Castañeda, P., Willis, J. R., Dec. 1995. The effect of spatial distribution on the effective behavior of composite materials and cracked media. Journal of the Mechanics and Physics of Solids 43 (12), 1919–1951.

Robb, K., Wirjadi, O., Schladitz, K., Sep. 2007. Fiber orientation estimation from 3D image data: practical algorithms, visualization, and interpretation. In: 7th International Conference on Hybrid Intelligent Systems. IEEE.

Rocklin, M., 2015. Dask: parallel computation with blocked algorithms and task scheduling. In: Huff, K., Bergstra, J. (Eds.), Proceedings of the 14th Python in Science Conference.

Rolland, H., Saintier, N., Raphael, I., Lenoir, N., King, A., Robert, G., Jun. 2018. Fatigue damage mechanisms of short fiber reinforced PA66 as observed by in-situ synchrotron X-ray microtomography. Composites Part B: Engineering 143, 217–229.

Rolland, H., Saintier, N., Robert, G., Apr. 2016. Damage mechanisms in short glass fibre reinforced thermoplastic during in situ microtomography tensile tests. Composites Part B: Engineering 90, 365–377.

Salaberger, D., Jerabek, M., Koch, T., Kastner, J., Jul. 2015. Consideration of accuracy of quantitative X-ray CT analyses for short-glass-fibre-reinforced polymers. Materials Science Forum 825-826, 907–913.

Salaberger, D., Kannappan, K. A., Kastner, J., Reussner, J., Auinger, T., Jul. 2011. Evaluation of computed tomography data from fibre reinforced polymers to determine fibre length distribution. International Polymer Processing 26 (3), 283–291.

Sato, N., Kurauchi, T., Sato, S., Kamigaito, O., 1991. Microfailure behaviour of randomly dispersed short fibre reinforced thermoplastic composites obtained by direct SEM observation. Journal of materials science 26 (14), 3891–3898.

Schemmann, M., Görthofer, J., Seelig, T., Hrymak, A., Böhlke, T., Jun. 2018. Anisotropic meanfield modeling of debonding and matrix damage in SMC composites. Composites Science and Technology 161, 143–158.

Schjødt-Thomsen, J., Pyrz, R., 2001. The Mori–Tanaka stiffness tensor: diagonal symmetry, complex fibre orientations and non-dilute volume fractions. Mechanics of Materials 33 (10), 531–544.

Schneider, M., Feb. 2017. The sequential addition and migration method to generate representative volume elements for the homogenization of short fiber reinforced plastics. Computational Mechanics 59 (2), 247–263.

Schneider, M., Ospald, F., Kabel, M., Mar. 2016. Computational homogenization of elasticity on a staggered grid. International Journal for Numerical Methods in Engineering 105 (9), 693–720.

Shen, H., Nutt, S., Hull, D., Oct. 2004. Direct observation and measurement of fiber architecture in short fiber-polymer composite foam through micro-CT imaging. Composites Science and Technology 64 (13-14), 2113–2120.

Spahn, J., Andrä, H., Kabel, M., Müller, R., Jan. 2014. A multiscale approach for modeling progressive damage of composite materials using fast Fourier transforms. Computer Methods in Applied Mechanics and Engineering 268, 871–883.

Stora, E., He, Q.-C., Bary, B., Jul. 2006. Influence of inclusion shapes on the effective linear elastic properties of hardened cement pastes. Cement and Concrete Research 36 (7), 1330–1344.

Tandon, G., Weng, G., Jan. 1986. Average stress in the matrix and effective moduli of randomly oriented composites. Composites Science and Technology 27 (2), 111–132.

Tandon, G. P., Weng, G. J., Oct. 1984. The effect of aspect ratio of inclusions on the elastic properties of unidirectionally aligned composites. Polymer Composites 5 (4), 327–333.

Tognevi, A., Bary, B., Delaplace, A., 2010. Micromechanical estimation of hydro-mechanical parameters in unsaturated microcracked concrete. In: Fracture mechanics of concrete and concrete structures: proceedings of the 7th International Conference on Fracture Mechanics of Concrete and Concrete Structures. Korea Concrete Institute, Jeju, South Korea.

Tsai, S. W., Wu, E. M., 1971. A general theory of strength for anisotropic materials. Journal of composite materials 5 (1), 58–80.

Tucker III, C. L., Liang, E., Apr. 1999. Stiffness predictions for unidirectional short-fiber composites: Review and evaluation. Composites Science and Technology 59 (5), 655–671.

van der Walt, S., Schönberger, J. L., Nunez-Iglesias, J., Boulogne, F., Warner, J. D., Yager, N., Gouillart, E., Yu, T., Jun. 2014. scikit-image: image processing in Python. PeerJ 2 (e453).

von Turkovich, R., Erwin, L., Sep. 1983. Fiber fracture in reinforced thermoplastic processing. Polymer Engineering and Science 23 (13), 743–749.

Wallenberger, F. T., Bingham, P. A. (Eds.), 2010. Fiberglass and glass technology: energy-friendly compositions and applications. Springer, New York.

Walpole, L., 1981. Elastic Behavior of Composite Materials: Theoretical Foundations. In: Advances in Applied Mechanics. Vol. 21. Elsevier, pp. 169–242.

Willis, J., Jun. 1977. Bounds and self-consistent estimates for the overall properties of anisotropic composites. Journal of the Mechanics and Physics of Solids 25 (3), 185–202.

Willis, J., 1981. Variational and Related Methods for the Overall Properties of Composites. In: Advances in Applied Mechanics. Vol. 21. Elsevier, pp. 1–78.

Wilmes, A., Hornberger, K., 2015. Influence of Fiber Orientation and Multiaxiality on the Fatigue Strength of Unnotched Specimens – Lifetime Estimation. Procedia Engineering 133, 148–160.

Wirjadi, O., 2009. Applications of anisotropic image filters for computing 2D and 3D-fiber orientations. In: Proceedings of the 10th European Congress of ISS. Milan.

Wulfinghoff, S., Cavaliere, F., Reese, S., Mar. 2018. Model order reduction of nonlinear homogenization problems using a Hashin–Shtrikman type finite element method. Computer Methods in Applied Mechanics and Engineering 330, 149–179.

Yang, H., Lindquist, W. B., 2000. Three-dimensional image analysis of fibrous materials. In: Tescher, A. G. (Ed.), Proc. SPIE 4115, Applications of Digital Image Processing XXIII. San Diego, CA, United States.

Zheng, Q.-S., Du, D.-X., 2001. An explicit and universally applicable estimate for the effective properties of multiphase composites which accounts for inclusion distribution. Journal of the Mechanics and Physics of Solids 49 (11), 2765–2788.

List of publications

Hessman, P.A., Hornberger, K., 2017. A comparison of mean field homogenization schemes for short fiber reinforced thermoplastics. PAMM 17, 595–596.

Hessman, P.A., Welschinger, F., Hornberger, K., 2018. Mean field homogenization schemes for short fiber reinforced thermoplastics based on real microstructural information. PAMM 18, e201800388.

Hessman, P.A., Riedel, T., Welschinger, F., Hornberger, K., Böhlke, T., 2019. Microstructural analysis of short glass fiber reinforced thermoplastics based on x-ray micro-computed tomography. Composites Science and Technology 183, 107752.

Hessman, P.A., Welschinger, F., Hornberger, K., Böhlke, T., 2021. On mean field homogenization schemes for short fiber reinforced composites: Unified formulation, application and benchmark. International Journal of Solids and Structures 230–231, 111141.

Hessman, P.A., Welschinger, F., Hornberger, K., Böhlke, T., 2023. A micromechanical cyclic damage model for high cycle fatigue failure of short fiber reinforced composites. Composites Part B: Engineering 264, 110855.

Schriftenreihe Kontinuumsmechanik im Maschinenbau
Karlsruher Institut für Technologie (KIT)
(ISSN 2192-693X)

Band 1 Felix Fritzen
Microstructural modeling and computational homogenization of the physically linear and nonlinear constitutive behavior of micro-heterogeneous materials.
ISBN 978-3-86644-699-1

Band 2 Rumena Tsotsova
Texturbasierte Modellierung anisotroper Fließpotentiale.
ISBN 978-3-86644-764-6

Band 3 Johannes Wippler
Micromechanical finite element simulations of crack propagation in silicon nitride.
ISBN 978-3-86644-818-6

Band 4 Katja Jöchen
Homogenization of the linear and non-linear mechanical behavior of polycrystals.
ISBN 978-3-86644-971-8

Band 5 Stephan Wulfinghoff
Numerically Efficient Gradient Crystal Plasticity with a Grain Boundary Yield Criterion and Dislocation-based Work-Hardening.
ISBN 978-3-7315-0245-6

Band 6 Viktor Müller
Micromechanical modeling of short-fiber reinforced composites.
ISBN 978-3-7315-0454-2

Die Bände sind unter www.ksp.kit.edu als PDF frei verfügbar oder als Druckausgabe bestellbar.

Band 7 Florian Rieger
Work-hardening of dual-phase steel.
ISBN 978-3-7315-0513-6

Band 8 Vedran Glavas
Micromechanical Modeling and Simulation of Forming Processes.
ISBN 978-3-7315-0602-7

Band 9 Eric Bayerschen
Single-crystal gradient plasticity with an accumulated plastic slip: Theory and applications.
ISBN 978-3-7315-0606-5

Band 10 Bartholomäus Brylka
Charakterisierung und Modellierung der Steifigkeit von langfaserverstärktem Polypropylen.
ISBN 978-3-7315-0680-5

Band 11 Rudolf Neumann
Two-Scale Thermomechanical Simulation of Hot Stamping.
ISBN 978-3-7315-0714-7

Band 12 Mauricio Lobos Fernández
Homogenization and materials design of mechanical properties of textured materials based on zeroth-, first- and second-order bounds of linear behavior.
ISBN 978-3-7315-0770-3

Band 13 Malte Schemmann
Biaxial Characterization and Mean-field Based Damage Modeling of Sheet Molding Compound Composites.
ISBN 978-3-7315-0818-2

Band 14 Jürgen Albiez
Finite element simulation of dislocation based plasticity and diffusion in multiphase materials at high temperature.
ISBN 978-3-7315-0918-9

Band 15 Maria Loredana Kehrer
Thermomechanical Mean-Field Modeling and Experimental Characterization of Long Fiber-Reinforced Sheet Molding Compound Composites.
ISBN 978-3-7315-0924-0

Band 16 Peter Hölz
A dynamic and statistical analysis of the temperature- and fatigue behavior of a race power unit – The effect of different thermodynamic states.
ISBN 978-3-7315-0988-2

Band 17 Andreas Prahs
A Gradient Crystal Plasticity Theory Based on an Extended Energy Balance.
ISBN 978-3-7315-1025-3

Band 18 Johannes Ruck
Modeling martensitic phase transformation in dual phase steels based on a sharp interface theory.
ISBN 978-3-7315-1072-7

Band 19 Hannes Erdle
Modeling of Dislocation - Grain Boundary Interactions in Gradient Crystal Plasticity Theories.
ISBN 978-3-7315-1196-0

Band 20 Johannes Görthofer
Microstructure generation and micromechanical modeling of sheet molding compound composites.
ISBN 978-3-7315-1205-9

Band 21 Daniel Wicht
Efficient fast Fourier transform-based solvers for computing the thermomechanical behavior of applied materials.
ISBN 978-3-7315-1220-2

Band 22 Juliane Lang
Thermomechanical Modeling and Experimental Characterization of Sheet Molding Compound Composites.
ISBN 978-3-7315-1232-5

Die Bände sind unter www.ksp.kit.edu als PDF frei verfügbar oder als Druckausgabe bestellbar.

Band 23 Julian Karl Bauer
Fiber Orientation Tensors and Mean Field Homogenization: Application to Sheet Molding Compound.
ISBN 978-3-7315-1262-2

Band 24 Sebastian Gajek
Deep material networks for efficient scale-bridging in thermomechanical simulations of solids.
ISBN 978-3-7315-1278-3

Band 25 Jannick Kuhn
Microstructure modeling and crystal plasticity parameter identification for predicting the cyclic mechanical behavior of polycrystalline metals.
ISBN 978-3-7315-1272-1

Band 26 Felix Ernesti
A computational multi-scale approach for brittle materials.
ISBN 978-3-7315-1285-1

Band 27 Patrick Arthur Hessman
On multi-scale modeling of fatigue in short glass fiber reinforced thermoplastics.
ISBN 978-3-7315-1398-8

Short glass fiber reinforced thermoplastic composites (SFRTs) are crucial for many industrial applications due to their high specific stiffness, strength, corrosion resistance, and low-cost mass production via injection molding. The complex microstructure resulting from the production process necessitates multi-scale simulation models to assess their behavior. This work focuses on micromechanical modeling of SFRTs, specifically PA66-GF composites with varying fiber mass fractions, to describe their elastic and fatigue behavior. A novel single fiber segmentation algorithm is introduced to obtain microstructural data from x-ray micro-computed tomography scans. Analytical mean-field homogenization schemes are studied and compared for predicting effective elastic properties. A micromechanical high cycle fatigue model using the Two-Step homogenization scheme is proposed, incorporating damage variables for fibers and matrix material. The model's ability to predict fatigue limits is evaluated using S-N curves for different fiber orientations and mass fractions.

ISSN 2192-693X
ISBN 978-3-7315-1398-8

Gedruckt auf FSC-zertifiziertem Papier